RELATION OF THE EXTREME ULTRAVIOLET REFLECTANCE TO THE OPTICAL CONSTANTS GENERATED BY A KRAMERS-KRONIG ANALYSIS WITH APPLICATION TO SAMPLES OF THE ALLOY $Cd_xZn_{3-x}As_2$

A THESIS

Presented to

The Faculty of the Division of Graduate

Studies and Research

By

Harry W. Ellis

In Partial Fulfillment

of the Requirements for the Degree

Doctor of Philosophy

in the School of Physics

Georgia Institute of Technology

March, 1974

RELATION OF THE EXTREME ULTRAVIOLET REFLECTANCE

TO THE OPTICAL CONSTANTS GENERATED BY A KRAMERS-KRONIG ANALYSIS

WITH APPLICATION TO SAMPLES OF THE ALLOY $Cd_xZn_{3-x}As_2$

Approved:

James R. Stevenson, Chairman

Augustus L. Stanford

Stephen Spoon

Date approved by Chairman: 3-1-74

ACKNOWLEDGMENTS

I would like to express my deepest thanks to Dr. James R. Stevenson for his guidance and counsel during the course of this research. I wish also to thank Dr. Augustus L. Stanford and Dr. Stephen Spooner for their help and suggestions in the writing of this manuscript. I would like to acknowledge the advice and assistance given me by Dr. D. C. O'Shea during the writing, and the help of Dr. D. E. Wrege in preparing the programs for the PDP-12.

I also wish to acknowledge the cooperation of E. M. Rowe, R. A. Otte, and Dr. C. H. Pruett of the University of Wisconsin Physical Sciences Laboratory, and of Dr. L. N. Tharp and J. R. House of the Georgia Tech Engineering Experiment Station. Thanks are due Dr. E. D. Palik and personnel at the Naval Research Laboratory for supplying our samples and information on polishing and etching techniques. In addition I wish to thank Mr. K. B. Springfield for his assistance in the construction phase of this research and Maury Zivitz, fellow traveler, from whom much valuable advice was received.

Support for this investigation was provided by a grant from the U. S. Air Force (Grant No. AFOSR-70-1892) and by funds made available from the THEMIS Contract F44620-68-C-0008. This support is gratefully acknowledged.

Finally, a special expression of thanks is devoted to my parents, who never lost faith.

TABLE OF CONTENTS

TABLE OF CONTENTS (Concluded)

LIST OF TABLES

LIST OF ILLUSTRATIONS

LIST OF ILLUSTRATIONS (Continued)

LIST OF ILLUSTRATIONS (Continued)

LIST OF ILLUSTRATIONS (Concluded)

SUMMARY

The complex dielectric constant determines the response of a material medium to an applied electric field. For a time-varying electric field the dielectric constant depends upon the frequency. The index of refraction of light is closely related to the dielectric constant; thus a knowledge of one is sufficient to determine the other. The complex index of refraction of a material may be calculated by means of the Kramers-Kronig dispersion relations if values of reflectance are known over a large range of photon energies.

We have measured the reflectance of members of the $Cd_xZn_{3-x}As_2$ alloy system. Existing results on the same samples in the visible and infrared spectral regions were used, and an experiment was designed to extend the measurements to higher photon energies than previously obtained for these samples. We have made use of the electron storage ring at the University of Wisconsin Physical Sciences Laboratory as an intense source of light in the extreme ultraviolet spectral region. An ultra-high vacuum experimental chamber was designed to be compatible with this light source and to provide a suitable environment for the sample. Near-normal incidence reflectance measurements were made in the energy range 8.8 - 30.9 eV, and transitions from the cadmium and zinc d-bands were observed. We have developed the capability for combining characterization of the surface by Auger spectroscopy and optical measurements in the extreme ultraviolet.

We have investigated the manner in which the reflectance at high

energies (beyond 11.0 eV) affects the calculated dielectric constant at lower energies. We have developed a method for optimizing the necessary extrapolation of reflectance data into the high energy region beyond the data. An analytical description of a theoretical model was used to establish a relation between the known behavior of the optical constants in obeying certain sum rules and the agreement of the calculated dielectric constant to the true value.

CHAPTER I

INTRODUCTION AND THEORETICAL CONSIDERATIONS

The Interest

Semiconductor alloy systems are of interest because they offer the possibility of a choice of electrical properties by varying the alloy concentration. Cadmium arsenide (Cd_3As_2) and zinc arsenide (Zn_3As_2) are particularly interesting because electrical measurements (1,2) indicate a wide variance of semiconductor properties while the crystallographic structures (body-centered tetragonal) are sufficiently similar that solid solutions may be formed. Cd_3As_2 is a degenerate n-type semiconductor (1) with a high carrier mobility and a small band gap (about 0.13 eV) while Zn_3As_2 is p-type with a low mobility and a relatively large band gap (about 1.0 eV). Lin-Chung (3) has performed theoretical band structure calculations for the two materials and for the alloy $Cd_xZn_{3-x}As_2$ based on magnetoabsorption experiments and infrared optical measurements. This band structure extended only through the valence and conduction bands. Thus, while low energy optical data may be interpreted on the basis of this structure, extension to deeper lying bands depends upon a determination of the optical properties at higher energies.

The dielectric constant (which is a function of the frequency) determines many of the electrical and optical properties of a material. At optical frequencies this function may be obtained from measurements of optical reflectance, transmission or both. The mechanical and chemical

nature of our samples precluded the preparation of samples thin enough to transmit measurable radiation in the extreme ultraviolet. Therefore, the reflectance was chosen as the observed quantity. Although the dielectric constant may be determined by measurement of reflectance at more than one angle of incidence for a single frequency, we have chosen for experimental reasons to measure the reflectance over a large range of photon energies and use the Kramers-Kronig dispersion relations to obtain the optical and dielectric constants.

The samples used in this research were grown at the Naval Research Laboratories using a modified Bridgman technique which has been described (4). A string saw was used to cut the ingots into discs approximately 2 mm thick. The purity achieved was such that the free carrier density in the Cd_3As_2 samples was typically 2×10^{18} cm^{-3} with a lower density for the alloy and for Zn_3As_2 (4). The samples were received by the author as discs. Cracks in the crystals became apparent upon polishing. The samples were quite brittle and tended to disintegrate easily. The polycrystalline nature is apparent in the infrared and visible reflectance data reported by Zivitz (5).

Our research on samples of this alloy consisted primarily of two parts. An experiment was designed which allowed measurements of the reflectance spectrum to incident photon energies up to 30 eV. Secondly a careful study has been made of the means by which a Kramers-Kronig calculation of the dielectric constant is made from reflectance data. In particular we have become interested in the effect of the reflectance at high photon energies (> 12.0 eV) on the calculated dielectric constant. A new method is proposed by which the reflectance may be best extrapolated beyond

the highest energy at which data are available.

In addition to our primary interests our research has provided motivation to investigate and develop techniques which we believe will be of assistance in advancing work on the optical properties of solids. Our familiarity with the storage ring as a radiation source led us to explore the possibility of using the infrared radiation from a synchrotron as a spectroscopic source. Both analytical and experimental measurements were made, and the work is described elsewhere (6). Our concern over a knowledge of the surface quality during optical measurements led to the development of an experimental chamber which has the flexibility of allowing ion bombardment of the surface and which combines an Auger electron spectrometer with an optical system capable of reflection or transmission measurements. This chamber is described in Chapter II, although only crude Auger spectra were obtained during this research. Later refinements have yielded high quality Auger data.

In the remainder of this chapter we present the elementary theory which relates the measured reflectance to the electrical and optical properties of interest. In Chapter II we describe the design of apparatus which was used in acquiring reflectance measurements in the extreme ultraviolet ($\hbar\omega > 12.0$ eV) spectral range. Finally, in Chapter III we report the results of our study of the calculation of the dielectric constant by a Kramers-Kronig analysis of reflectance data.

History

Interest in the problem of the interaction of light with matter is as old as physics. Sir Isaac Newton in 1666 made studies in which sunlight

was dispersed into various colors upon being passed through a glass prism. Further experiments with materials other than glass provided evidence that the colors were inherent in the original sunlight and that the presence of a material body merely acted to separate them by bending the direction of travel of various colors by different amounts. As the wave theory of light gained wide acceptance in the 19th century, measurements of the phase of monochromatic light showed that light passing through a material behaved as if it traveled with a different phase velocity in the material than that in vacuum. The refractive index characteristic of a medium was introduced, and defined such that the apparent phase velocity in the medium was c/n where c is the phase velocity in vacuum. Together with the Fresnel - Kirchhoff formalism, the refractive indices of the media were sufficient to correctly explain the amount of bending in the direction of travel of the light upon encountering a boundary between the two media. The dispersion observed by Newton is explained if the refractive index varies with the wavelength of visible light, the index decreasing for the larger values of wavelength.

A theoretical prediction of the wavelength dependence of the refractive index based on a model of the material medium was given by Cauchy in 1836. The model considered was that of an elastic solid composed of particles and one in which the wavelength λ was much longer than the distance between particles. The index of refraction was given by (7)

$$n = a + b/\lambda^2 + d/\lambda^4 \ . \ . \ . = \sum_m a_m \lambda^{-2m} \qquad (1\text{-}1)$$

in which the a_m were adjustable parameters independent of λ. After Fraunhofer's discovery of absorption spectra in the early 19th century, it was found by LeRoux in 1862 that the dispersion near an absorption line differed greatly from that predicted by Equation 1-1. The terms "normal" and "anomalous" dispersion were used for the behavior exhibited, respectively, far away from and near the absorption lines. Near absorption lines the index was found to vary as

$$n^2 = 1 + \frac{A\lambda^2}{\lambda^2 - \lambda_0^2}$$

where λ_0 is the absorption line wavelength.

The Dielectric Constant

Maxwell's work in electromagnetism laid the basis for further understanding. The association of light and time-varying electric and magnetic fields, together with the molecular theory of matter, resulted in a model which accurately predicted the wavelength dependence of the dispersion of light.

The strength of the electric field at a point must ultimately be defined in terms of the force F experienced by a test charge q at that point: $\vec{E} = \vec{F}/q$. Direct measurement of the field inside a dielectric is difficult. In the absence of a model when indirect techniques such as measuring the capacitance of the dielectric material are employed, the measured field represents an average over the interior volume and is insensitive to local variations within the medium. It is this average or

"macroscopic" electric field which appears in Maxwell's equations and which will1 be discussed here. According to Gauss' law, the sources of electric field are charges, from which the electric field may be found from

$$\nabla \cdot \vec{E} = 4\pi\rho \tag{1-2}$$

where ρ is the volume charge density. If a charge $V\rho$ is placed uniformly upon a dielectric of volume V, originally neutral, the electric field is determined. It was early discovered, however, that the field strength inside the dielectric was different from that predicted by Equation 1-2 on the basis of a charge density ρ. The dielectric had the effect of changing the field strength inside it by a factor ϵ, such that the true field in the dielectric was

$$\vec{E} = \vec{D}/\epsilon \tag{1-3}$$

where $\vec{D}$ is the field which would result from the charge density ρ in the absence of a dielectric and was called by Maxwell the electric induction. In the absence of an excess or "free" charge density, Gauss' law becomes $\nabla \cdot \vec{D} = 0$. The factor ϵ takes into account the presence of the material medium, i.e., the dielectric, and is named the dielectric constant. A similar relation exists between the magnetic field strength $\vec{H}$ and the magnetic induction $\vec{B}$ in a material: $\vec{B} = \mu\vec{H}$. Many materials are, however, non-magnetic, and in such a case μ is unity in the Gaussian system of units. Maxwell's equations for the electric and magnetic fields in a non-magnetic homogenous medium containing no free charge are then

$$\nabla\cdot\vec{D} = 0 \qquad \nabla\cdot\vec{B} = 0 \qquad \nabla \times \vec{E} = -\frac{1}{c}\frac{\partial\vec{H}}{\partial t} \qquad \nabla \times H = \frac{1}{c}\frac{\partial\vec{D}}{\partial t}$$

from which may easily be obtained the equations

$$\nabla^2\vec{E} - \frac{\epsilon}{c}\frac{\partial^2\vec{E}}{\partial t^2} = 0 \qquad \nabla^2 H - \frac{\epsilon}{c^2}\frac{\partial^2 H}{\partial t^2} = 0$$

Solutions to these equations are transverse waves which may be represented by $E = E_0\, e^{i(\omega t - \vec{k}\cdot\vec{r})}$ where the frequency is $\nu = \omega/2\pi$ and the wavelength is $\lambda = 2\pi/|\vec{k}|$. Substitution of this solution into the wave equation shows immediately that points of equal phase travel with a velocity $c/\sqrt{\epsilon}$. If we identify electromagnetic waves with light, the index of refraction must be $n = \sqrt{\epsilon}$, thus establishing a relation between the optical and electrical properties of the material.

Even in the absence of a particular model, it must be supposed that some physical behavior of the dielectric is responsible for its dielectric properties and that the behavior is a response to the presence of the field. Since it is not to be seriously thought that such a response can be instantaneous, there will generally be a time lag between any change in the field strength and the response of the dielectric. This is equivalent to a phase difference between $\vec{E}$ and $\vec{D}$. In exponential notation $\vec{E} = \vec{E}_0\, e^{i(\omega t - \vec{k}\cdot\vec{r})}$ $\vec{D} = \vec{D}_0\, e^{i(\omega t - \vec{k}\cdot\vec{r}+\delta)}$ then $\epsilon = \dfrac{|\vec{D}|}{|\vec{E}|} = \dfrac{E_0}{D_0}\, e^{+i\delta}$ is complex. We represent complex quantities by a tilde:

$$\tilde{\epsilon} = \epsilon_1 - i\epsilon_2$$

The wave equation will be modified only to the extent of allowing $\tilde{\epsilon}$ to be complex. The solution for the field will remain traveling waves, but these waves will be attenuated with distance:

$$\vec{E}_y = \vec{E}_{y_0} e^{i\omega(t-\tilde{n}x/c)}$$

where a complex index of refraction is defined by

$$\tilde{n} = n_i - ik$$

Substitution into the wave equation yields

$$\tilde{n}^2 = \tilde{\epsilon}$$

Then we have, as before, the relation

$$n = c/v$$

where v is the phase velocity and k is an attenuation coefficient, such that the amplitude is attenuated by a factor 1/e for each distance

$$x = c/\omega k$$

traveled in the medium.

The dielectric constant may be related to other more fundamental electrical properties of the material through the atomic model. If it is assumed that the substance in question is composed of equal numbers of positively and negatively charged particles occupying positions of equilibrium, the effect of an electric field applied from an external source

is to exert force on the charges in opposite direction for the two kinds of charge. The result is the formation of dipoles with dipole moment

$$\vec{p} = q\vec{x}$$

where $\vec{x}$ is the charge separation. It may be that the material is composed of polar molecules already possessing dipole moments which are randomly oriented in the absence of a field (we are specifically excluding electrets). In this case the interaction between the dipole and the applied field produces in effect a torque on the dipoles, resulting in greater ordering and a net dipole moment per unit volume. In either case the polarization $\vec{P}$ is defined as the net dipole moment per unit volume and is simply the vector sum over all molecular dipoles. Since the interaction energy between an electric field and a dipole is the scalar product $-\vec{p}\cdot\vec{E}$, the energy stored in a volume V through the interaction is given by

$$U = -\int_V \vec{P}\cdot\vec{E}\ dV$$

Expressing the electric field as $-\nabla\varphi$ where φ is the electrical potential, and using a vector identity, we obtain the energy density in terms of volume and surface integrals

$$U = -\int_V \varphi\nabla\cdot\vec{P}\ dV + \int_S \nabla\cdot(\vec{P}\varphi)\ dS$$

Electrical energy may be expressed in just this way in terms of potentials and charge densities. We identify the volume and surface charge densities

ρ and σ, respectively, as (8)

$$\rho = - \nabla \cdot \vec{P} \qquad \sigma = \vec{P} \cdot \hat{n}$$

where $\hat{n}$ is a unit vector normal to the surface S. This volume charge density produces a source of electric field determined by the relation

$$\nabla \cdot \vec{E} = 4\pi\rho = - 4\pi \nabla \cdot \vec{P}$$

so that we have

$$\nabla \cdot (\vec{E} + 4\pi\vec{P}) = 0$$

If there were a free (excess) charge density ρ_f in addition to the ρ above the equation would become

$$\nabla \cdot (\vec{E} + 4\pi\vec{P}) = 4\pi\rho_f \equiv \nabla \cdot \vec{D}$$

so, obviously, we may identify the electric induction of Maxwell (known also as the displacement field) as

$$\vec{D} = \vec{E} + 4\pi\vec{P}$$

and we infer that the polarization $\vec{P}$ determines the extent to which the presence of the dielectric causes the electric field to differ from that caused by the free charge alone, i.e., $\vec{D}$. Since we have from Equation 1-3

$$\vec{D} = \tilde{\epsilon}\ \vec{E}$$

the relation between the polarization and the field must be

$$\vec{P} = \frac{\tilde{\epsilon}-1}{4\pi} \vec{E}$$

In a low field approximation and for a homogeneous linear material the polarization is just proportional to the applied field and parallel to it. The constant of proportionality is the electric susceptibility, $\tilde{\chi}$, and is

$$\tilde{\chi} = \frac{\tilde{\epsilon}-1}{4\pi} \tag{1-4}$$

The relation between P and E is linear to a good approximation for all but extremely intense fields such as those produced in laser beams (8). For a non-homogeneous material, however, the direction of the induced polarization will not in general be the same as that of E. In this case the above expressions are valid if $\tilde{\epsilon}$ and $\tilde{\chi}$ are tensor quantities.

The molecular property, then, which determines the electrical and optical behavior of a material is the degree to which the molecules can be polarized. This property is obviously closely related to the susceptibility, but account must be made for the effect of nearby dipoles on the electric field at a molecular site. The average field E which enters Maxwell's equations must be corrected to obtain E_{loc}, the "local" field at the molecule. Following H. A. Lorentz (9), this correction is made by drawing an imaginary surface about the site in question and accounting for all dipoles exterior to this surface through the effect of the surface charge density, which will be $B\vec{P}$ where B is characteristic of the geometry.

For a spherical surface its value is $B = \frac{4\pi}{3}$. The dipoles inside the imaginary surface contribute an electric field $S\vec{P}$, where S = 0 for cubical symmetry and is in general a tensor quantity. The local field is then

$$\vec{E}_{loc} = \vec{E} + (B + S)\ \vec{P} \tag{1-5}$$

and the polarizability of the molecules (which is not a directly observable quantity) is defined by

$$\vec{P} = \tilde{\alpha}\ \vec{E}_{loc} \tag{1-6}$$

and is related to the dielectric constant $\tilde{\epsilon}$ by

$$\tilde{\alpha} = \frac{\tilde{\epsilon}-1}{(4\pi-B-S) + \tilde{\epsilon}(B+S)}$$

An expression for the polarizability may be derived from a classical model of the electrons in a material and the various forces acting on them.

If, in a dielectric, the electrons are bound near an equilibrium position, the potential energy may be expanded in a power series in the distance from the equilibrium position. Since the first non-constant term has a coefficient of zero, the first significant term is a Hooke's law potential. Assuming a sufficiently small displacement from equilibrium the restoring force may be represented solely by an expression linear in the displacement. The application of an electric field with a sinusoidal time dependence will result in the harmonic oscillation of the electron

about the position of equilibrium. These oscillations will be damped classically by the emission of radiation as well as by any collisions suffered by the electron. The radiation damping produces an effective force proportional to (10) $d^2\vec{v}/dt^2$, while the number of collisions per second is directly proportional to the velocity. For harmonic oscillatory motion, the radiation damping force has the same phase as the velocity, so that both may be included in a single velocity-dependent force term in the equation of motion of the electron. The coefficient of this term will, however, be a function of the frequency. The equation of motion in the direction of a polarized alternating electric field may be written as

$$m \frac{d^2\vec{x}}{dt^2} + \eta \frac{d\vec{x}}{dt} + \xi\vec{x} = - eE_0 e^{i\omega t}$$

solutions to which are

$$\tilde{\vec{x}} \qquad \tilde{\vec{x}}_0 e^{i\omega t}$$

where

$$\tilde{x}_0 = \frac{- eE_0/m}{(\omega_0^2 - \omega^2 + i\Gamma\omega)} \; ; \; \omega_0^2 = \frac{\xi}{m} \; , \; \gamma = \frac{\eta}{m}$$

where ω_0 is a characteristic frequency of the atoms. The dipole moment produced is

$$\vec{p} = - e\tilde{\vec{x}}_0 e^{i\omega t}$$

so the macroscopic polarizability per unit volume is

$$\tilde{\alpha} = \frac{Ne^2}{m} \frac{1}{(\omega_0^2 - \omega^2 + i\gamma\omega)} \tag{1-7}$$

where N is the volume particle density.

The relation between the dielectric constant and the polarizability may be obtained from Equations 1-4, 1-5, and 1-6 as

$$\tilde{\epsilon} = 1 + \frac{4\pi\tilde{\alpha}}{1 - (B+S)\,\tilde{\alpha}}$$

Taking $\tilde{\alpha}$ from Equation 1-7, we find upon separating the real and imaginary components

$$\epsilon_1 = 1 + \frac{4\pi Ne^2}{m} \frac{\omega_0^2 - \omega^2 - \frac{Ne^2}{m}(B+S)}{\left\{\omega_0^2 - \omega^2 - \frac{Ne^2}{m}(B+S)\right\}^2 + \gamma^2\omega^2} \tag{1-8}$$

and

$$\epsilon_2 = \frac{4\pi Ne^2}{m} \frac{\gamma\omega}{\left\{\omega_0^2 - \omega^2 - \frac{Ne^2}{m}(B+S)\right\}^2 + \gamma^2\omega^2}$$

If we ignore the local field correction, we have

$$\epsilon_1 = 1 + \frac{4\pi ne^2}{m} \frac{(\omega_0^2 - \omega^2)}{(\omega_0^2 - \omega^2)^2 + \gamma^2\omega^2} \tag{1-9}$$

$$\epsilon_2 = \frac{4\pi ne^2}{m} \frac{\gamma\omega}{(\omega_0^2 - \omega^2)^2 + \gamma^2\omega^2}$$

The effect of the local field correction is to shift the resonant

frequency from ω_0 to ω_0', where

$$\omega_0' = \omega_0^2 - \frac{Ne^2}{m} \quad \text{(B+S)}$$

The optical constants are related to the dielectric constant by

$$\tilde{n}^2 = \tilde{\epsilon}$$

so we have the relations

$$n^2 = \frac{1}{2}\left[\epsilon_1 + \sqrt{\epsilon_1^2 + \epsilon_2^2}\right] \qquad (1\text{-}10)$$

$$k^2 = \frac{1}{2}\left[-\epsilon_1 + \sqrt{\epsilon_1^2 + \epsilon_2^2}\right]$$

for the real and imaginary parts of the refractive index.

From Equations 1-9 it is apparent that far from resonance, we have

$$|\omega_0^{2\prime} - \omega^2| \gg \gamma\omega$$

and ϵ_2 will be small. The attenuation coefficient k will then be small and the result will be the relation

$$n^2 = \epsilon_1 \qquad (1\text{-}11)$$

as in "normal" dispersion. Near resonance, ϵ_2 becomes appreciable and k becomes significantly different from zero.

The energy which disappears from this wave must be absorbed in the medium. To approach this, we consider the current created by the oscilla-

tion of the charges about their position of equilibrium. From Maxwell's equations the current must be (8)

$$\nabla \times \vec{H} = \frac{4\pi}{c} \vec{J} = \frac{1}{c} \frac{\partial \vec{D}}{\partial t} = \frac{1}{c} \frac{\partial}{\partial t} (\tilde{\epsilon}\vec{E})$$

so that, for the time dependence previously assumed for $\vec{E}$, and defining the conductivity $\tilde{\sigma}$ via the equation

$$\vec{J} = \tilde{\sigma} \vec{E}$$

we have

$$\sigma_1 = \frac{\omega \epsilon_2}{4\pi}$$

$$\sigma_2 = \frac{\omega \epsilon_1}{4\pi}$$

The Joule heating power loss is

$$\vec{J} \cdot \vec{E} = \mathrm{Re}[\tilde{\sigma} \overline{E^2}]$$

or, for a sinusoidal field,

$$\vec{J} \cdot \vec{E} = \frac{\omega \epsilon_2 E_0^2}{8\pi}$$

A similarity in the behavior of k and ϵ_2 is therefore predicted, since an attenuation of the field implies a loss of energy which appears as Joule heating in the medium. The imaginary component of the conductivity corresponds to a current out of phase with the electric field, and results in no loss of energy to the field. Nevertheless the dipoles are coupled

to the field just as two masses connected by a spring undergoing harmonic oscillation. A large out-of-phase component of current (large value of ϵ_1) implies a large portion of the wave's energy being continually absorbed and re-radiated, whereupon the newly radiated waves interfere with the existing waves. Even if no net energy is lost ($\epsilon_2 = 0$) from the incident wave, the phase of the resultant electromagnetic wave will be affected by the time delay associated with the dipole interaction, and an index of refraction characteristic of the dipoles will result.

In a real solid there will exist many frequencies at which a particular type of molecule may absorb energy, as well as perhaps several different types of molecules. In this case the formulae for the polarizability and for the dielectric constant require a sum over the various resonant frequencies ω_{0_i}, possibly with different damping coefficients and particle volume densities; e.g.,

$$\epsilon_1 = 1 + \sum_i \frac{4\pi N_i e^2}{m_i} \frac{\omega_{0_i}^2 - \omega^2}{\left\{\omega_{0_i}^2 - \omega^2\right\}^2 + \gamma^2\omega^2}$$

with a similar form for ϵ_2.

Quantum Mechanical Considerations

A quantum mechanical treatment yields, under several simplifying assumptions, a result for the dielectric constant that is remarkably similar to the classical form. The formulation of a Hamiltonian for the interaction between the medium and the electromagnetic field is based upon the Lorentz force law for a particle with a charge q in the presence of electric and magnetic fields $\vec{E}$ and $\vec{B}$, respectively, which is

$$\vec{F} = q[\vec{E} + \frac{1}{c}\vec{v} \times \vec{B}]$$

where $\vec{v}$ is the particle velocity. The field quantities may be expressed in terms of a vector potential $\vec{A}$ and a scalar potential φ by the relations

$$\vec{B} = \nabla \times \vec{A} \qquad \vec{E} = -\nabla\varphi - \frac{1}{c}\frac{\partial\vec{A}}{\partial t}$$

A generalized potential may be written for the interaction:

$$u = q\varphi - \frac{q}{c}\vec{A}\cdot\vec{v}$$

where the components of force may be derived from

$$F_i = -\frac{\partial u}{\partial x_i} + \frac{d}{dt}\frac{\partial u}{\partial v_i}$$

The momentum is obtained from the Lagrangian, and given by

$$\vec{p} = m\vec{v} + \frac{q}{c}\vec{A}$$

and the Hamiltonian as a function of coordinates and conjugate momentum is

$$H = \frac{1}{2m}\left(\vec{p} - \frac{q}{c}\vec{A}\right)^2 + q\varphi$$

where, in the quantum mechanical treatment, the momentum $\vec{p}$ is replaced by the operator $-i\hbar\nabla$. Expanding, we have

$$H = \frac{p^2}{2m} + q\varphi + \frac{q^2}{2mc^2}\vec{A}^2 - \frac{q}{2mc}\left[\vec{p}\cdot\vec{A} + \vec{A}\cdot\vec{p}\right]$$

For the externally applied electromagnetic field, both $\vec{A}(\vec{r},t)$ and $\varphi(\vec{r},t)$ obey a wave equation, if $\vec{E}$ and $\vec{B}$ do. A gauge can be chosen (11), however, so that the scalar potential originating from the applied field is zero. The Hamiltonian can be grouped conveniently into terms representing the charged particles in the absence of an applied field and terms representing the interaction with the applied field:

$$H = H_0 + H_i$$

where

$$H_i = \frac{q^2}{2mc^2}\vec{A}^2 - \frac{q}{2mc}\left(\vec{p}\cdot\vec{A} + \vec{A}\cdot\vec{p}\right]$$

is the interaction term.

The state functions of the system in the absence of radiation are eigenfunctions of H_0, and the energy states available are the eigenvalues obtained from the Schroedinger equation. We discuss the interaction with radiation in terms of electronic transitions between allowed states, and further, we employ the "one-electron" approximation in which transitions of an electron are not affected by transitions involving other electrons. The environment of an electron, including the presence of other electrons, phonons, etc. is represented by H_0 which is a constant not affected by the presence of radiation. Any interaction of an electron with the field is assumed to be direct, as represented by H_i, not through interaction with other particles which may be perturbed by the radiation. This is equiva-

lent to assuming that relatively few electrons interact with the field. The state function for this system of electrons is then a product of single-electron wave functions:

$$\Phi = \prod_i \psi_i$$

If the radiative effects are sufficiently small the problem may be treated by time-dependent perturbation theory in which the electrons are assumed to occupy near eigenstates of H_0, while the field acts to induce transitions between states. As allowed by the expansion postulate, the electron wave function is expressed as a summed series of eigenfunctions of H_0 (12)

$$\psi(t) = \sum_j C_j(t)\psi_j^{(0)}$$

where

$$H_0\psi_j^{(0)} = E_j\psi_j^{(0)}$$

and

$$\sum_j |C_j|^2 = 1$$

The probability at time t that the electron is in a state ψ_m^0 is $|C_m|^2$. The initial value of C_m is unity for the ground state and zero for all others, i.e., $|C_0|^2 = 1$. The time evolution of the system is described by the behavior of C_j which obeys the equation

$$C_j(t) = \frac{C_0}{i\hbar} \int \psi_j^0 H_i \psi_0^0 \, d\tau$$

where H_i is the perturbation Hamiltonian.

Since the effect of H_i is assumed small compared to H_0, the first order solution is obtained by requiring that $C_0(t) = 1$ for all t.

For the weak interactions assumed, we neglect the contribution to the perturbation Hamiltonian proportional to $\vec{A}^2$. It may be shown (12) that this term represents two-photon interactions with an electron, which are unlikely compared with single-photon interactions unless the field (photon flux) is extremely large. We shall, nevertheless, assume that the field is strong enough so that a "semi-classical" treatment is valid, i.e., one in which the field is well represented by the classical Maxwell equations. We shall assume that the electromagnetic field varies sinusoidally with time and is described by a vector potential given by

$$\vec{A} = \vec{A}_0 \exp \{i(\omega t - \vec{K}\cdot\vec{r})\}$$

which is a transverse wave. This is not true if there are collective electron motions (plasmons) in the medium, but we have previously forbidden such considerations in making the single-electron approximation. For transverse fields we have

$$\nabla\cdot\vec{A} = 0$$

and it can be shown that the interaction Hamiltonian operator reduces to

$$H_i = -\frac{q}{2mc}[\vec{p}\cdot\vec{A} + \vec{A}\cdot\vec{p}] = -\frac{q}{mc}[\vec{A}\cdot\vec{p}]$$

The coefficients C_j are determined by integrals of the type

$$\int \psi_j^0 H_i \psi_0^0 \, d\tau = - \frac{q}{mc} \int \psi_j^0 \vec{A}\cdot\vec{p} \, \psi_0^0 \, d\tau$$

where the spatial dependence of the field is of the form $e^{i\vec{K}\cdot\vec{r}}$. For fields whose wavelength $(2\pi/|\vec{K}|)$ is long compared to the distance over which the interaction occurs, the exponential dependence on distance may be approximated by unity. This is commonly known as the dipole approximation. In this case the integrals which determine the coefficient C_j are reduced to

$$- \frac{q}{mc} \vec{A}_0 \cdot \int \psi_j^0 \vec{p} \, \psi_0^0 \, d\tau$$

If we neglect damping, it is possible to express these matrix elements of momentum as matrix elements of the dipole moment. The unperturbed Hamiltonian contains a kinetic term plus a term V_0 which includes all the various interactions which the electron undergoes, specifically excluding the applied radiation. If this potential commutes with the position operator, a supposition tantamount to the assumption that V_0 contains no momentum-dependent (damping) terms, then one may derive the result

$$[\vec{r}, H_0] = \frac{i\hbar}{m} \vec{p}$$

where $\vec{r}$ represents the displacement from some equilibrium position. Since functions ψ_j^0 are eigenfunctions of H_0, the matrix elements involved in

calculating the C_j are those of the dipole moment given by

$$(\vec{M}_{j0}) = \int \psi_j^{0*}(q\vec{r})\ \psi_0^0\ d\tau$$

Under the assumptions and conditions set forth, a straightforward calculation (11) yields a transition rate of an electron from the ground state to the state j. The expectation value of the dipole moment may be calculated, and the polarizability due to transition between states 0 and j is found to be

$$\alpha_{j0} = \frac{e^2}{m} \frac{f_{j0}}{\omega_{j0}^2 - \omega^2} \qquad (1\text{-}12)$$

where

$$f_{j0} = \frac{2m}{\hbar e^2}\, \omega_{j0}\ |\vec{M}_{j0}|^2$$

is called the oscillator strength, and ω_{j0} is defined by

$$\omega_{j0} = \frac{(E_j - E_0)}{\hbar}$$

A direct comparison with the classical result shows that f_{j0} replaces the number of electrons participating in the interaction, the resonant frequency becomes the Bohr frequency for the energy difference between the initial and final electronic states, and the damping term is absent. We have specifically excluded damping due to collisions and the velocity-dependent interactions which prevent an infinitely narrow resonance. In addition, we have excluded the life-time broadening effect due to the decay

of the system from the initial state.

If, following Seitz (12), we do not take the coefficient of the initial state, C_0, to be constant but rather assume a time dependence $e^{-2\pi\gamma t}$, the result is the appearance of an imaginary term in the denominator of Equation 1-12.

It is well known that the periodicity of the lattice in crystalline solids demands that the electronic wave function possess a translational symmetry characteristic of the lattice. The resulting allowed electronic energies lie in bands which are in general separated by forbidden values. These bands may be related to the atomic energy levels but have a finite width. In the ground state the electrons occupy, insofar as the exclusion principle allows, those bands whose energies are lowest. There will be, then, some highest energy band which is occupied, either partially or completely, viz the valence band. Above this level lie states, possibly in the valence band and certainly in other bands, which are available to an electron of sufficient energy and to which any of the electrons in the lower energy states may be excited if supplied with the necessary energy.

The expression for the polarizability given in Equation 1-12 must be considered valid only for transitions between states which have discrete energies and must be summed over all available initial and final states if a real solid is to be represented. The summation over the spectrum of states in each band causes the polarizability as a function of the light frequency to exhibit broad peaks rather than discrete lines (13). In addition the finite width of the bands makes possible transitions within bands, where a practical continuum of states is available. This contributes

to the polarizability a "free electron" term which has no "resonant" frequency, i.e., $\omega_{j0} = 0$ in Equations 1-9. This intra-band contribution is significant for low light frequencies, but its $1/\omega^2$ dependence makes it of small importance (relative to the interband "resonance") in the visible and ultraviolet spectral regions.

We feel that we have sufficiently established the polarizability, and thus the dielectric constant, as characteristic of several important fundamental properties of a medium and thus justified an effort to measure them carefully. An accurate determination of the optical properties can aid in the creation of a band structure for a material; for example, in the simplest interpretation the location of structure in the dielectric constant is representative of energy difference between bands, and the width and shape of the structure are characteristic of the width and density of states in the bands as well as the amount of damping present. The damping itself may be separated into contribution of lifetime broadening, collision processes, etc. Obviously, sophisticated methods must in general be used to reduce measurements of the dielectric constant to a detailed knowledge of the band structure; nevertheless such measurements are prerequisite. Since our experiment is basically directed at obtaining accurate values of the optical properties through measurement and subsequent analysis of the data, we refrain from becoming more involved in the theoretical treatment of the band structure of our samples (see Reference 5).

Reflectance Determination of the Dielectric Constant

We have shown that the dielectric constant is intimately related to

the complex index of refraction (Equation 1-10), so that a measurement of one suffices to determine the other. In an optical experiment the complex index of refraction may be obtained by reflection measurements or by transmission. Since transmission measurements for a sample are dependent on preparing a thin specimen of known thickness, reflection measurements were used in this work.

Maxwell's equations establish the behavior of electric and magnetic fields at the interface of two media: the components of the electric field parallel to the surface and of the magnetic field normal to the surface cannot charge at the boundary while the normal electric field and parallel magnetic field may change if there are charges or currents, respectively, on the boundary surface. The ratio of the amplitude of the reflected field to the incident field is the complex reflectance and is given by Fresnel's equations (14). For an electromagnetic wave incident from the vacuum on a material, the reflectance is in general a function of the angle of incidence, as well as the complex index of refraction, which is indicative of the induced surface charges and currents. For normal incidence, the reflectance is

$$\tilde{r} = \frac{\tilde{E}_r}{\tilde{E}_i} = \frac{n-1-ik}{n+1-ik} \qquad (1\text{-}13)$$

The complex reflectance has a real and an imaginary part. Physical interpretation is facilitated by writing the complex reflectance in terms of the relative phase shift of the wave upon reflection, which gives

$$\tilde{r} = re^{i\theta}$$

where the measured reflectance is the ratio of intensities

$$R = \frac{|E_r|^2}{|E_i|^2} = |r|^2 = \frac{(n-1)^2 + k^2}{(n+1)^2 + k^2}$$

The equations relating the real and imaginary parts of the index of refraction with the reflectance amplitude and phase shift at normal incidence are obtained from Equation 1-13 and are

$$n = \frac{1 - |r|^2}{1 + |r|^2 - 2|r|\cos\theta} \qquad k = \frac{|r|\sin\theta}{1 + |r|^2 - 2|r|\cos\theta} \tag{1-14}$$

Thus a measurement yielding $\tilde{r}$ determines $\tilde{n}$, which in turn yields the dielectric constant.

Viewed classically, the complex dielectric constant contains information on the dipole oscillations produced in the medium by the applied field. This motion may be considered as the superposition of electronic oscillations in-phase and out-of-phase with respect to the applied field. The out-of-phase displacement (whose current is in-phase with the field) produces a real absorption while the in-phase oscillation produces a "virtual" absorption; i.e., an absorption and re-emission, of some fraction of the energy in the wave. (The real and virtual absorption processes may also be viewed as quantum mechanical in origin.) In the case of virtual absorption the re-emitted wave is not in phase with the incident electromagnetic wave. The resultant (observed) wave is the superposition of the unabsorbed portion of the initial wave and the virtually absorbed wave. The observable result of the virtual absorption is, then, a phase

shift in the resultant wave.

It is noted that one can envision a virtual absorption in the absence of a real absorption (corresponding to $\epsilon_2 = 0$). However, it is not possible for a real absorption to take place in the absence of virtual absorption, since any oscillation of the dipole will result in the emission of radiation. Thus the processes of real and virtual absorption are obviously not independent. Consider, for example, an electromagnetic wave, a portion of which undergoes virtual absorption and is phase-shifted with respect to the original wave. The amplitude of the resultant wave will in general be affected, implying that real absorption has also occurred. Conversely, any attenuation of the incident wave (which we have noted must be accompanied by some virtual absorption) will enhance the relative contribution of the phase-shifted virtually absorbed wave in the resultant, and thus affect its phase.

The equations which relate the absorption and phase shift of a wave are called dispersion relations. Such relations exist between the real and imaginary parts of the complex dielectric constant. In general, dispersion relations exist in any theory in which a function representing a response is linearly dependent upon a function representing the stimulus causing the response and in which the response function is zero prior to the application of the cause. Toll (15) establishes the logical equivalence of this strict causality and the validity of a dispersion relation.

The dielectric constant (in the linear approximation) satisfies these conditions. We identify the response with the polarization, and the cause with the electric field. Then, following Stern (16), we have

$$\tilde{\vec{P}}(t) = \frac{1}{4\pi} (\tilde{\epsilon}-1) \tilde{\vec{E}}(t)$$

Taking two Fourier transforms we obtain

$$\tilde{\vec{E}}(t) = \frac{1}{4\pi^2} \int_{-\infty}^{\infty} dt' \int_{-\infty}^{\infty} \tilde{\vec{E}}(t') e^{i\omega(t'-t)} d\omega$$

so that we can write

$$\tilde{\vec{P}}(t) = \frac{1}{8\pi^2} \int_{-\infty}^{\infty} G(t-t') \tilde{\vec{E}}(t') \, dt'$$

where $G(t-t')$, given by

$$G(t-t') = \frac{1}{2\pi} \int_{-\infty}^{\infty} [\tilde{\epsilon}(\omega) - 1] \, e^{+i\omega(t-t')} d\omega$$

is the Fourier transform of $\tilde{\epsilon}-1$, and gives the response at a time t produced by the electric field at time t'. Then we have the relation

$$\tilde{\epsilon}(\omega) - 1 = \int_{-\infty}^{\infty} G(T) \, e^{i\omega T} \, dT$$

We now invoke the causality requirement that

$$G(T) = 0 \quad ; \quad T < 0$$

Then

$$\tilde{\epsilon}(\omega) - 1$$

is an analytic function for complex values of ω which have a positive imaginary part, since this gives an exponential e^{-BT}, $B > 0$, in the integral, assuring its convergence.

We may then make use of the Cauchy theorem from the theory of complex variables (17) for a bounded region containing no singularities,

$$\oint_C \frac{\tilde{\epsilon}(\omega) - 1}{\omega' - \omega} d\omega' = 0$$

where C encloses the entire half-plane where $\mathrm{Re}(w) > 0$, except the point

$$\omega = \omega'$$

on the real axis. Discarding the contribution for extremely large $|\omega|$ not lying on the real axis because the assumed finiteness of $\tilde{\epsilon}$, and evaluating the small semi-circular path around the point ω' by the residue theorem, we obtain

$$i\pi[\tilde{\epsilon}(\pi) - 1] = P \int_{-\infty}^{\infty} [\tilde{\epsilon}(\omega) - 1] \frac{1}{\omega' - \omega} d\omega'$$

where P indicates the Cauchy principal value of the integral. Separating the real and imaginary parts, we have

$$\epsilon_1(\omega) = \frac{1}{\pi} P \int_{-\infty}^{\infty} \frac{\epsilon_2(\omega)}{\omega' - \omega} d\omega'$$

$$\epsilon_2(\omega) = \frac{1}{\pi} P \int_{-\infty}^{\infty} \frac{\epsilon_1(\omega) - 1}{\omega' - \omega} d\omega'$$

under the assumptions of (1) boundedness of ϵ, (2) linearity of the dependence of the polarization on the electric field, and (3) causality. Use of a simple integral identity transforms the relations to integrals over positive frequencies only, which results in the equations

$$\epsilon_1(\omega) - 1 = \frac{2}{\pi} P \int_0^\infty \frac{\omega' \epsilon_2(\omega')}{\omega'^2 - \omega^2} d\omega'$$

$$\epsilon_2(\omega) = \frac{2\omega}{\pi} P \int_0^\infty \frac{\epsilon_1(\omega)}{\omega^2 - \omega'^2} d\omega'$$

The dispersion relations for the complex reflectance are slightly more difficult to derive because a given reflectance curve does not uniquely determine the phase shift. Toll (15) derives such a relation, and Stern (16) justifies the discarding of pathological terms as being equivalent to restricting the phase shift to values between 0 and 180°. The resulting dispersion relations for the phase shift in terms of the reflectance are (15)

$$\theta(\omega) = \frac{1}{\pi} \int_0^\infty \frac{d \ln |R(\omega')|}{d \ln \omega'} \frac{1}{\omega'} \ln \left| \frac{\omega' + \omega}{\omega' - \omega} \right| d\omega' \qquad (1\text{-}15)$$

where $r = re^{-i\theta}$ and $R = |r|^2$.

Equation 1-15 provides the linkage which allows the determination of the dielectric constant from normal incidence reflection data. Provided that $R(\omega)$ is measured over a sufficiently broad frequency range, $\theta(\omega)$ may be calculated from this equation. Equations 1-14 then yield $\tilde{n}(\omega)$ from which $\tilde{\epsilon}(\omega)$ follows from the relations

$$\epsilon_1 = n^2 - K^2 \qquad \epsilon_2 = 2nK \tag{1-16}$$

which are obtained from Equations 1-10.

Equations 1-14 and 1-16 are exact in the sense that particular values of R and θ yield unambiguous values of $\tilde{n}$ and $\tilde{\epsilon}$. Any error in the results for these functions must enter through incorrect values of R and θ, errors which originate from two distinct sources. Errors of the first type arise from incorrect values in the raw reflectance data which, in general, also give incorrect values for the phase shift. An examination of Equation 1-15 shows, however, that R may be incorrect by an arbitrary multiplicative constant without causing errors in θ. In any case, the results for $\tilde{n}$ and $\tilde{\epsilon}$ will be affected by errors in the experimental reflectance curve.

Errors of the second type arise because reflectance data cannot be obtained over an infinite frequency range. Even if the correct reflectance $R(\omega)$ is measured over a range $\omega_a - \omega_b$, the resulting phase shifts cannot be computed exactly since Equation 1-15 requires the complete reflectance spectrum. The contribution to the phase shift at a frequency ω_o is not equally dependent on the reflectance at all frequencies, but is weighted by the function

$$W(\omega) = \frac{1}{\omega} \ln \left| \frac{\omega + \omega_o}{\omega - \omega_o} \right|$$

which is strongly peaked near ω_o. Thus for frequencies ω_o outside the data range (ω_a, ω_b) or for ω_o near either ω_a or ω_b, we expect a relatively

large error in $\theta(\omega_o)$.

In order to investigate errors of the second type, we express the Kramers-Kronig relation for the phase shift as

$$\theta(\omega_o) = A + \int_{\omega_a}^{\omega_b} \frac{d\ \ell n|R(\omega)|}{d\ \ell n\ \omega} \frac{1}{\omega} \ell n \left|\frac{\omega + \omega_o}{\omega - \omega_o}\right| d\omega + B$$

where

$$A = \int_{o}^{\omega_a} \frac{d\ \ell n|R(\omega)|}{d\ \ell n\ \omega} \frac{1}{\omega} \ell n \left|\frac{\omega + \omega_o}{\omega - \omega_o}\right| d\omega$$

$$B = \int_{\omega_b}^{\infty} \frac{d\ \ell n|R(\omega)|}{d\ \ell n\ \omega} \frac{1}{\omega} \ell n \left|\frac{\omega_o + \omega}{\omega_o - \omega}\right| d\omega$$

For frequencies ω_o which are not near ω_a, the contribution A will be small compared to B. The region $(0, \omega_a)$ may be made small, since data are obtainable in the infrared region, usually to photon energies below 0.1 eV. Then for energies $E = \hbar\omega \geq 2$ eV, the total contribution for the range (0 - 0.1 eV) is usually negligible. Furthermore, at low photon energies the band model makes definite predictions about the behavior of the medium, which may form the basis of an extrapolation. Thus, an insulator is expected to be transparent at energies less than the valence-conduction band gap, while in a metal or semiconductor only the intra-band transitions are allowed. In this latter case the free electron model is applicable, and predicts that the reflectance behaves as $R \approx 1 - \sqrt{\frac{2\omega}{\pi\sigma_o}}$ where σ_o is the d.c. conductivity. In any case, Equation 1-15 demands that $\theta = 0$ at $\omega_o = 0$. The error $A(\omega_a)$, usually negligible for ω_o in the visible and ultraviolet, may be made smaller still by an appropriate

extrapolation.

A more serious problem is the termination at high frequencies. The range of frequencies is infinite, so that even though the weighting function asymptotically decreases to zero, the resulting value of B may be significant. We will show, using data on Cd_3As_2 over the energy interval (0.08, 11.0 eV) that the error incurred in neglecting B (as opposed to making an extrapolation) is quite significant, causing ϵ_1 to change from positive to negative values at an energy of 6 eV. Some assumption must be made for the behavior of the reflectance at higher energies to obtain accurate results for $\tilde{n}$ and $\tilde{\epsilon}$.

Various attempts to extrapolate the reflectance to high energies are surveyed by Stern (16), who nevertheless states "no really satisfactory way to proceed is available when the reflectivity is still varying at the highest frequency attainable." The simplest scheme is to assume a smooth decay at frequencies $\omega > \omega_b$.

If we examine the behavior of the dielectric constant (Equation 1-9) we find that for $\omega \gg \omega_o$ the reflectance decreases as $1/\omega^4$. Thus if data exist for frequencies much greater than the highest absorption line, the extrapolation may be made with a known behavior. When several "resonances" are still contributing at ω_b, the most common extrapolation is to assume

$$R = R(\omega_b)\left(\frac{\omega_b}{\omega}\right)^{\alpha} \qquad \omega > \omega_b \tag{1-17}$$

where α is chosen so that no sharp change of slope occurs at ω_b.

A more sophisticated procedure is described by Roessler (18,19).

Use is made of the generalized mean value theorem

$$\int_a^b f(x)g(x)dx = f(x_o)\int_a^b g(x)dx \qquad a < x_o < b$$

applied to the phase-shift dispersion relation, where a and b are limits on a frequency range where no data exist (i.e., $0 - \omega_a; \omega_b - \infty$) and f is the function representing the (unknown) reflectance. The remaining integral can be evaluated directly. The contribution from low and high frequencies is thus expressed exactly in terms of the reflectance at two frequencies outside the data range. One may obtain a solution for the contributions A and B if the phase shift is known a priori for two frequencies in (ω_a, ω_b). Thus, for an insulator, the phase shift must be zero for energies less than the valence-conduction band gap, and the resulting solution contains no approximations. For semiconductors and semi-metals the points of known phase shift do not exist.

Sum Rule Constraints on the Optical Constants

In general, if a known property of the medium may be used to establish constraints on the phase shift at particular energies, then the adjustable parameters in any extrapolation formula may be chosen so that the calculated phase shift is forced to agree with the constraint. For example, for an insulator, α in Equation 1-17 may be adjusted to give a zero phase shift for energies below the valence-conduction band gap energy. For some materials no energy exists for which the phase shift is known (except the trivial case $\theta = 0$ at $E = 0$). There exist, however, definite constraints on the integral over all photon energies of functions of the

phase shift in the form of sum rules on the dielectric and optical constants.

An examination of the dielectric constant dispersion relations shows that, for frequencies much higher than the highest "resonance,"

$$\epsilon_1(\omega) - 1 = -\frac{2}{\pi}\frac{1}{\omega^2}\int_o^\infty \omega'\epsilon_2(\omega')\, d\omega' \tag{1-18}$$

From the equation relating $\epsilon_1(\omega)$ to the physical properties of the medium (Equations 1-9) under the same conditions we have

$$\epsilon_1(\omega) = 1 - \frac{4\pi N_0 e^2}{m}\frac{n}{\omega^2} \tag{1-19}$$

where N is the atomic density and n is the number of electrons per atom. Since these equations must be consistent, we have

$$\int_o^\infty \omega'\epsilon_2(\omega')\, d\omega' = \frac{\pi}{2}\frac{4\pi N_0 e^2}{m}\, n = \frac{\pi}{2}\,\omega_p^2 \tag{1-20}$$

where ω_p is the plasma frequency. Philipp and Ehrenreich (20) have generalized this relation to apply for a finite frequency range, where not all the electrons are contributing to the absorption. If n_{eff} is the effective number of electrons per atom which may be excited by radiation of frequency ω_o, we may write

$$\int_o^{\omega_o} \omega\epsilon_2(\omega)\, d\omega = \frac{2\pi^2 e N_0}{m}\, n_{eff} \tag{1-21}$$

The relation 1-20 is a form of the so-called "f-sum" rule. There are many such sum rules, all of which may be derived from a "Superconvergence" theorem given by Altarelli et al. (21) which shows that sum rules exist for all functions g(x) which may be written

$$g(x) = P \int_0^\infty \frac{f(y)}{x \pm y} \, dy$$

where f(y) is a continuously differentiable function. The dispersion relations for $\tilde{n}(\omega)$ and $\tilde{\epsilon}(\omega)$ are of this form. Three sum rules (in addition to Equation 1-20) which are of interest are

$$\int_0^\infty [n(\omega) - 1] \, d\omega = 0 \tag{1-22}$$

$$\int_0^\infty \omega k(\omega) [n(\omega) - 1] \, d\omega = 0 \tag{1-23}$$

$$\int_0^\infty \omega k(\omega) \, d\omega = \frac{\pi}{4} \omega_p^2 \tag{1-24}$$

The dispersion relations for the complex reflectance are not of the required form, and no sum rule exists directly for the phase shift. Altarelli remarks on this, observing that such sum rules "would be helpful in performing an extrapolation of R(ω) beyond the measured frequency range." In Chapter III we shall investigate the use of those sum rules which do exist (especially Equations 1-22 and 1-23 which do not demand a knowledge of the effective electron density) in extrapolating the reflectance to high energies. Obviously such integral constraints are not sufficiently

sensitive to construct reflectance curves where data are lacking. However, if the analytical form of the reflectance as a function of energy is assumed, the sum rules may serve to yield the optimum results which this form is capable of giving.

Synchrotron Radiation

Since the calculated dielectric constant at energies of 6 eV has been found to depend on reflectance data at energies above 12 eV (wavelengths shorter than 1000 Å, designated the "extreme vacuum ultraviolet," or XUV region by Samson (21)), a major experimental effort was undertaken to extend reflectance measurements to these high energies. The radiation source employed was an electron storage ring, a source which, along with the synchrotron, is uniquely suited to this spectral region. Electrons moving in a constant magnetic field perpendicular to their velocity are accelerated in circular trajectories (classically) and emit electromagnetic radiation. The radiation is "a glow which immediately originates from the electrons in vacuo; therefore it is not connected with the micro-particles of the environment as is the case for the Cerenkov radiation." (23). The spectral distribution of the intensity as well as the angular distribution and polarization is crucial to the suitability of this "glow" for reflectance spectroscopy.

For a brief description of the properties of synchrotron radiation as they bear upon its suitability as a source for spectroscopy, see Appendix A.

CHAPTER II

APPARATUS AND OPERATIONAL PROCEDURE

Extension of optical measurements into the extreme ultraviolet (wavelengths below 1000 Å) is a relatively new achievement, due in large part to the lack of intense continuous radiation sources in this region. In a published report in 1966 (24) a Solid State Panel Subcommittee investigated the characteristics of synchrotron radiation with particular attention given to its usefulness as a source in the 50-1500 Å spectral region, the "energy starved region of the spectrum." By 1968 several solid state experiments were being conducted at the electron storage ring facility at the University of Wisconsin Physical Sciences Laboratory (UWPSL). A brief description will be given of the operational parameters of the storage ring and auxiliary equipment at the UWPSL facility as they directly bear on this experiment.

The UWPSL Facility

The UWPSL storage ring (25) (which was the source of synchrotron radiation in this experiment) typically stores 2-10 milliamperes of electron current at an energy of 240 MeV. The bending radius of the magnets is 0.54 meter and the cross-sectional size of the electron beam is about 1 mm x 1 mm. Electrons are injected at an energy of 45 MeV from an FFAG synchrotron and accelerated to the final energy whereupon the electrons are "stored." Electrons are continuously scattered from the beam causing

a decay which does not possess a simple exponential time dependence. The decay rate is a strong function of both the pressure in the ring and the beam current; for instance, an injected current of 5 mA may decrease to 2.5 mA in one hour and this to 1.25 mA in two or three hours at a ring pressure of 5×10^{-10} Torr. An increase in pressure to 1×10^{-9} Torr may half these time intervals. Since the intensity of the emitted radiation at any time is directly proportional to the electron current in the ring at that instant, it is necessary to monitor the ring current if meaningful comparisons are to be made of radiation signals taken at different times.

The need for a vacuum path for radiation whose wavelength is less than 2000 Å (the vacuum ultraviolet region) is imposed by the strong air absorption of these wavelengths. In the extreme ultraviolet, the condition of the sample surface imposes even more stringent conditions on reflectance spectroscopy. In addition to the increased smoothness required in this region for specular reflection (the surface roughness must be significantly less than the wavelength of the incident radiation), contamination becomes more important, especially for semiconductors, for which the penetration depth is only a few hundred Angstroms for XUV radiation. Greenaway and Harbecke (14) observe that "The difficulties in obtaining reproducible surfaces which reveal the properties of the bulk material become more severe at shorter wavelengths." One experimental implication is that any undesired surface layer (e.g. vacuum pump oil or oxide film) may contribute a significant portion of the reflected signal. An ultra-high vacuum environment for the sample is therefore desirable.

One of the experimental difficulties encountered in the XUV is the

lack of a window material. Samson (22) states that "below 1040 Å no window material transmits radiation," which implies that a single vacuum must enclose the source, any focusing and monochromating elements, and the sample-detector system. In this respect the ultra-high vacuum of the storage ring enhances its suitability as an XUV source.

The path traveled by the radiation from its origin in the storage ring to the detector is shown in Figure 1. The major components of the vacuum system in addition to the storage ring were a mirror chamber, a monochromator, and our experimental chamber. These sections were connected by straight-line valves and each possessed ion pumping sufficient to maintain ultra-high vacuum. The roughing pumps employed were chemical sorption pumps, thus the entire vacuum system was oil-free.

The mirror-separation chamber was designed by H. Fritzsche and U. Gerhardt and contained a grazing incidence mirror in the shape of a section of an ellipsoid. The angle of incidence was about 80° from the surface normal. An image of the source, which was a section of the electron orbit, was formed at the entrance slit of the monochromator. The image size was 1/4 the size of the source. The divergence was such that the ruled portion of the diffraction grating in the monochromator was fully illuminated.

The monochromator (26) was designed by C. Pruett and N. Lien of the UWPSL. The optical system closely resembles the McPherson 225 one-meter normal incidence monochromator. The diffracting element used was a gold-coated tripartite reflection grating with a one meter radius of curvature blazed at 800 Å. The wavelength selection was done by a movement of the grating, an adjustment designed to consist of two independent

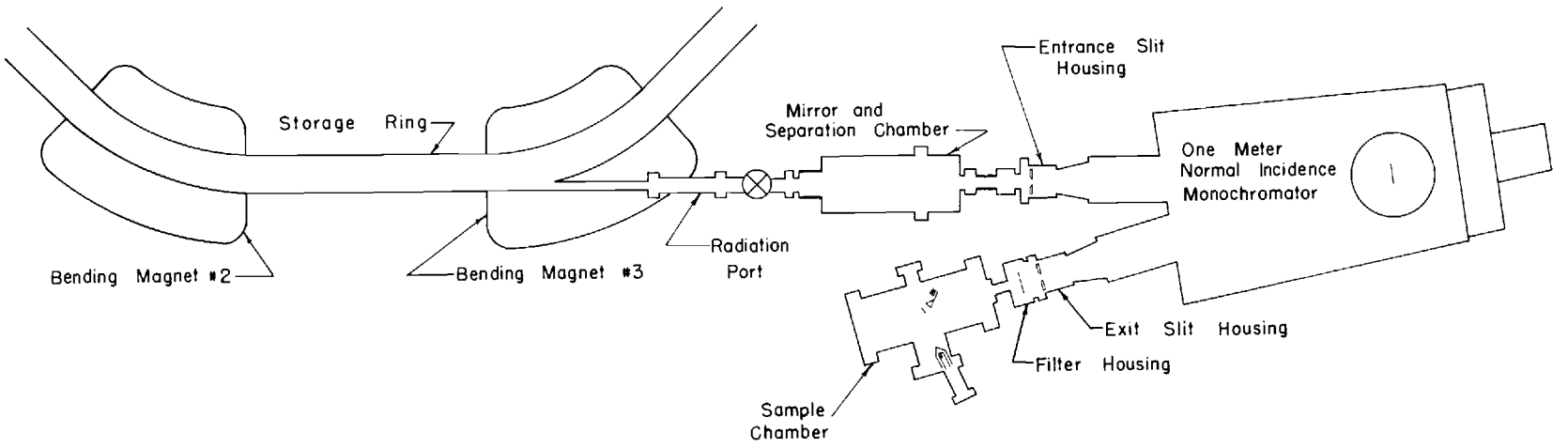

Figure 1. Overall View of Major Experimental Apparatus on the Northwest Port of the UWPSL Storage Ring

motions. The first was a rotation of the grating about a vertical line lying in the plane of the face while the second was a translation along a line bisecting the angle formed by an incident ray and the ray passing through the exit slit. This linear motion maintained a vertical line focus at the exit slit. The motions were achieved by two stepping motors which were capable of manual operation or remote operation by an on-site PDP-12 computer.

An experimental chamber was designed to allow independent mobility of the sample and detector so that the incident and reflected radiation might be measured. Ion pumping was used to give an oil-free ultra-high vacuum environment. In addition to the photon optics an electron optical system was incorporated to allow detection of contamination of the sample surface.

Experimental Chamber Design

The experimental chamber was a modification of a standard vacuum "cross" with four main arms which were 6 inch O.D. tubing and terminated in ports with 8 inch O.D. flanges. The modification consisted of the addition of a 6 inch O.D. flanged port at the center of the cross oriented perpendicular to the main arms and two 2 3/4 inch O.D. flanged ports on the opposite side. During operation the chamber was oriented so that the centerline of the two tubes forming the main arms of the cross defined a vertical plane. The optical axis coincided with the horizontal centerline and the sample position was the intersection of the two centerlines at the chamber center. The chamber was maintained at ultra-high vacuum by two Ultek double-ended 150 liter/sec differential ion pumps which possessed

8 inch O.D. flanged ports on each end. So that there would be no direct-line path from the titanium elements of the pumps to the sample or detector, a second, unmodified "cross" was employed as an intermediate vacuum chamber between the pumps and the experimental chamber. The experimental chamber and pumping system are shown assembled in Figure 2. The auxiliary cross as well as the experimental chamber and the pumps was constructed from 304 stainless steel. The entire experimental system was supported by a platform built from 1 inch thick boiler-plate steel with several 4 inch I-beams welded length-wise to the base. This support stand proved capable of holding the system in optical alignment for the several weeks during which the system remained coupled to the monochromator.

The weights of the support stand and the assembled experimental system were approximately 625 lb and 450 lb, respectively. The support stand rested on three legs which were 1 inch diameter threaded steel rods which screwed through the base and whose lower ends lay in machined grooves in a base-plate assembly designed by R. N. Dexter. This assembly consisted of a lower plate which was fixed relative to the floor and upon which an upper plate "floated" by means of ball bearings. The upper plate was allowed a pivotal motion (with respect to the lower plate) about a fixed point of the bottom plate. This pivot point was adjustable by about ± 1 inch in each of the X and Y horizontal directions, and could be located directly under the monochromator exit slit. The possible motions of the assembly were then (1) a pivot about the exit slit, (2) height adjustment achieved by uniformly extending or retracting the legs of the support stand, and (3) "pitch" and "roll" adjustments obtained by adjusting independently the extension of each of the three legs.

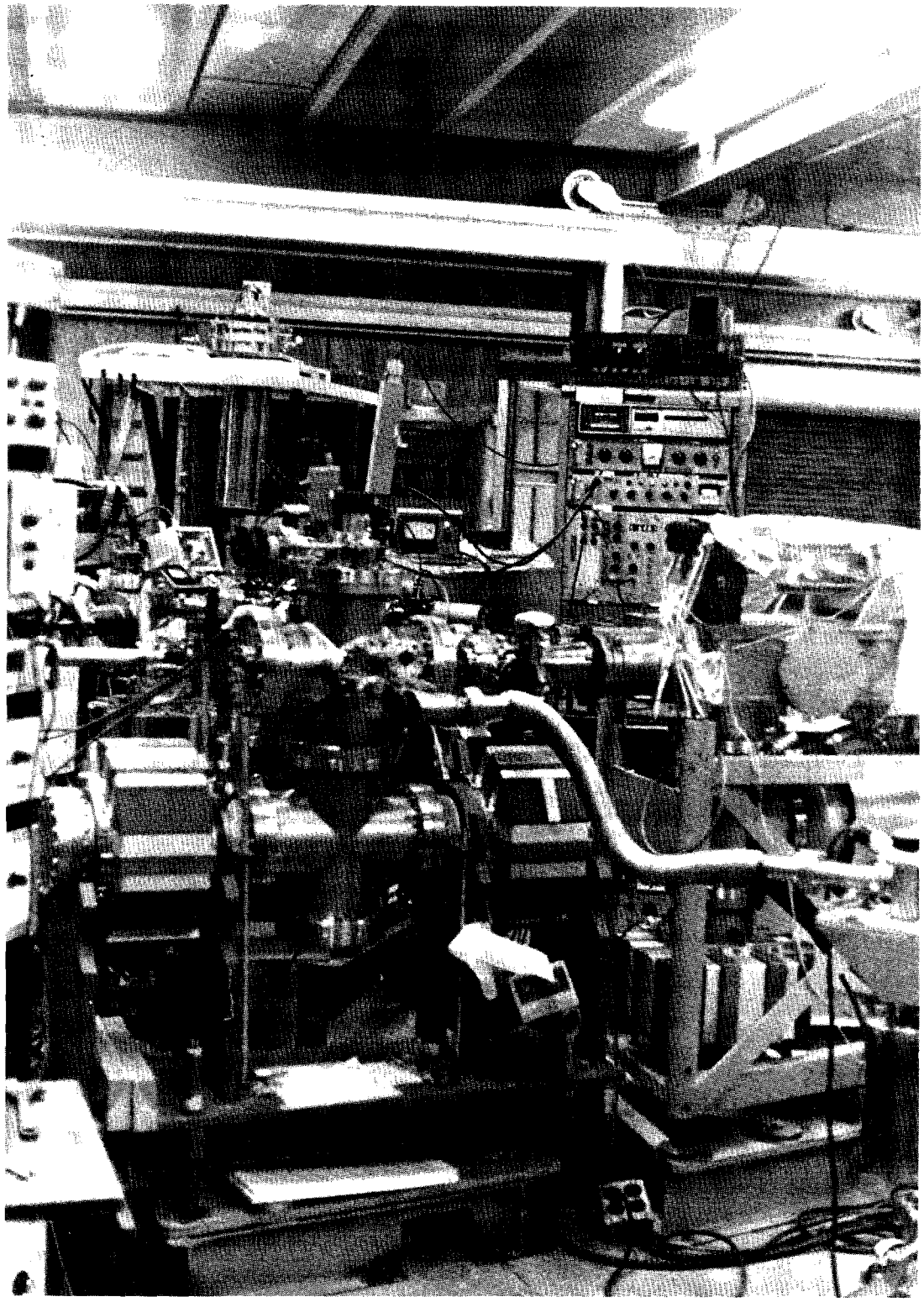

Figure 2. Experimental Chamber During Operation (the monochromator is to the right)

Values of the reflectance of a sample were obtained by two measurements; that of the incident radiation intensity I_o, and that of the radiation intensity reflected from the sample surface RI_o. During the measurement of RI_o the sample surface occupied the center of the experimental chamber, the surface normal oriented at some small angle (which was less than 20° for normal incidence reflectance) with respect to the incident light. The detector was positioned to intercept the reflected radiation. For the incident intensity measurement the sample was moved in order to allow the incident light to pass unobstructed into the detector. The motions involved were a rotation of the sample (to select the angle of incidence) about a vertical axis through the center of the chamber, a rotation of the detector about the same axis, and a vertical translation of the sample in and out of the optical beam. In this way the optical path length from the monochromator exit slit to the detector was the same for the (diverging) beam in each configuration. This was desirable in that it resulted in the illumination of the same size area on the detector for both measurements thus eliminating differences in the two signals due to "hot spots" or selective saturation of a particular area of the photosensitive surface.

The sample, detector, electrical leads connecting the sample and detector with the electronics outside the vacuum, and the manipulatory apparatus were all supported on a single 8 inch O.D. flange, so that the entire assembly could be removed as a unit. The flange is shown in Figure 3. This flange was bolted to the top of the experimental chamber during operation. The combination of linear and rotational motion of the sample was obtained by bolting an Ultek direct-drive rotary vacuum

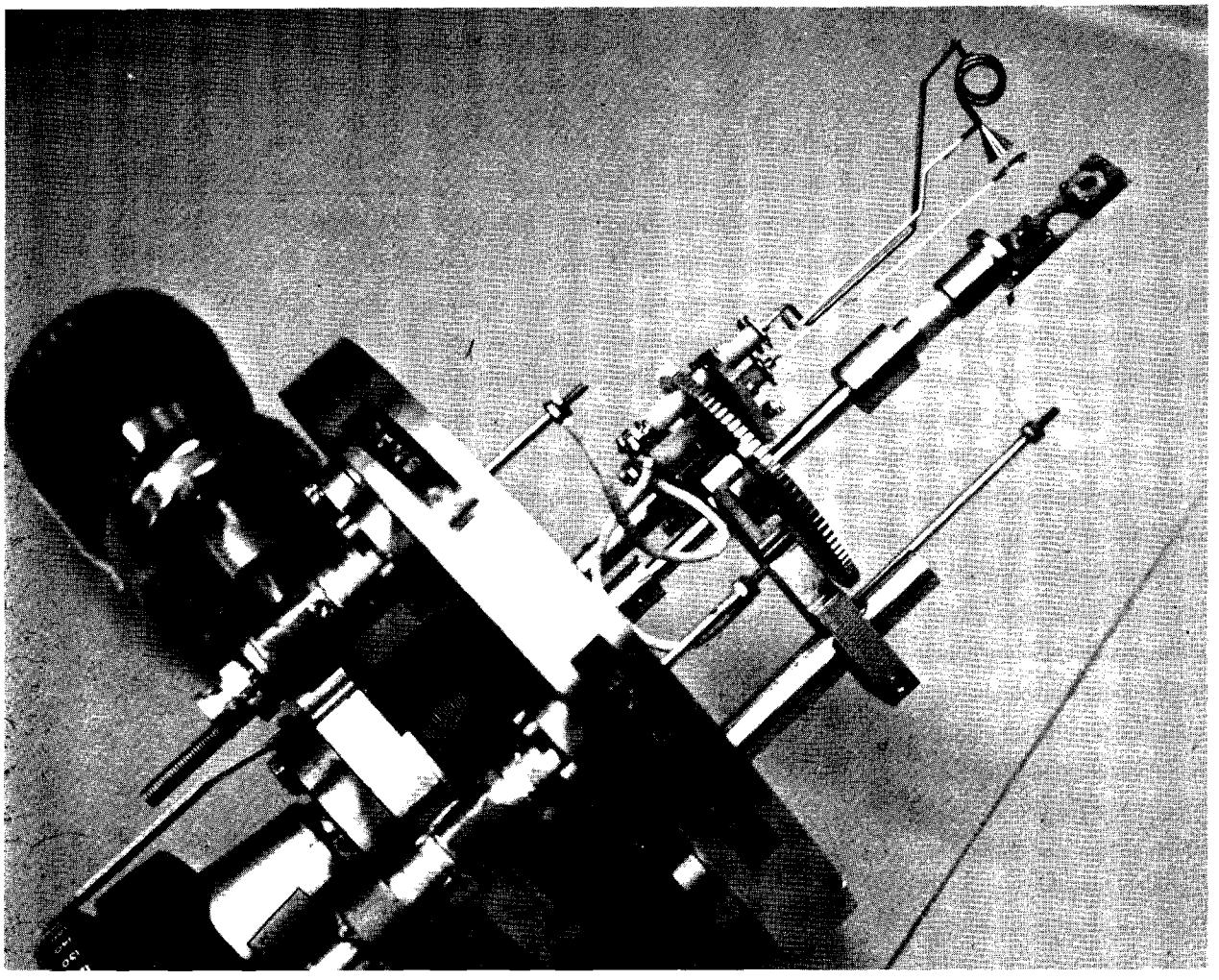

Figure 3. Sample-Detector Manipulation Flange

feedthru on a 4 1/2 inch O.D. flange which was attached to the 8 inch O.D. flange by a bellows. The bellows was welded to both flanges and the flange separation was determined by three fine-threaded (1/4 inch - 28) posts which were screwed into the 8 inch O.D. flange and along which the smaller flange was free to travel subject to lock nuts which held it at a chosen distance from the 8 inch O.D. flange. Linear motion was achieved by extension and compression of the bellows, and was independent of the rotation of the rotary feedthru. About 1 inch of linear travel was possible. A sample holder was mounted directly on the end of the (extended) rotary feedthru, whose extended length was 8 1/2 inches. In order to eliminate wobble, a ball bearing was used to guide the extension rod (which connected the feedthru with the sample holder) in its rotary and linear motions. The sample holder was designed to hold two samples separated by a distance of 7/8 inch along the axis of the extension rod, so that either sample could be positioned in the beam by the linear motion described above. Between the two samples was a 3/8 inch diameter clearance hole which allowed the radiation to pass unobstructed. The sample holder was coupled to the extension rod through a commercial ceramic-to-metal seal which electrically isolated the sample holder by a 3/8 inch alumina rod. The sample could thereby be maintained at a floating potential relative to the chamber without use of organic insulating material. A cutaway drawing of the sample chamber interior is shown in Figure 4.

The samples under study in this experiment were in the shape of discs 6-10 mm diameter and 1-2 mm thick. These samples were mounted on the face of stainless steel blocks. They were supported on one side by a

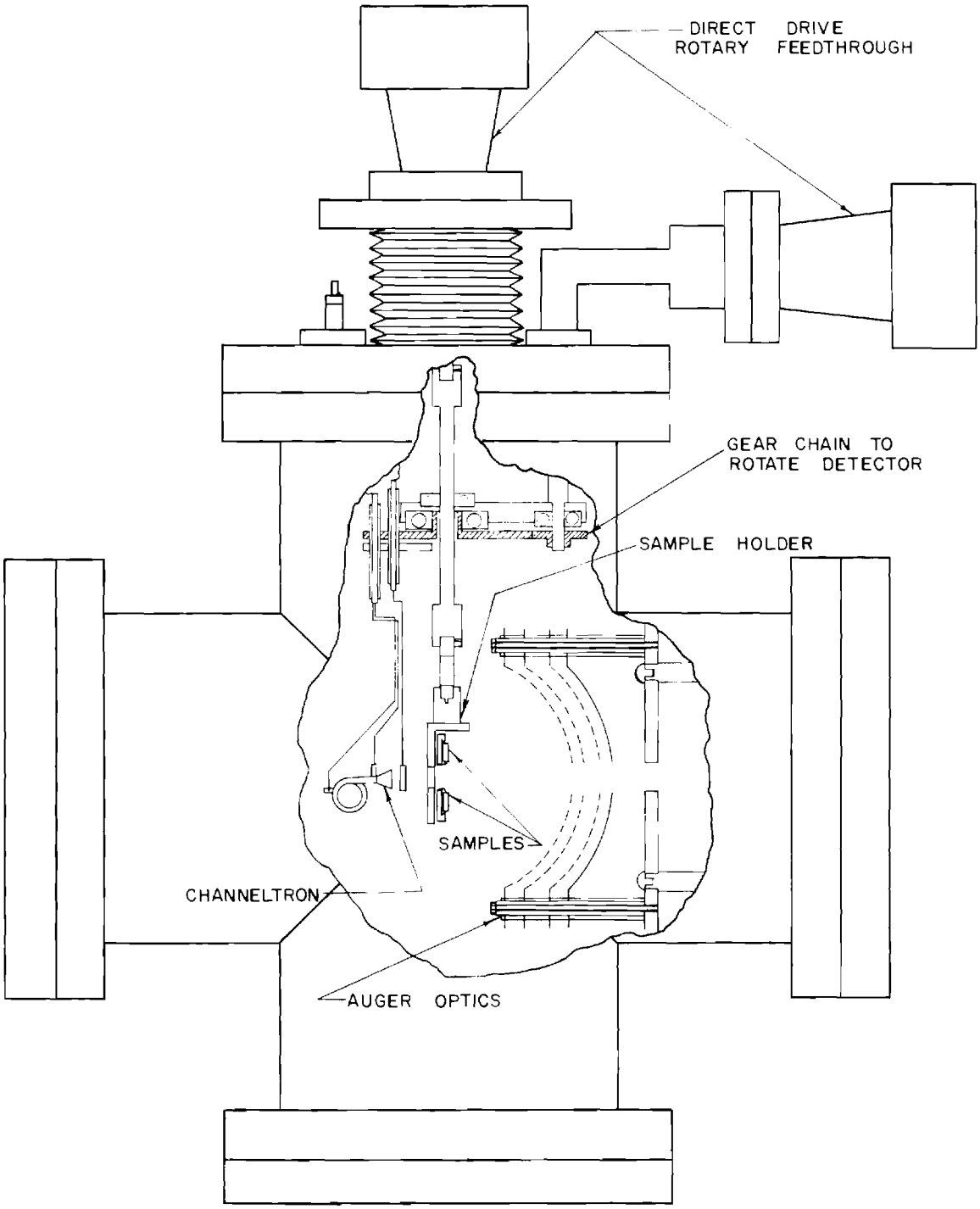

Figure 4. Cutaway of the Experimental Chamber

knife-edged shoulder in the shape of a 60° "Vee" machined on the block's face, and pressed from the opposing side by a spring clip which was clamped to the block by a screw. The block was held away from the sample holder by a tungsten coil spring and retained by three number 0-80 screws; an arrangement which allowed alignment of the samples so that the rotational axis of the rotary feedthru (and the extension rod) lay in the plane of the sample surface. Good electrical contact existed between the sample and sample holder, and no chemical adhesives were used. The sample holder, rotary feedthru, extension rod, bellows, and flanges were stainless steel. Stainless 304 was used where possible for its good vacuum properties. More than 95% of the interior surface area of the chamber was 304 stainless steel.

The photon detector chosen for the experimental chamber was the Bendix Channel Electron Multiplier (channeltron) which consists of a hollow glass tube coated inside with tungsten and bent into the shape of a spiral. The Bendix model 4028C used in our experiment had an 8 mm diameter cone which served as a photosensitive surface at the front end of the channel and a metallic cap which acted as a current collector in the rear of the channel. Nickel ribbon electrodes were spot-welded around the channel at the cone and at the rear cap. The signal was taken from the rear electrode which was maintained at 3.0 kilovolts positive relative to ground while the cone was held at 0.5 kilovolt negative relative to ground. A fine (100 mesh) tungsten screen was placed in front of the cone at a distance of about 1 mm and electrically connected to the cone in an attempt to equalize the potential across the surface of the cone and thus to eliminate "hot spots" due to possible inhomogeneities in the

tungsten coating. The optical transmission of the screen was about 80%.

The channeltron was mounted by the nickel electrodes which were spot-welded to heavy (.045 inch diameter) stainless steel wires which were in turn spot-welded into 1/8 inch diameter stainless steel rods. The wires provided electrical contact as well as physical support and were bent to avoid contact with other apparatus in the experimental chamber (especially the electron energy analyzer). The 1/8 inch support rods were held in alumina tubes by snap rings which fit grooves in the rods just above and below the ceramic. The rods protruded about 1/4 inch above and below the alumina tubes. There were three ceramic tubes containing rods for the wires leading to the front and rear of the channeltron and to the screen. Each tube passed through a hole in a 1/8 inch thick 304 stainless steel plate to which the tube was rigidly fixed by snap rings which gripped the alumina above and below the plate. The plate was thus electrically isolated from the detector and screen. Five number 4-40 screws held the plate about 3/16 inch from and roughly parallel to a gear (whose support will be discussed shortly) in which clearance holes were drilled for the three alumina tubes. Two of the number 4-40 screws passed through clearance holes in the plate and were screwed into tapped holes in the gear, while three were screwed through tapped holes in the plate and tightened against the gear. The separation of the plate and gear as well as the relative orientation of the two were adjustable by means of these screws and this adjustment was transmitted to the channeltron. The relative tilt possible between the plate and gear was about 10° in any direction and this was sufficient to finely position and orient the channeltron,

which was held about 5 inches from the plate.

The ends of the 1/8 inch diameter rods protruding from the alumina tubes on the side of the gear opposite the channeltron were threaded and .015 inch diameter bare copper wire was attached by being squeezed between two nuts. The copper wire passed to high-vacuum electrical feedthrus which were bolted onto the 8 inch O.D. flange. The wire was insulated with alumina bead and was thus flexible during the rotation of the gear.

The above construction allowed the channeltron to be electrically accessed from outside the vacuum while all electrically active components were insulated during the necessary movement of the channeltron. This was achieved using only stainless steel and alumina materials (except for the copper wire), a desirable feature for an ultra-high vacuum system.

Physical support for the above-mentioned gear was a stainless steel bracket 1/4 inch thick and 1 inch wide. The bracket was screw clamped to a 1/2 inch diameter post which was welded into the 8 inch O.D. flange. The bracket held two ball bearings whose outer races were pressed into recesses in opposite sides of the bracket. Both bearings were concentric about the sample holder axis of rotation. One bearing guided the rod (earlier referred to as the "sample holder extension rod") which connected the sample holder to the rotary feedthru. The hub of the gear carrying the channeltron was pressed into the 3/4 inch I.D. inner race of the second bearing, while the sample holder extension rod passed freely through a clearance hole in the center of the gear (Figure 4). This design allowed the sample and detector to rotate independently about the same axis, and the sample to be translated along this axis. The sample possessed 360° rotation which was limited only by any wires which might

be attached to it. A total rotation of the channeltron by 210° was possible, a limit imposed by the obstruction of the bracket which made contact with the alumina tubes at the extremes of rotation. The actual rotation of the channeltron support gear was done by a small driver gear which was chosen to be of the anti-backlash type since the meshing of the two gears was the sole constraint upon the channeltron's rotation. The driver gear was coupled (through a matched pair of miter gears) to a second Ultek rotary feedthru mounted on the 8 inch O.D. manipulation flange.

Filtration and Collimation of the Light

The radiation passing through the monochromator exit slit was further collimated and filtered before reaching the sample position. Light diverged from the exit slit with a half-angle of about 2°50' in the horizontal plane and about 1°26' in the vertical, illuminating an area approximately 1" by 1/2" at the sample position, which was 12 inches from the exit slit of the monochromator. To limit the beam to the sample, masks were placed about 3 inches from the exit slit. The masks also served the function of holding filters which selectively blocked higher order light from the grating. It is a characteristic of diffraction gratings illuminated by white incident light that the constructive interference peak in the first-order spectrum for a wavelength λ coincides exactly with second-order peak for the wavelength $\lambda/2$, the third order peak for $\lambda/3$, etc. Thus the light passing through the monochromator exit slit consists not purely of the selected wavelength, but contains contributions of shorter wavelengths. The relative amount of higher-order contributions

depends upon the wavelength distribution in the incident light and on the reflectance of the grating at various wavelengths. For a grating blazed at 800 Å, the amount of light reflected at wavelengths less than 400 Å is negligible (in the first order spectrum it was found to be less than 2% of that reflected at 600 Å). At longer wavelengths, however, filtering is necessary to insure monochromaticity in the reflected radiation. A lithium fluoride window was used to filter light of wavelengths longer than 1040 Å, since no light of shorter wavelength is transmitted by this material (no data were collected beyond 2000 Å). Below 1040 Å no bulk material is a good transmitter of radiation, but thin films of certain metals possess transmission "windows" in this region. In our particular case, an evaporated film of indium about 3000 Å thick was used to select light of wavelengths between 800 Å and 1040 Å. This filter possessed a window from about 740 Å to about 1000 Å (there was no sharp upper cut-off) wherein the transmittance was between one and five percent. Since this region is one of high intensity in the beam emerging at the exit slit, ample radiation at the sample was obtainable by suitably adjusting the monochromator slit widths.

A cylindrical housing 5 1/2 inches in diameter was constructed for the masks and filters and to furnish a continuous vacuum path from the monochromator to the experimental chamber. The axis of symmetry of the cylinder coincided with the optical axis of the chamber, i.e. was the path traveled by the incident radiation beam. A flange configuration was machined on one end of the housing, compatible with the viton gasket seal which existed at the exit slit of the monochromator. The other end of the

housing was closed except for a bellows whose clear inner diameter was 1/2 inch and whose outer diameter was 1 1/4 inches, and which was welded to the housing concentric with the axis of symmetry. The free end of the bellows was welded into a standard high-vacuum 2 3/4 inch O.D. flange which was bolted onto the 8 inch O.D. flange on the forward arm of the experimental chamber. The housing was pumped from either end by the ion pumps on the monochromator and experimental chamber. Figure 5 shows the filter housing during the experiment.

Since more than one filter material was to be used, several collimation holes were drilled in a 2 1/2 inch P.D. miter gear which became the masking element. These holes were .027 inch in diameter and resulted in an illuminated spot approximately 2 1/2 mm in diameter at the sample position. Each hole was countersunk on the side of the gear away from the monochromator to avoid scattered light from the hole walls. Four holes were drilled in the gear; they were placed symmetrically 90° apart with the centers lying 3/4 inch from the center of the gear. Three of the four were collimation holes as described above and had tapped holes nearby so that filters could be screw clamped in place. The fourth hole was 3/8 inch in diameter and allowed the radiation to pass unobstructed into the experimental chamber for alignment purposes. The masking gear is displayed mounted inside the housing in Figure 6. The axis of rotation of the masking gear was parallel to the optical axis and 3/4 inch away from it. To mount the gear the outer race of a stainless steel ball bearing was pressed into a recess machined in the gear. The inner race was slipped over a 1/4 inch diameter threaded post which was welded into the housing wall. The post possessed a collar which made contact with both

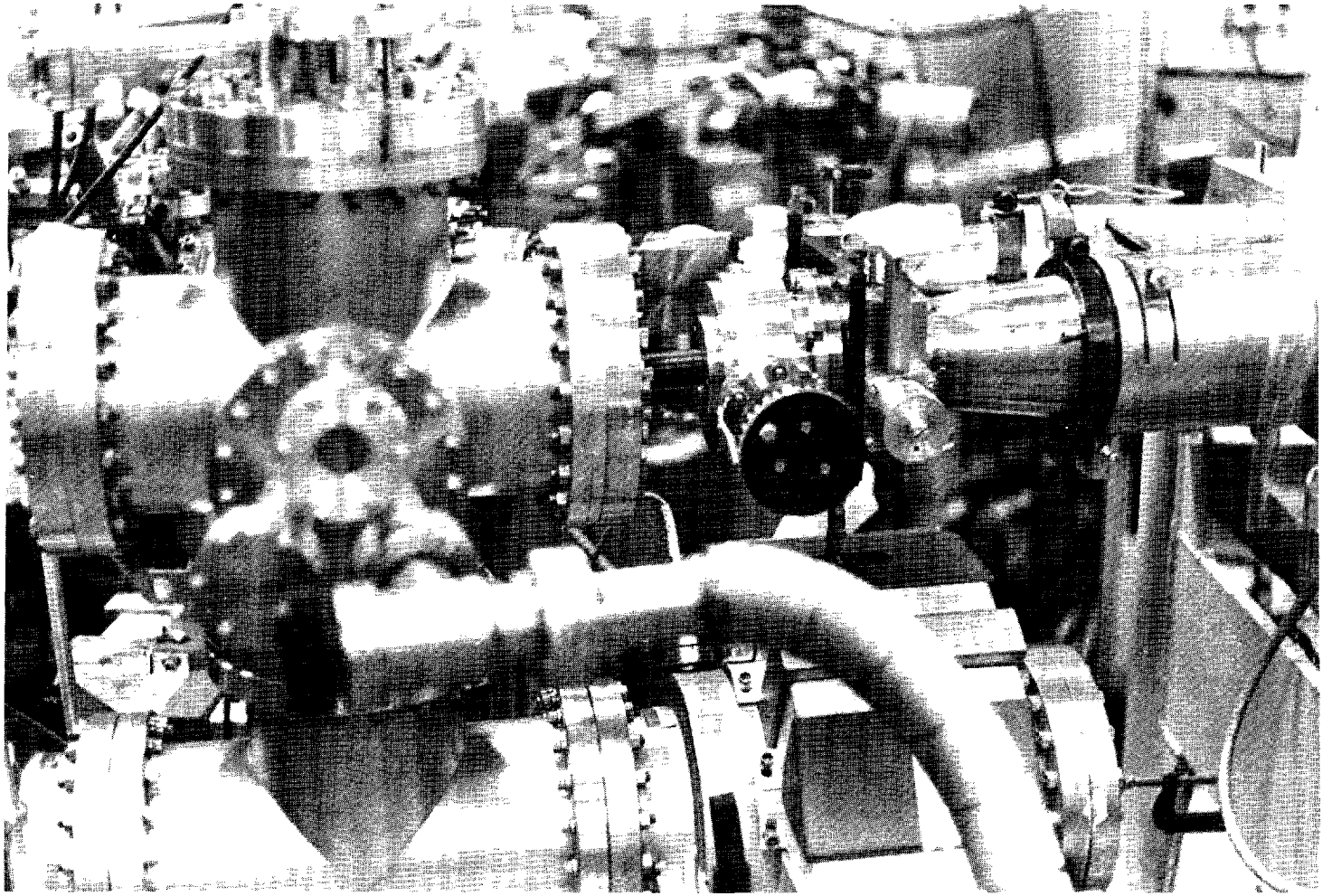

Figure 5. Experimental Chamber, Filter Housing, and Monochromator Exit Slit Housing (left to right) On-Line During Operation at UWPSL Storage Ring

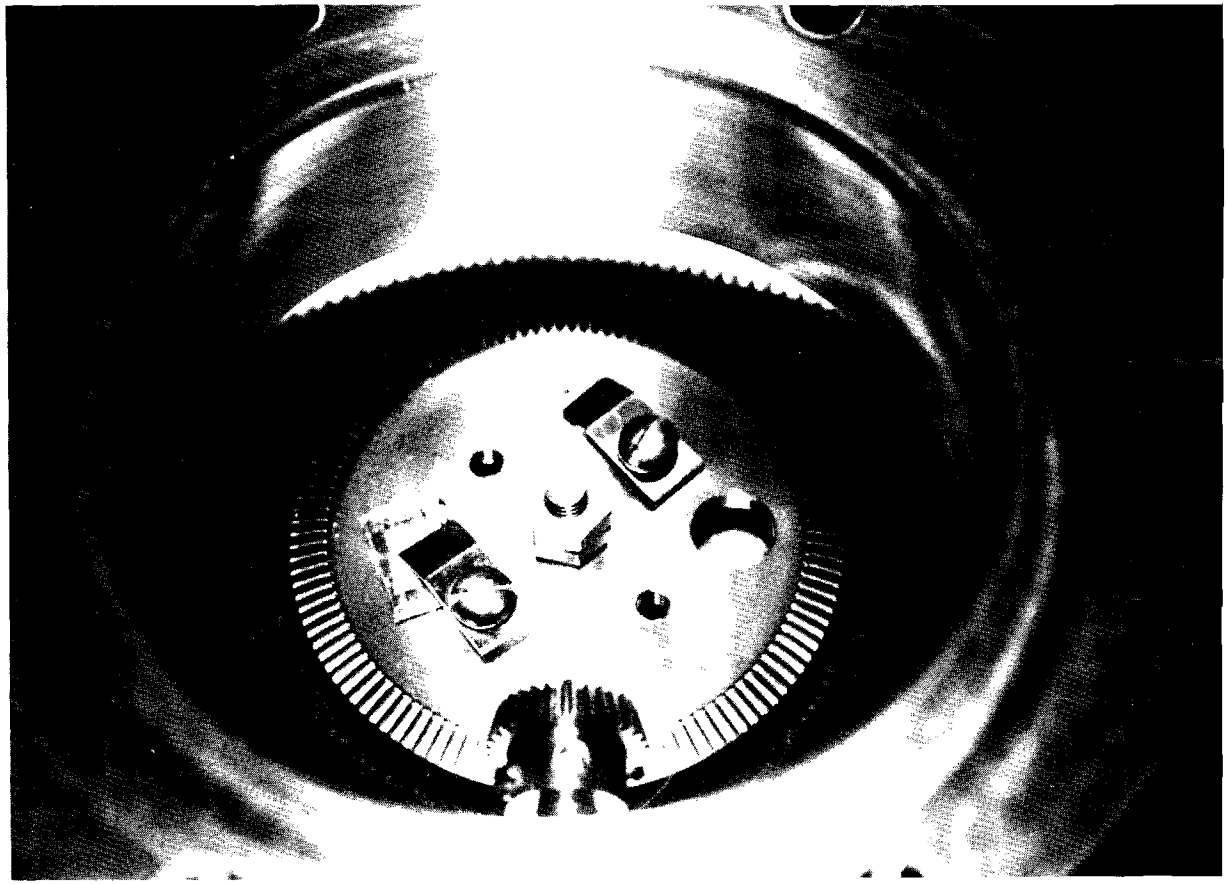

Figure 6. Filter Housing Showing Gear Used to Mount Optical and Limiting Apertures

the inner and outer races of the bearing. Rotation of the outer race (i.e. the gear) was thus opposed by a frictional force. A thin steel ring slipped over the post and pressed the inner race of the bearings against the collar as it was pressed from the other side by two lock nuts which rode on the post. By adjusting the lock nut pressure on the ring the torque necessary to turn the gear was selected. Some friction was essential because small uncontrolled movements of the gear produced magnified changes in the position of the incident radiation at the sample, an effect which could not be tolerated. The masking gear was driven from outside the vacuum by a matching 5/8 inch P.D. miter gear fastened by a set screw to an Ultek direct drive rotary feedthru which was bolted on the side of the housing. The gear ratio was 1:4; thus a complete revolution of the feedthru resulted in a change of filters.

The lithium fluoride filter was a commercial window 1 mm thick which was held over one of the collimation holes. Indium filters were produced by vacuum evaporation of 99.99% pure indium onto a glass slide which had previously been coated with a solution of sugar and a potassium based soap, then dried. After evaporation the film on the slide was scored with a sharp tool, which cut the film into patches approximately 1/4" x 1/4". Upon careful immersion in a distilled water bath, several of the patches floated free of the slide and were fished from the surface with small pieces of 100 mesh tungsten screen. After drying each potential filter was inspected for pin holes, then clamped carefully to the gear so that a portion of the thin film with no pin holes lay over a collimation hole in the gear. Although the failure rate was quite high

(≈ 90%), several good filters were obtained.

The design allowed data to be taken on a sample over the entire wavelength range of interest without breaking vacuum, and permitted samples to be changed and the new samples optically aligned necessitating the removal of only the sample manipulation flange.

The Auger Spectrometer

Auger electron spectroscopy provides a sensitive means of detecting and identifying contaminants on the surface of a material. Incorporation of an Auger spectrometer was a consideration in the initial design of the experimental chamber and influenced the choice of optical components, particularly by imposing spatial restrictions. Auger spectroscopy in general consists of the creation of ionization in the inner electron shells of atoms lying on or near the surface of a sample and an energy analysis of the secondary electrons emitted. Auger electrons (see Appendix B) are not true secondaries but possess a weak discrete energy spectrum which is superimposed on the broad continuous (and much stronger) spectrum of the true secondary and inelastically scattered primary electrons emitted from the surface. Detection of Auger signals is difficult at best, and attention must be given to the elimination of sources of noise even in the early stages of design and in the choice of the electronics employed.

Ionization of the surface atoms was produced by an impinging beam of high energy (about 2.2 keV) electrons. A Superior model SE-3K-5U electron gun was modified by the installation of a tungsten filament so that it could be repeatedly exposed to the atmosphere without damage. The resulting gun was mounted on a Varian 8-pin high-vacuum feedthru and

is shown in Figure 7. Electrons that were thermally emitted from the heated filament, which floated at high negative potential relative to ground, were focused by an Einzel lens and directed by two pairs of deflector plates. The final pair of deflector plates was about 2.5 inches from the sample.

A retarding potential energy analyzer based on a design of L. N. Tharp and E. J. Scheibner (27) was built on an 8 inch O.D. flange. Three grids of 100 mesh gold-coated tungsten wire cloth were molded into spherical sections and spot-welded on stainless steel rings. Holes in the rings slipped over posts which were 1/8 inch steel insulated by 1/4 inch O.D. alumina tubing. The rings were separated by 3/8 inch O.D., 1/4 inch I.D. alumina tubing, thus each grid was electrically isolated from the others and from the experimental chamber. The grids were located so that the sample position coincided with the center of the spherical grids, whose radii of curvature were 2 5/16, 2 13/32, and 2 1/2 inches, respectively. Concentric with the three grids was a stainless steel screen which acted as a collector for the secondary electron current emitted from the sample. Its spherical radius of curvature was 2 3/4 inch and its concave surface was coated with G.E. P-4 phosphor which aided in aligning the sample to maximize the secondary electron signal. The solid angle subtended by the screen at the sample was $2\pi/3$ steradians. Each grid and the screen were electrically connected to a high-vacuum electrical feedthru which was bolted on the 8 inch O.D. flange supporting the electron detector assembly. The flange and detection optics are shown in Figure 8. On the outside of the flange each feedthru was terminated in an MHV connector. The solder joint and feedthru were enclosed in an RF shield to

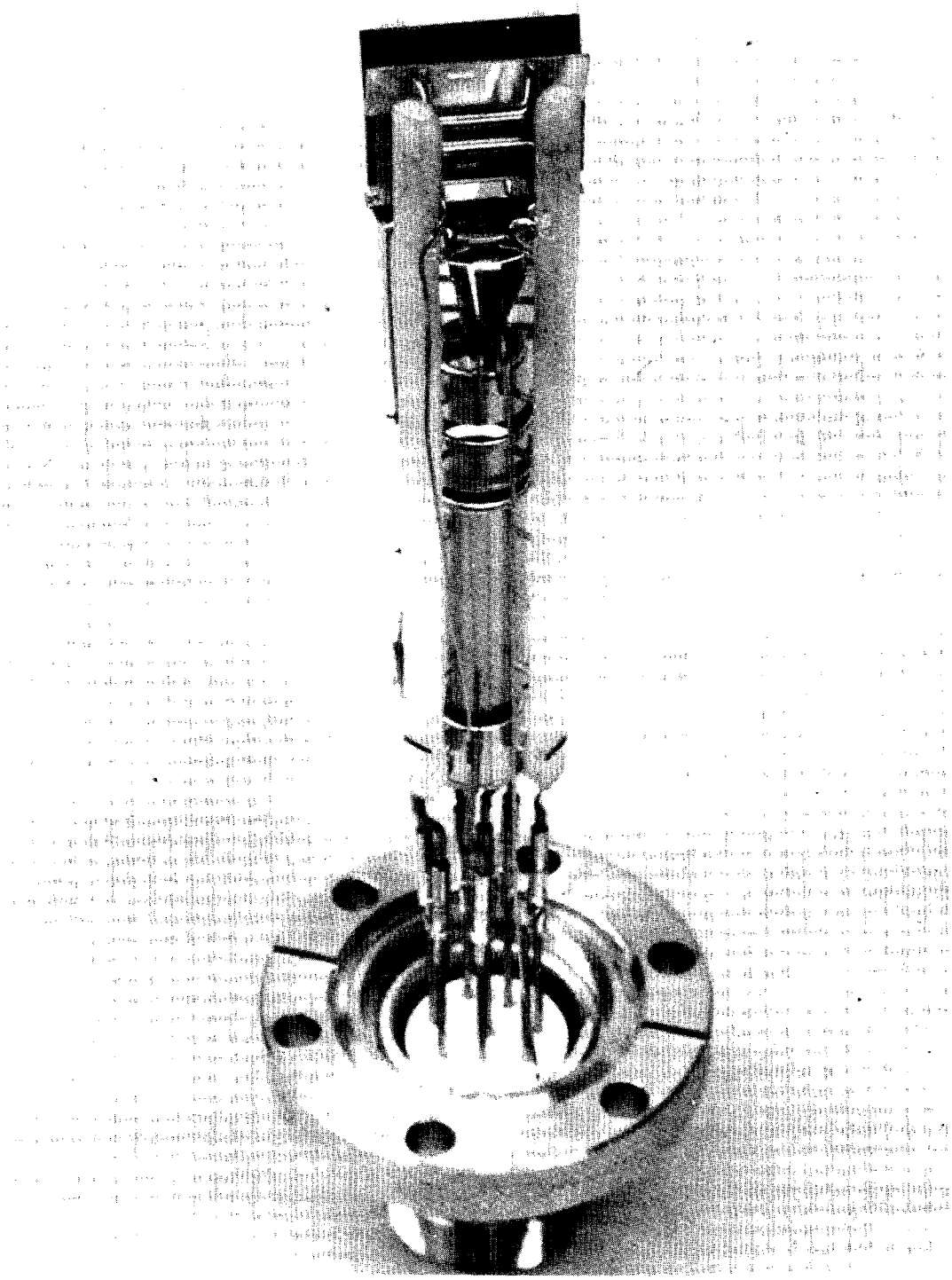

Figure 7. Auger Electron Gun Assembly Mounted on 2 3/4 Inch Flange

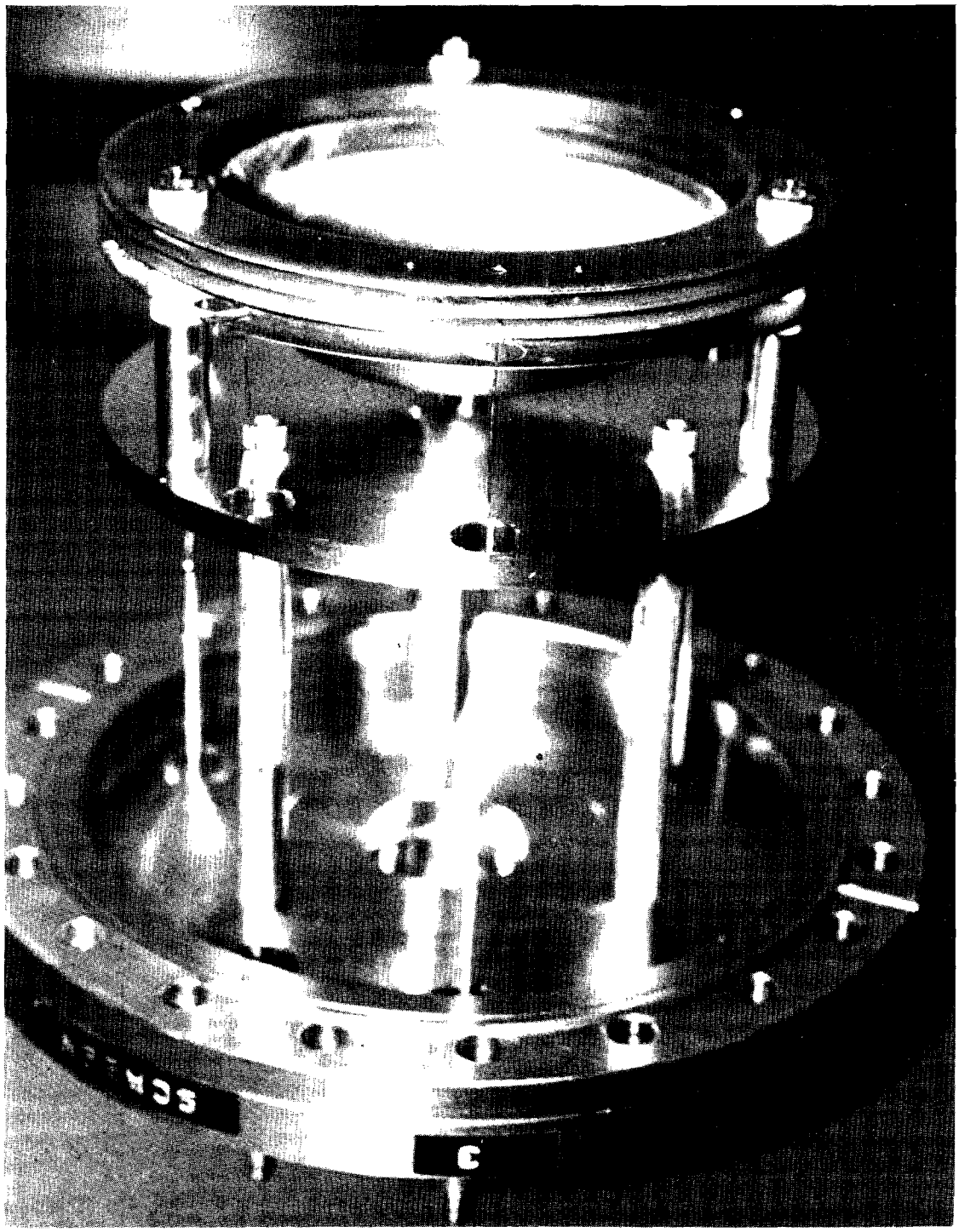

Figure 8. Retarding Potential Electron Energy Analyzer for the Auger Optics Mounted on 8 Inch Flange

eliminate noise.

During the experiment the electron energy analyzer occupied the "front" arm of the experimental chamber as indicated in Figure 4, so that the optical beam passed through the center of the grids and screen. A 1/2 inch diameter hole was punched in the center of the screen and grids to allow the light to pass. The 8 inch O.D. flange containing the energy analyzer possessed a 1 inch diameter hole in its center surrounded by a standard high-vacuum seal configuration machined to mate with a 2 3/4 inch O.D. flange. The electron gun was "side" mounted at an angle of 80° from the optical axis. The relative orientation of the gun, sample, channeltron detector, and energy analyzer for the secondary electrons is shown in Figure 9.

Operational Procedure

The experimental procedure may be described in terms of (a) optical alignment of the system, (b) sample preparation and operation of the optical reflectometer, and (c) Auger characterization of the sample surface. A more detailed treatment of the problems encountered in the preparation of the sample is given in Appendix C, since it is believed that the surface conditions imposed the final limit on the accuracy of the reflectance data.

A. Optical Alignment

Alignment of the optical system proceeded from the storage ring to the sample and detector. Light emitted tangentially to the electron orbit was accepted by the ellipsoidal mirror and focused on the entrance slit of the monochromator. The monochromator was mounted on a base con-

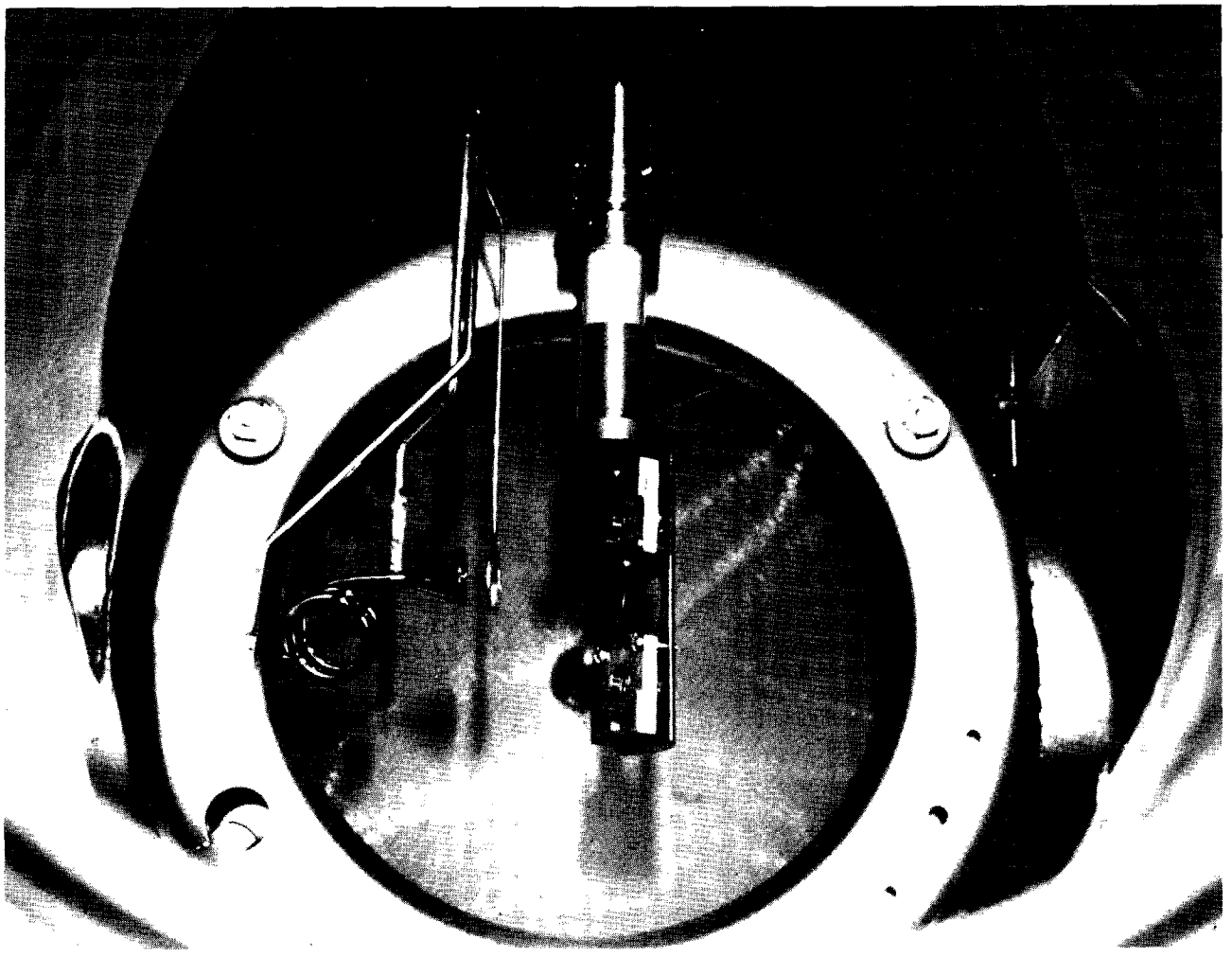

Figure 9. Interior of Experimental Chamber Showing Sample Holder, Detector, and Electron Energy Analyzer (the electron gun is side mounted to the right and cannot be seen)

structed so that it could be pivoted about a point directly under the entrance slit, and raised or lowered as necessary. These adjustments were used initially to fill the ruled portion of the grating with the light passing through the entrance slit and were performed some weeks prior to our arrival. Vacuum was not broken on the monochromator or the mirror chamber during our visit. Some fine adjustments were made, however, by using a photomultiplier tube mounted directly on the exit slit housing and adjusting the monochromator position to maximize the first-order diffracted intensity at the exit slit. This was possible because the exit slit housing was separated from the body of the monochromator by a valve which, when closed, positioned a LiF window in front of the exit slit. Thus, zero-order visible light and first-order diffracted ultraviolet light to a lower wavelength limit of 1040 Å were available without evacuation of the exit slit assembly.

The experimental chamber and associated pumps were assembled and placed on the support stand. The entire assembly was then positioned on the base plate whose pivot point had previously been located directly under the monochromator exit slit with the aid of a plumb line. The zero-order visible beam was used to define the optical axis, and the pivotal motion as well as the height adjustments of the support stand legs was used to move the system so that the symmetry axis of the experimental chamber coincided with the optical axis. The masks and filters were mounted and the housing containing them bolted into place on the monochromator. Fine adjustments were made in the positioning of the sample and detector so that the entire visible beam was intercepted. The

divergence of synchrotron radiation depends upon wavelength in such a way that ultraviolet light is fully intercepted by the sample if visible light is.

Samples of $Cd_xZn_{3-x}As_2$ alloy were obtained saw-cut from the grown ingot. The samples were polished with 1.0 micron alumina grit until all evidence of the saw was removed. The samples were sufficiently soft that the 1.0 micron polish removed stock and about one hour of wheel polishing was usually enough. An intermediate polish of 0.25 micron diamond was used until the scratch marks left by the 1.0 μm polish were removed, then 0.05 μm alumina was used as a final polish. A phase-interference microscope was used to ensure that no scratches from the diamond particles remained on the surface. The polishing was done at Georgia Tech.

Immediately before being placed in the sample holder, some of the samples were etched with a 5% solution of bromine in methanol and rinsed in acetone and methanol. The samples were then mounted on the stainless steel blocks described earlier in this chapter and the blocks attached to the sample holder. While the system was at atmospheric pressure, repeated corrections were made on the orientation of the blocks to insure that the zero-order visible light was fully intercepted by the sample and by the channeltron in both positions.

B. Operation of Optical Reflectometer

The experimental chamber was evacuated using aspirator and sorption pumps and, finally, ion pumps. During the start of the ion pumps, the sample holder, both ends of the channeltron, and the Auger detection grids were grounded because it had been observed that titanium metal was deposited upon any ungrounded surface during this process. The time interval

from the etching of the samples to the pump start was typically 1-2 hours. The pressure in the chamber reached the 10^{-7} Torr range approximately 1/2 hour after the ion pumps had started, at which time the valve to the monochromator could be opened and optical data collected on the sample.

Optical reflectance was measured between 400 Å and 1400 Å in four wavelength intervals. For each interval the monochromator was set to the position of maximum light intensity, the incident light was allowed to impinge on the channeltron, and the monochromator slits were adjusted to obtain approximately 12K counts per second. The monochromator was then set to the shortest wavelength in the interval and stepped in increments (typically 5 Å) to the longest wavelength in the interval. For each interval, scans were made for the incident light and for the light reflected from the sample. Scans were made over the intervals 400-520 Å and 500-900 Å without a filter, 700-1100 Å through the indium filter, and 1000-1400 Å through the lithium fluoride filter. Slit widths ranged from about 3 μm near the blaze wavelength of 800 Å, to nearly 200 μm when using the indium filter.

The channeltron was operated at a potential of 3.6 kV. The rear electrode was held at 3.0 kV positive relative to ground while the cone was held at 600 volts negative to eliminate spurious signal due to photoelectric emission from the sample. Figure 10 is a block diagram of the electronic system used for reflectance measurements. The signal taken from the rear electrode of the channeltron was a current pulse which passed into a preamplifier built according to a Bendix design and mounted directly on the chamber. The pre-amp had a voltage gain of unity and merely converted the current pulse into a voltage pulse which was input for an Ortec

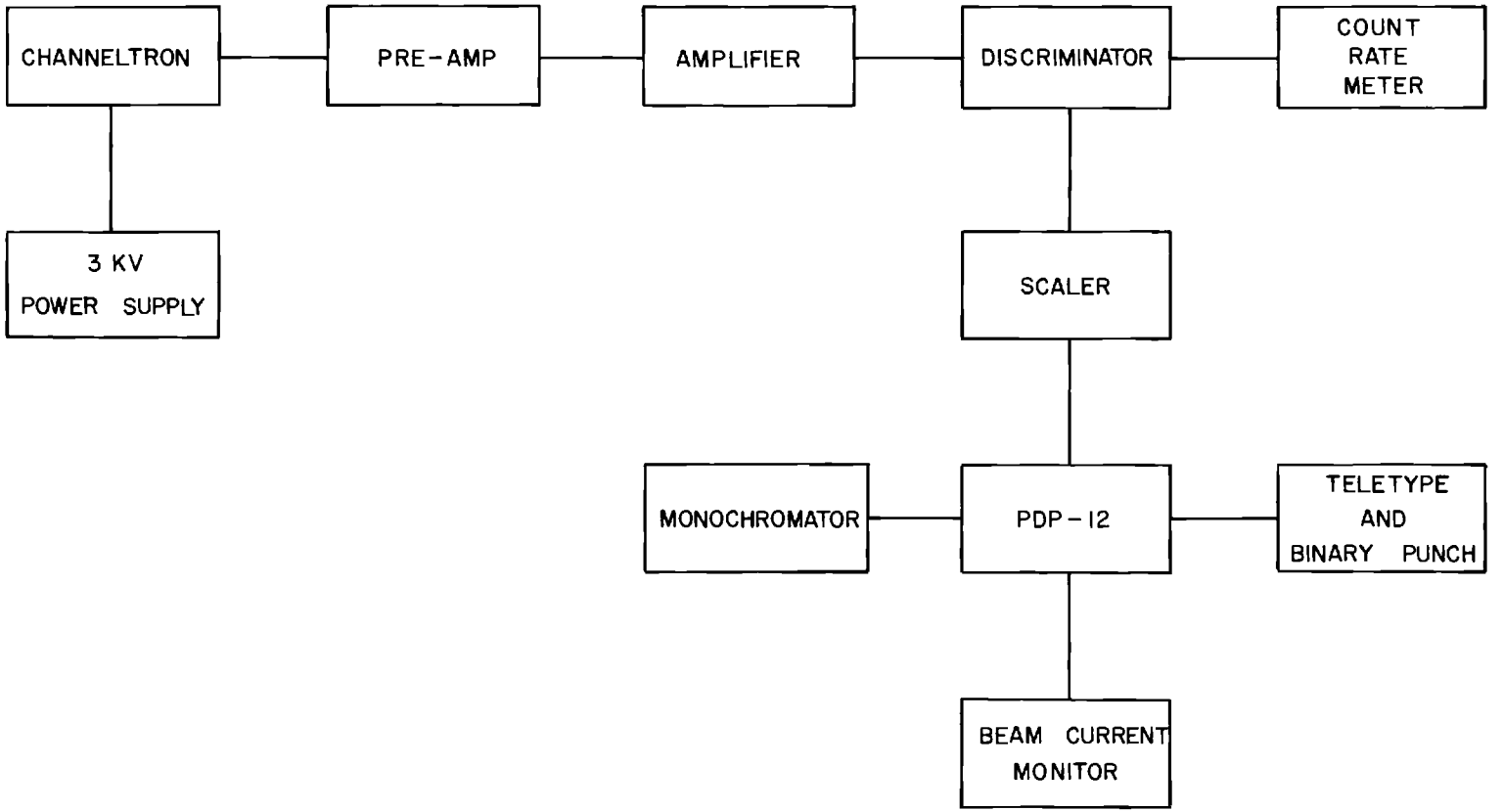

Figure 10. Electronics Used for Optical Reflection Measurements

model 485 amplifier. An Ortec model 421 pulse height discriminator was used following amplification to eliminate noise pulses from the amplifier. The discriminator produced five-volt logic pulses which were counted and accumulated by a Hewlett-Packard model 5201L scaler. An Ortec count rate meter was also used to monitor the count rate and facilitate alignment of the detector. The accumulated count total in the scaler after some set period of time was entered into the PDP-12 as data.

Although the channeltron was capable of a count rate of 10^6 counts per second, we were limited to much lower count rates by two factors. First, because we wished to compare signals of different strengths (often the reflectance of the sample was on the order of 1%), it was imperative that the pulse height distribution at the discriminator be independent of the count rate. This requirement is equivalent to demanding that the gain of the channeltron not vary with count rate, which imposes an upper limit of 20K cps. A more severe limitation was imposed by the amplifier, which was insensitive to voltage pulses of less than 40 μsec duration. Values were chosen for the components of the pre-amp to give this decay time constant to the output pulses, and the resulting "dead time" was of this same order. Comparison of signal ratios indicated that the count rate was noticeably nonlinear with signal strength for count rates greater than 15K cps. An upper limit for the count rate of 12K cps was chosen and obtained by adjusting the monochromator slits.

After accumulating counts for a chosen time interval, the count rate was "normalized" to the electron current in the storage ring by dividing the total counts by a number proportional to the electron current.

This number was obtained for all storage ring users by measuring the current produced as gas atoms ionized by the synchrotron radiation impinged upon and were collected by the clearing electrodes in the ring. This current was read across a resistance of about 12K Ω whose value was chosen so that 1.000 volts corresponded to an electron current of 10.00 milliamperes. The PDP-12 computer was designed to accept analog voltage inputs, but the relatively low input impedance made the provided voltage unsuitable as input. In our experiment a Keithley model 150B electrometer was used to monitor this voltage and produce an output voltage of 0-1.0 volt which was entered into the PDP-12 computer at one of the analog input jacks.

The PDP-12 computer controlled the experiment during a single scan (which was either I_o or I_oR) through an operating program whose basis was a modified FOCAL (28,29) language. The language, named FOCAL-0 (30,31) defined functions which allowed the experimental apparatus to be controlled by the program. One such function designated (through its argument) one of the 16 analog inputs of the PDP-12 and caused it to be read, thus obtaining a number proportional to the storage ring electron current. A second function caused voltage pulses to be emitted at a modified relay terminal of the computer. The pulses, whose number and rate were determined by values of the function's arguments, were used to step the two Responsyn motors which drove the monochromator. A third function operated one of the five relays (as designated by the argument) of the PDP-12 and caused the HP 5201L scaler to be sequentially enabled, disenabled, and the total counts read as digital input. The operating program was read into the computer from a DIAL magnetic tape, and further communica-

tion was through a teletype. The program used in our experiment required the following information which the operator entered on the keyboard: the current wavelength setting of the monochromator, the number of scans to be made, and, for each scan, (1) the time period for which the scaler was to accumulate counts, (2) the initial wavelength (in Angstroms) at which data were to be taken, (3) the wavelength increment between successive data points, (4) the wavelength of the final data point, and (5) the electron current in the storage ring which corresponded to an analog input signal of 1.00 volts. The PDP-12 proceeded to step the monochromator to the initial data point, enable the scaler for the chosen time interval as measured by an internal clock on the computer, read the scaler and ring current, and step to the next data point. The ring current was read twice, just before and just after the accumulation of channeltron counts, and an average taken. The data were printed on the teletype and punched in binary code on paper tape after each incremental wavelength step. These data consisted of the wavelength, the scaler reading, a number proportional to the ring current, and the quotient of the total scaler counts and the number proportional to ring current. Typically, counts were accumulated at each data point for 10 seconds, although in regions of very low count rates longer times were used to decrease the statistical percentage variation. About five seconds were required to move from one data point to the next. Data were normally collected at wavelength increments of 5 Å, which was somewhat greater than the resolution of the monochromator in the XUV region (about 2 Å) but which was sufficiently sensitive to detect the rather broad structure under investigation. Successive scans were

made of I_o and I_oR over the same wavelength interval. About 10 minutes were required to change the sample and detector positions.

C. Auger Characterization of Surface

Auger spectra were made on each sample, although close time proximity to the reflectance measurements was often impossible because stray magnetic fields from the storage ring magnets caused noise in the Auger signal. The electron beam was directed on the sample using the deflection plates on the gun. Although the samples did not fluoresce under electron bombardment, the surrounding stainless steel did, and this facilitated visual alignment. The electron current from the gun was typically 12 μA. The beam was focused and the angle of incidence adjusted until the fluorescent screen was fully and evenly illuminated. The sample was biased with a small voltage (normally -10 V relative to ground) to prevent space charge build-up. A more detailed description of the Auger experiment is deferred to Appendix B.

CHAPTER III

RESULTS AND ANALYSIS

Interpretation of the Reflectance Data

The recorded data in the form of binary punched paper tape as described in Chapter II were returned to Georgia Tech and entered in the Univac 1108 computer. Fortran programs were created which reduced the raw data to reflectance spectra expressed as a function of energy over the range 8.8 to 30.9 eV. A Calcomp plotter was used to generate plots of the reflectance, and of the optical and dielectric constants determined by the analysis.

The results of the reflectance measurements are shown in Figures 11-13 as a function of the incident photon energy. The reflectance exhibits a sharp fall-off up to about 11 eV where there is a change of slope which may be interpreted as a broad low peak on the shoulder of the larger decline. After about 14 eV the reflectance again decreases smoothly. The statistical fluctuations which occur in the vicinity of 12 eV are a result of the low count rate in the wavelength region 900-1040 Å where no good filter was available. The general features of our data are similar to measurements on other semiconductor materials, notably Philipp and Ehrenreich (19) and Zivitz (5).

The sharp decrease in the reflectance from the low-energy end of our data to about 11 eV is characteristic of the plasma frequency region, which is defined by

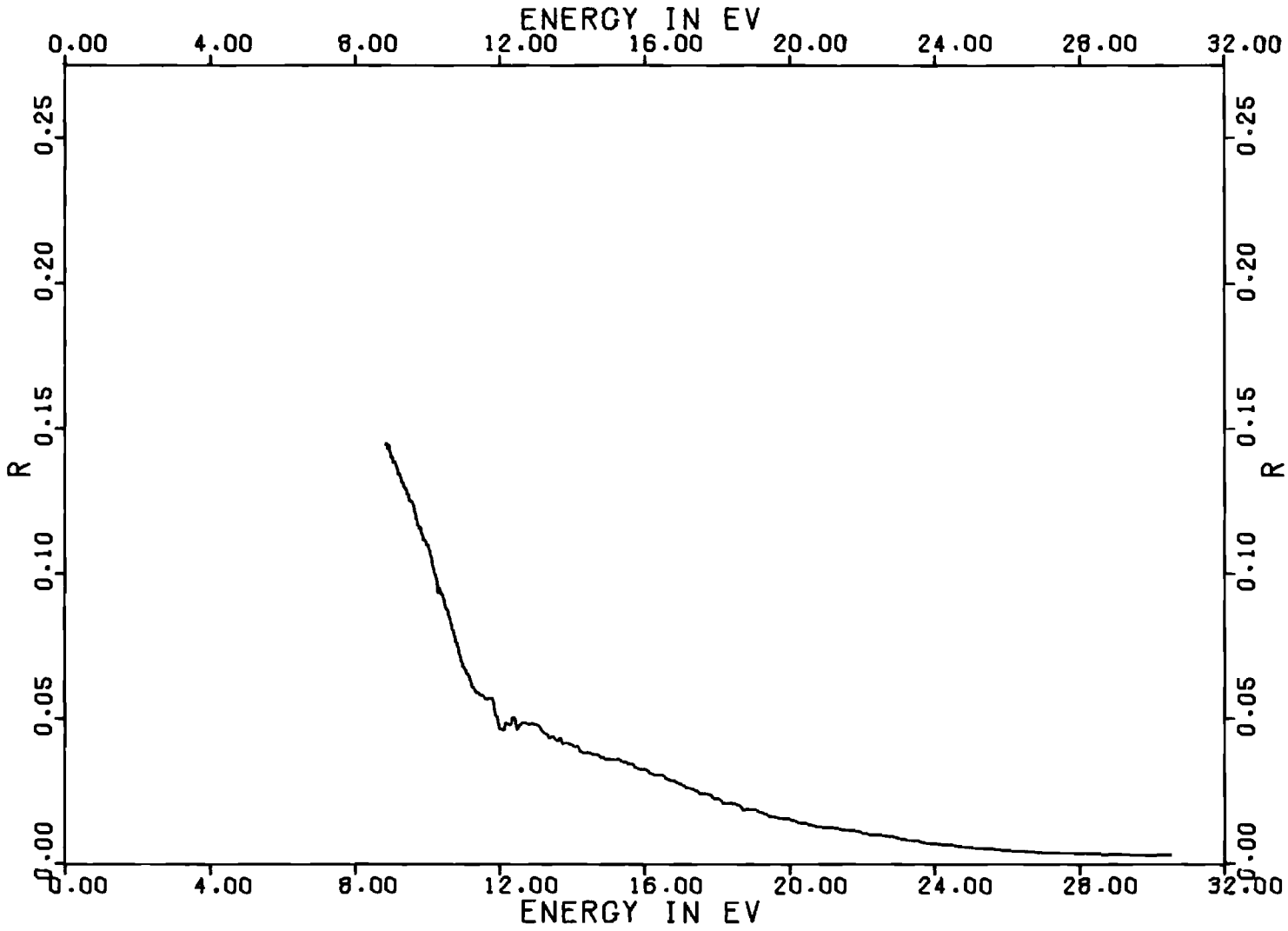

Figure 11. Reflectance of Cd_3As_2

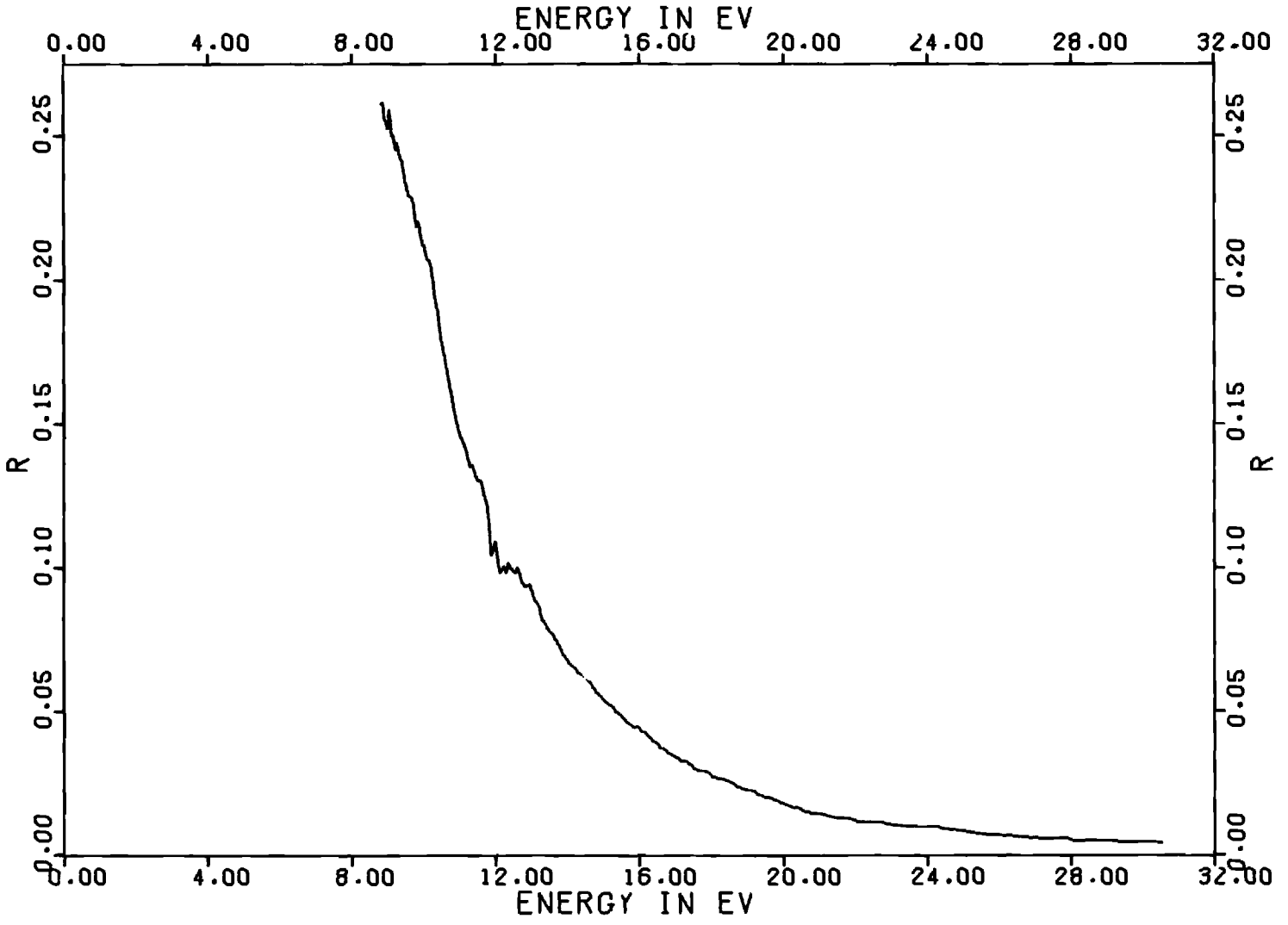

Figure 12. Reflectance of Etched $Cd_{1.5}Zn_{1.5}As_2$

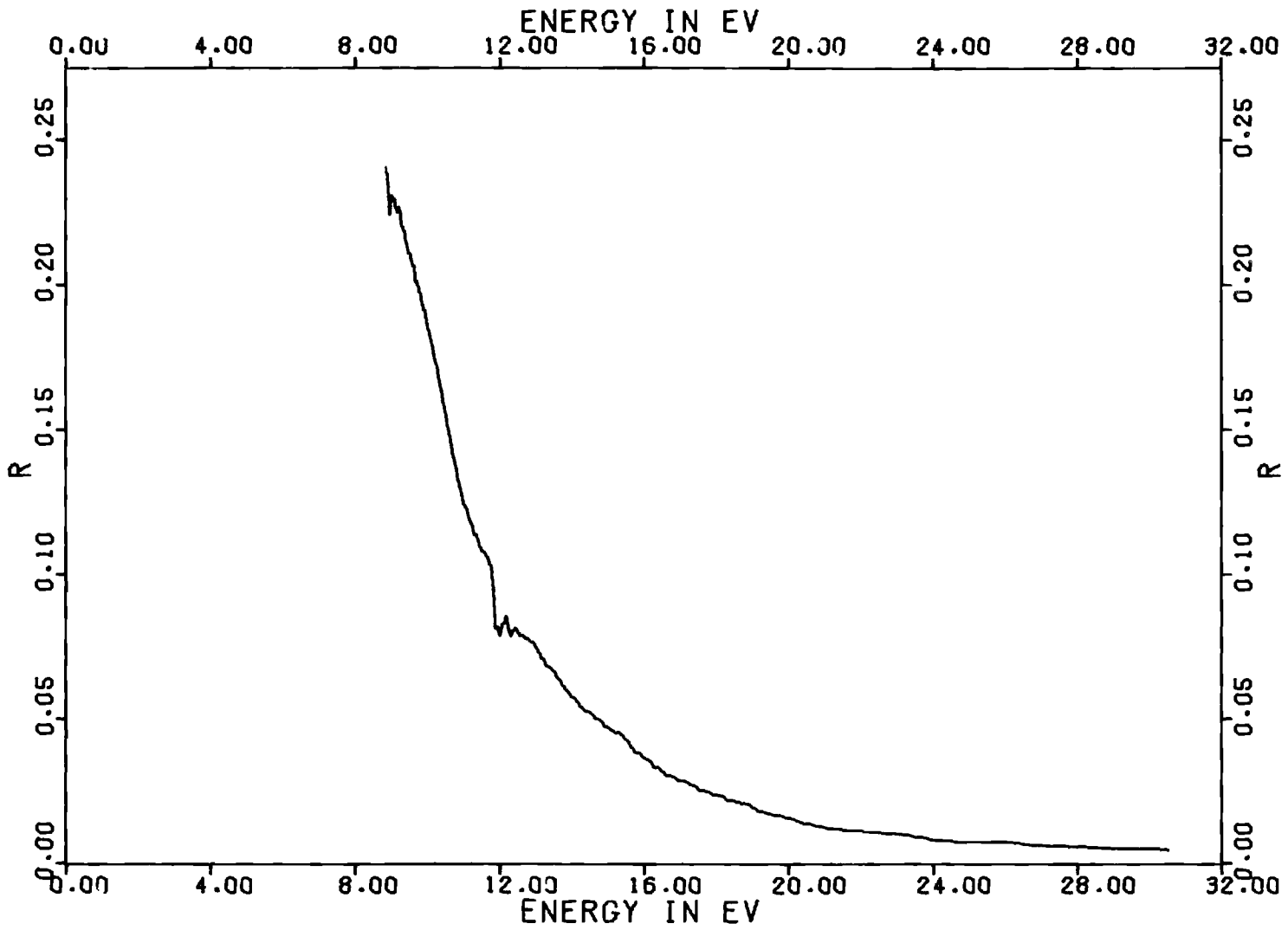

Figure 13. Reflectance of Unetched $Cd_{1.5}Zn_{1.5}As_2$

$$\omega \simeq \omega_p = \frac{4\pi ne^2}{m} \qquad (3\text{-}1)$$

where ω_p is the frequency of the infinite-wavelength collective mode for free electrons, e and m are the electron charge and mass respectively, and n is the free electron density. This is the lowest frequency for which a plasma resonance may occur and is signaled by a peak in the electron energy loss function, which Nozieres and Pines (32) have shown is the imaginary part of the reciprocal of the dielectric constant $\mathrm{Im}(1/\tilde{\epsilon})$. The plasma resonance is a longitudinal mode, so that the dielectric constant involved is actually $\epsilon_{\parallel}$, whereas optical measurements depend only upon the transverse dielectric constant $\epsilon_{\perp}$. Since Cd_3As_2 and Zn_3As_2 are non-cubic (tetragonal) materials, plasmons cannot normally be exited by optical means. Adler (33) has shown however, that in the limit of vanishing wavevector the dielectric constant is a scalar, and we have

$$\epsilon_{\parallel}(0,\omega) = \epsilon_{\perp}(0,\omega)$$

which allows a calculation of the electron energy loss in the region of the fundamental plasma resonance from optical data. To see the effect of the plasmon on the optical constants, we note that a longitudinal electromagnetic wave can exist only when the dielectric constant is zero. It is common (34,35) to define the plasma frequency as that frequency for which ϵ_1 is zero and ϵ_2 is small. The optical constants are then obtained from

$$\epsilon_1 = n^2 - k^2 \simeq 0 \qquad (3\text{-}2)$$

$$\epsilon_2 = 2nk \simeq 0$$

so that we have $n^2 \simeq k^2 \simeq 0$ at the plasma frequency.

The change in slope of the reflectance and the possible existence of a peak around 12-13 eV is attributed to the excitation of electrons in the d-bands (below the valence bands) of cadmium and zinc. To explain this interpretation it is necessary to examine more closely the electronic band structure of the material. Cadmium (Z = 48) and zinc (Z = 30) are Group II elements both possessing two electrons in an outer filled s-level lying above filled d-bands ($3d^{10}4s^2$ for Zn, $4d^{10}5s^2$ for Cd). Arsenic is a Group V non-metal whose outer electronic structure is $4s^24p^3$. In the neutral atom the d-bands of Cd and Zn lie approximately 8 eV (36,37) below the valence band of As. The evolution of the electron energy levels in the neutral free atoms into a band structure for the compounds Cd_3As_2 and Zn_3As_2 is a problem which has been treated by Lin-Chung (3), who, however, did not treat the Cd and Zn d-bands which are relatively isolated from the valence bands. We presume to associate the structure in the reflectance above 10 eV with the onset of transitions from the Cd and Zn d-bands to the conduction band since these are the only levels existing in the neutral atoms which are even remotely within reach of our photon energies. We note that this structure is poorly resolved from the plasmon structure, and that the center of gravity is impossible to locate precisely from our data.

The reflectance at photon energies above 15 eV exhibits a lack of structure which indicates the absence of further bands within the range which can be reached by photons of energies up to 30 eV. Such data are not without value, however, since they eliminate the necessity of extrapolation in this energy range when calculating the optical and dielectric constants.

Extrapolation of the Reflectance

In order to obtain values of the optical constants over the energy range of the data by Kramers-Kronig analysis of the reflectance, an extrapolation must be made to energies higher than those reached by the data. The expected behavior of the reflectance at high energies may be seen from an examination of the form of ϵ_1 and ϵ_2. If ω is sufficiently large compared to all resonant frequencies ω_{cj} corresponding to allowed interband excitations and if the damping constant γ is independent of frequency, then Equations 1-9 become

$$\epsilon_1 = 1 - \frac{\omega_p^2}{\omega^2 + \gamma^2}$$

$$\epsilon_2 = \frac{\omega_p^2 \gamma}{\omega^3 + \gamma^2 \omega}$$

Unlike most metals the damping constant, which is the reciprocal of the relaxation time, is not necessarily small in semiconductors compared to the plasma frequency; this is particularly true for transitions from deep-lying bands (20). Nevertheless for sufficiently high frequencies we arrive at

$$\epsilon_1 = 1 - \frac{\omega_p^2}{\omega^2}$$

$$\epsilon_2 = \frac{\omega_p^2 \gamma}{\omega^3}$$

from which we see that $\epsilon_2 \rightarrow 0$ rapidly and $\epsilon_1 \rightarrow 1$ more slowly. The optical constants are, then

$$n \simeq \epsilon_1 = 1 - \frac{1}{2}\frac{\omega_p^2}{\omega^2}$$

$$K \simeq 0$$

and the normal incidence reflectance is

$$R = \frac{(n-1)^2}{(n+1)^2} \simeq \frac{1}{16}\frac{\omega_p^4}{\omega^4} \qquad (3\text{-}3)$$

This assumed form of the reflectance at high energies will be useful in making the necessary extrapolation if the data extend sufficiently far that the assumptions made in deriving it are valid. Since we are essentially neglecting ω_{cj}^2 and γ^2 in comparison to ω^2, we may expect Equation 3-3 to be accurate only for energies well above the last interband transition. The value of high-energy reflectance data, even in the absence of intrinsically interesting structure at these energies, lies in the improvement of the Kramers-Kronig analysis made possible. Although an extrapolation is still necessary in order to obtain the maximum amount of information, the region where the reflectance must be guessed is energetically further removed from the structure of interest when high energy data are available.

In order to illustrate the usefulness of high-energy reflectance data, we have performed a Kramers-Kronig analysis of data taken on etched samples of Cd_3As_2. We have used the data of Zivitz (5) to 8.8 eV and then joined the high energy data of Figure 11. A multiplicative constant was used to create a smooth transition between the two sets of data; nevertheless an imperfect match in the slopes produced a false structure in the

neighborhood of 8.8 eV. Results for n, k, ϵ_1, ϵ_2, and $\mathrm{Im}(1/\tilde{\epsilon})$ were then calculated for two cases: one in which only the data below 11 eV were used, and one which made use of all the data to 30.9 eV. We did not extrapolate either set of data beyond the final point since this introduces an arbitrary manipulation which may be used to affect the results. The results are shown in Figures 14-19, in which each plot contains the results for the two cases. It may be seen that the addition of the high energy data causes major differences in the calculated results even below 10 eV; structure is enhanced, peak locations are shifted, and major differences in the absolute magnitude of the functions are introduced. The effect upon the energy loss function is the most drastic and illustrates the necessity of including at least all transitions occurring near the plasma region. The effect of nearby transitions in shifting the plasma frequency has been discussed by Phillipp and Ehrenreich (20).

The above comparison is obviously unfair since no attempt has been made to extrapolate the restricted data. In the absence of the high energy data, however, it is difficult to know when a good extrapolation has been achieved since we have no independent knowledge of the optical or dielectric constants. The most common procedure (38,39) for choosing an extrapolation for dielectrics is to assume for the reflectance beyond the highest energy data point either a power law or an exponential decay which includes an adjustable parameter, and then to adjust this value so that the phase shift calculated from KK analysis is zero for energies less than that of the first allowed transition. An obvious disadvantage of this method is that the high-energy reflectance affects the KK integral at low energies

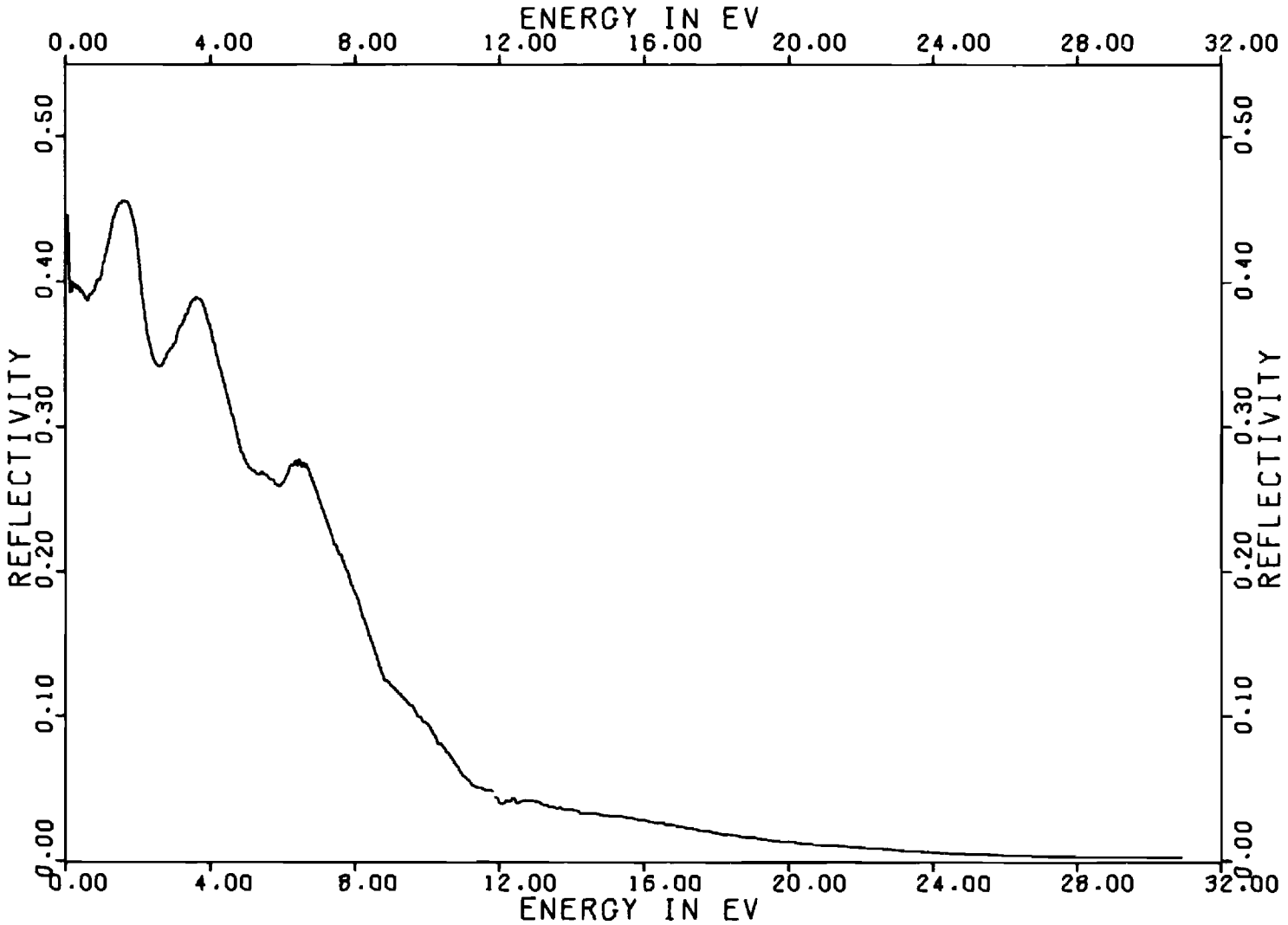

Figure 14. Reflectance Spectrum of Cd_3As_2 Obtained by Matching High and Low Energy Data

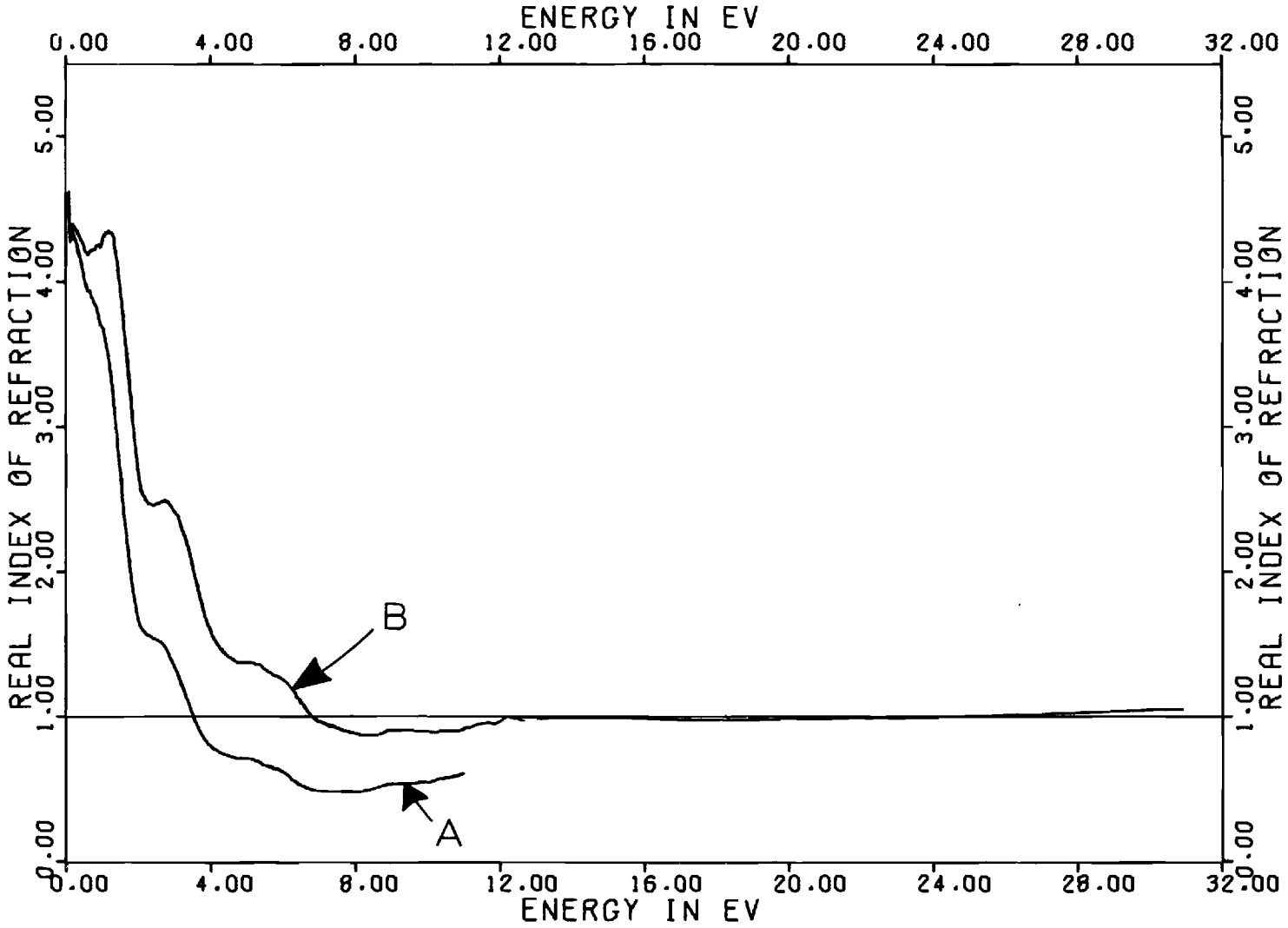

Figure 15. n Calculated by KK Analysis Using Reflection Data in Figure 14; (A) to 11 eV and (B) to 31 eV

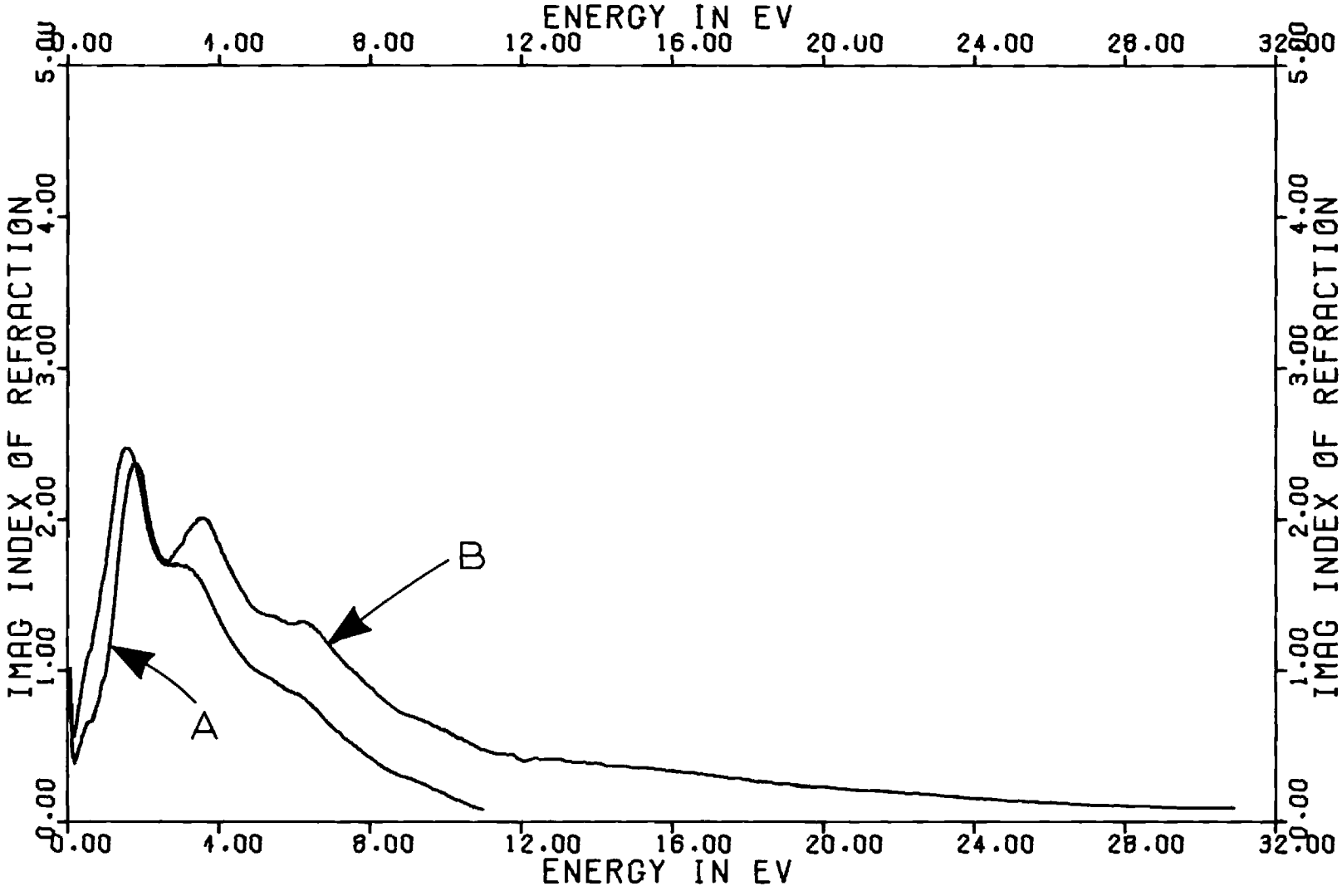

Figure 16. k Calculated by KK Analysis of Reflection Data in Figure 14; (A) to 11 eV and (B) to 31 eV

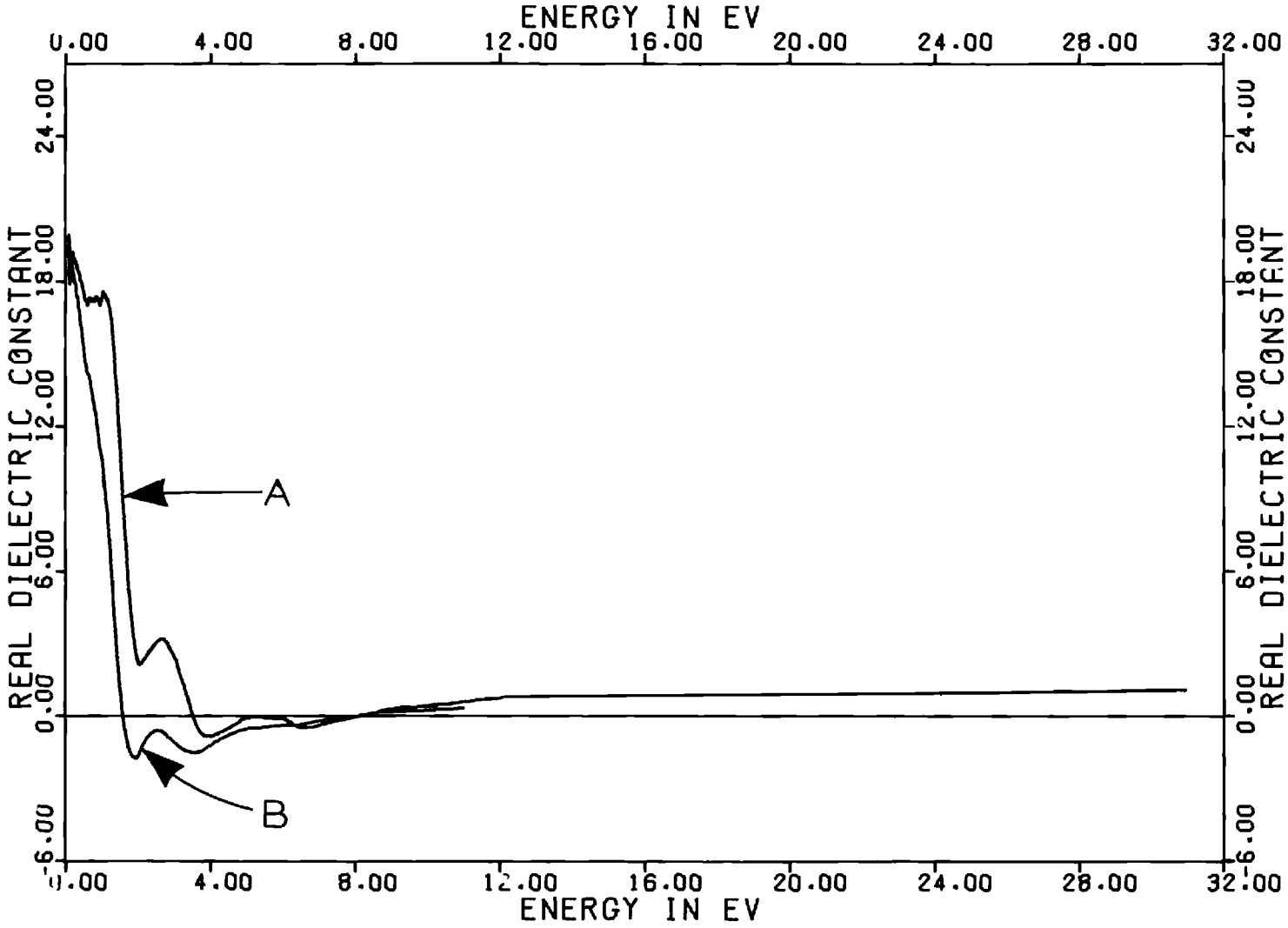

Figure 17. ϵ_1 Calculated by KK Analysis of Reflection Data in Figure 14; (A) to 11 eV and (B) to 31 eV

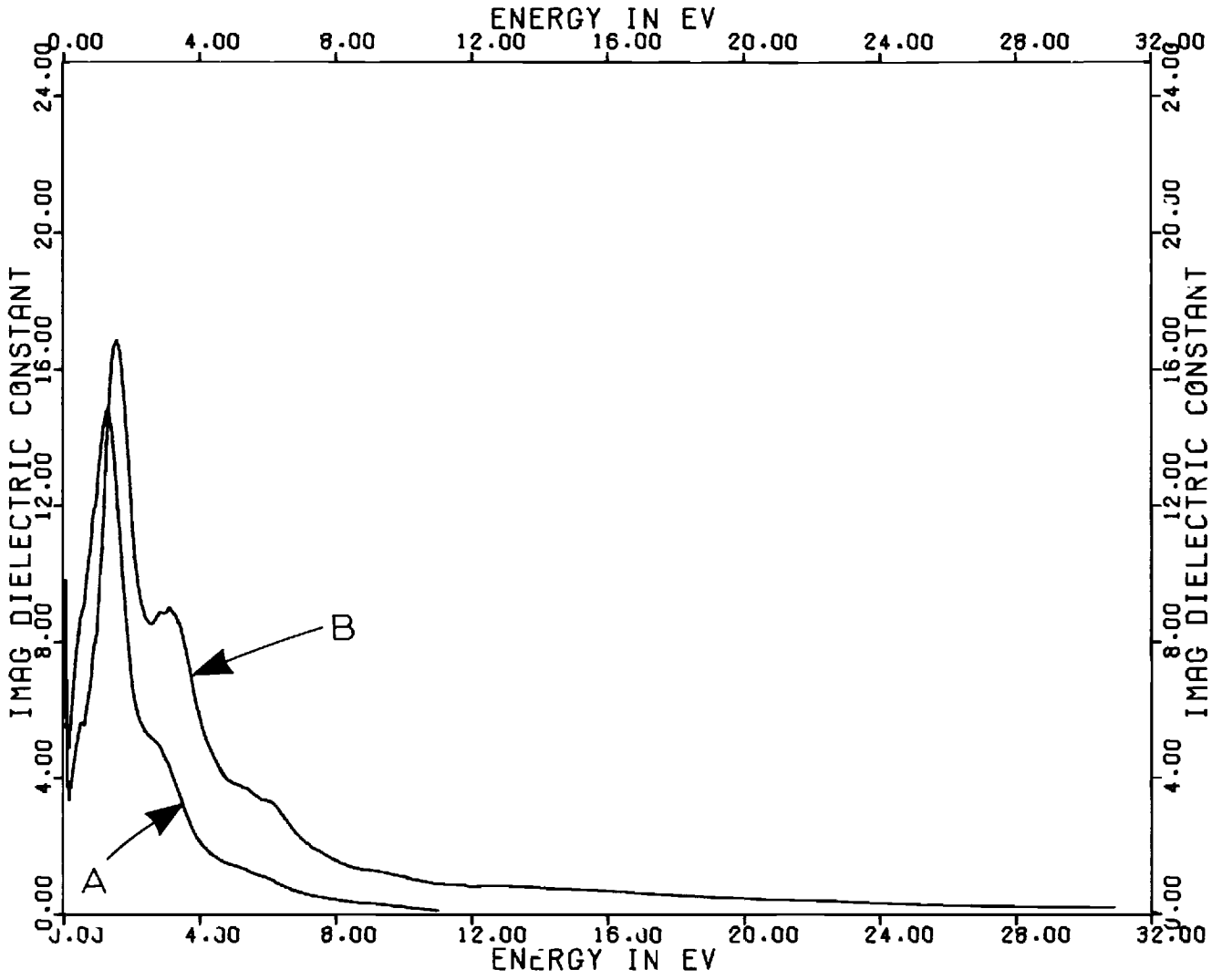

Figure 18. ϵ_2 Calculated by KK Analysis of Reflection Data in Figure 14; (A) to 11 eV and (B) to 31 eV

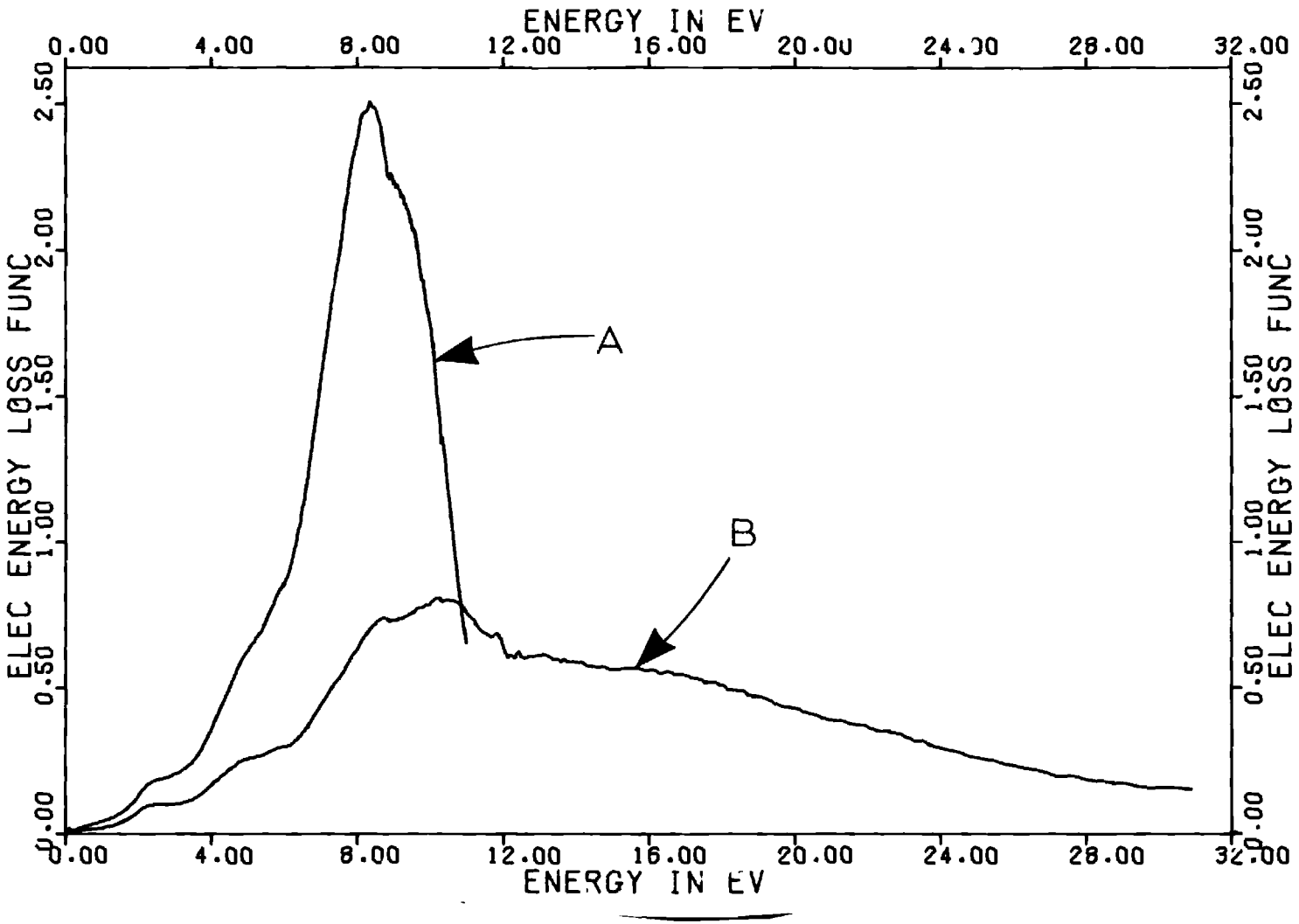

Figure 19. $\mathrm{Im}(1/\tilde{\epsilon})$ Calculated by KK Analysis of Reflection Data in Figure 14; (A) to 11 eV and (B) to 31 eV

less than anywhere else in the entire spectrum, so that this procedure does not assure accuracy for the calculated optical constants in the ultraviolet. For application to semiconductors an added disadvantage is the narrow width of the zero-phase shift region (.135 eV for Cd_3As_2, less than 1.0 eV for $Cd_xZn_{3-x}As_2$ when $x < 3$). Zivitz (5), who has used this method on semiconductors, observes that the technique is sensitive to errors in the reflectance measurements in this small energy range.

Use of Sum Rules in Extrapolation of Data

It is known that the optical constants obey certain sum rules, two of which are given in Equations 1-22 and 1-23 and rewritten here for convenience as

$$\text{SR1:} \quad \int_0^\infty (n-1)\, d\omega = 0 \tag{3-4}$$

$$\text{SR2:} \quad \int_0^\infty (n-1)\, k\omega d\omega = 0$$

It has occurred to us that these sum rules might provide a test for the optical constants calculated from a KK analysis and that a suitable choice for the extrapolation of the reflectance to high energies might be guided by demanding that the calculated n and k obey these sum rules. We wish to stress that this test of the KK termination is not a test of the accuracy of the data, since presumably inaccurate data may be extrapolated so that the sum rules are obeyed. Thus the validity of the extrapolation will depend upon the data, but over the entire energy range rather than a small interval. The contributions (especially to SR2) will be greater in

the range where structure exists in the optical constants, i.e. in the regions of interest where, presumably, the data are most accurate.

Before the sum rules can be of use as a test of the extrapolation we must establish the rate at which the integrals converge to their final value, and whether this may be correlated with the convergence of the Kramers-Kronig results to a "true" value. Our lack of an independent knowledge of the "true" optical constants for our samples plus uncertainties in the absolute magnitude of our reflectivity prevent us from using the data to establish these criteria. For these reasons a simulated experiment was designed and conducted on the computer. The model which was used allowed for a complete analytical description and could therefore establish the reliability and sensitivity of the criteria.

Classical Model Behavior

To investigate the convergence of the sum rules in Equation 3-4 for an ideal case we have considered a model in which the dispersion is characterized by a single resonant frequency. Nilsson and Munkby (40) have used similar classical models to trace errors introduced into the calculated optical constants by inaccurate reflectance data. We have programmed Equations 1-9 for ϵ_1 and ϵ_2 for our model and proceeded to calculate exactly the optical constants n and k. Our choice for the parameters ω_o, ω_p, and γ in Equations 1-9 determine the shape of the resulting reflectance, index of refraction, and dielectric constant as a function of energy. Interpreting Equations 1-9 quantum mechanically, ω_o is the energy difference between the initial and final states of the oscillators and ω_p is a measure of the volume density of oscillators. The damping constant γ is the inverse of the relaxation time τ for the excited state. In con-

venient units, we have

$$\tau(\text{sec}) = \frac{4.14 \times 10^{-15}}{\hbar\gamma(\text{eV})}$$

Choosing values of $\hbar\omega_o$ = 12.0 eV and $\hbar\omega_p$ = 10.0 eV, we display curves for the reflectance, optical and dielectric constants, and the electron energy loss function for values of $\hbar\gamma$ equal to 1.0 eV and 2.5 eV in Figures 20-25. We note that the energy loss function peaks not at the metallic plasma energy of 10 eV but near 15 eV. This shift is due to the presence of the ω_o resonance at 12.0 eV, so that the actual plasma frequency depends upon our choice of location of the resonance. Note that the location of the peak in the electron energy loss function does not depend upon the damping of the oscillator. In order to further observe the dependence of the loss function peak with the value of ω_o, we have programmed models which differ only in that $\hbar\omega_o$ = 6.0 eV, 9.0 eV, and 12.0 eV. The curves for the loss function and reflectance are shown in Figures 26 and 27.

In creating a single oscillator model we may hope to simulate real data in the range $\omega > \omega_o$ for samples in which the highest frequency absorption line at frequency ω_o is well separated from any lower frequency lines. Since this scheme was conceived for semiconductors (for which the more usual procedure is inappropriate), we choose for our oscillator model values of ω_p and ω_o which simulate our samples as well as possible. The values used for ω_p and ω_o correspond to energies of 10.0 eV and 12.0 eV, respectively. In choosing a value for the damping constant we depart from

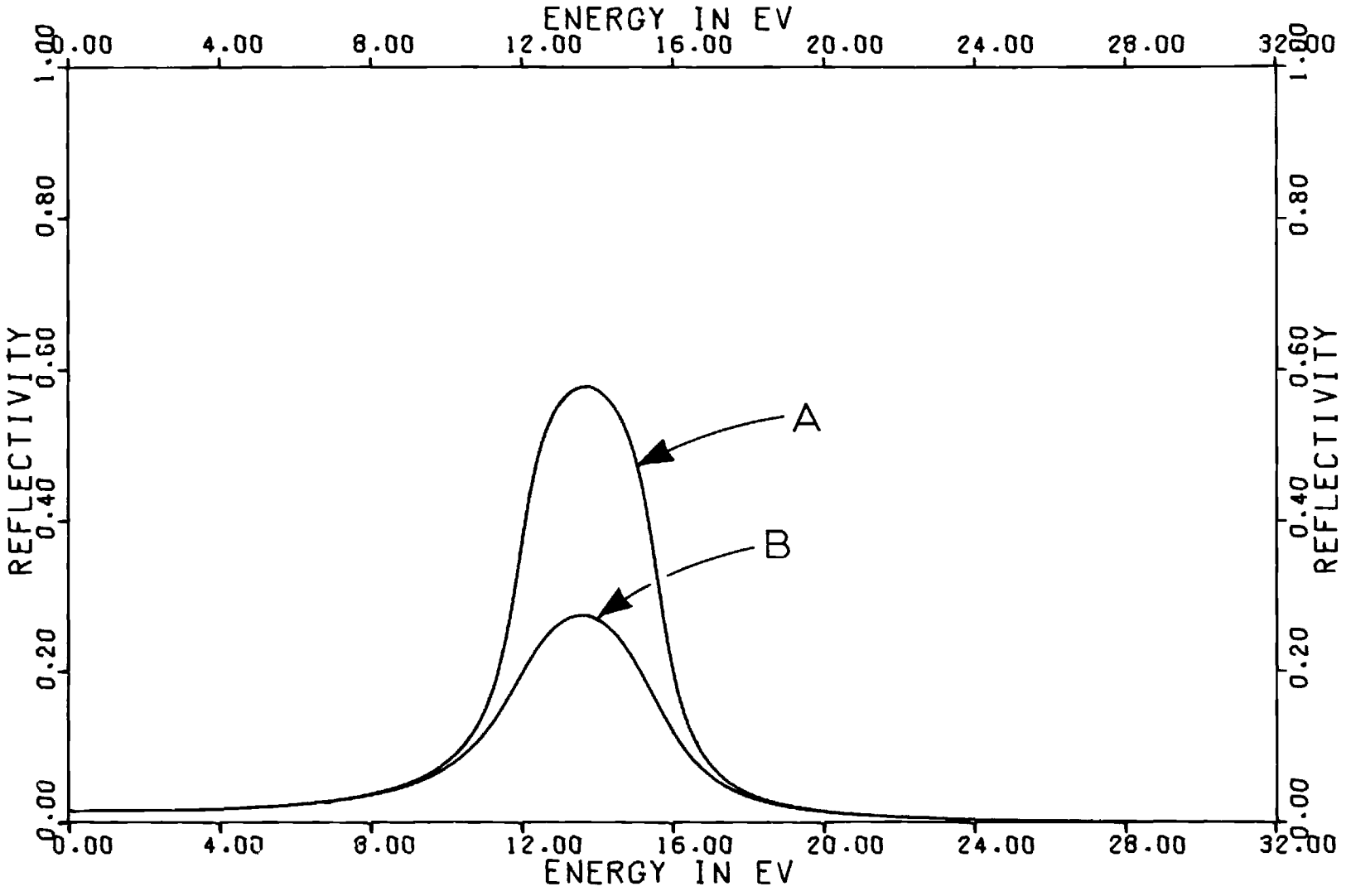

Figure 20. Theoretical Reflectance of Models for which $\hbar\omega_o$ = 12 eV, $\hbar\omega_p$ = 10 ev, and $\hbar\gamma$ Is (A) 1.0 eV and (B) 2.5 eV

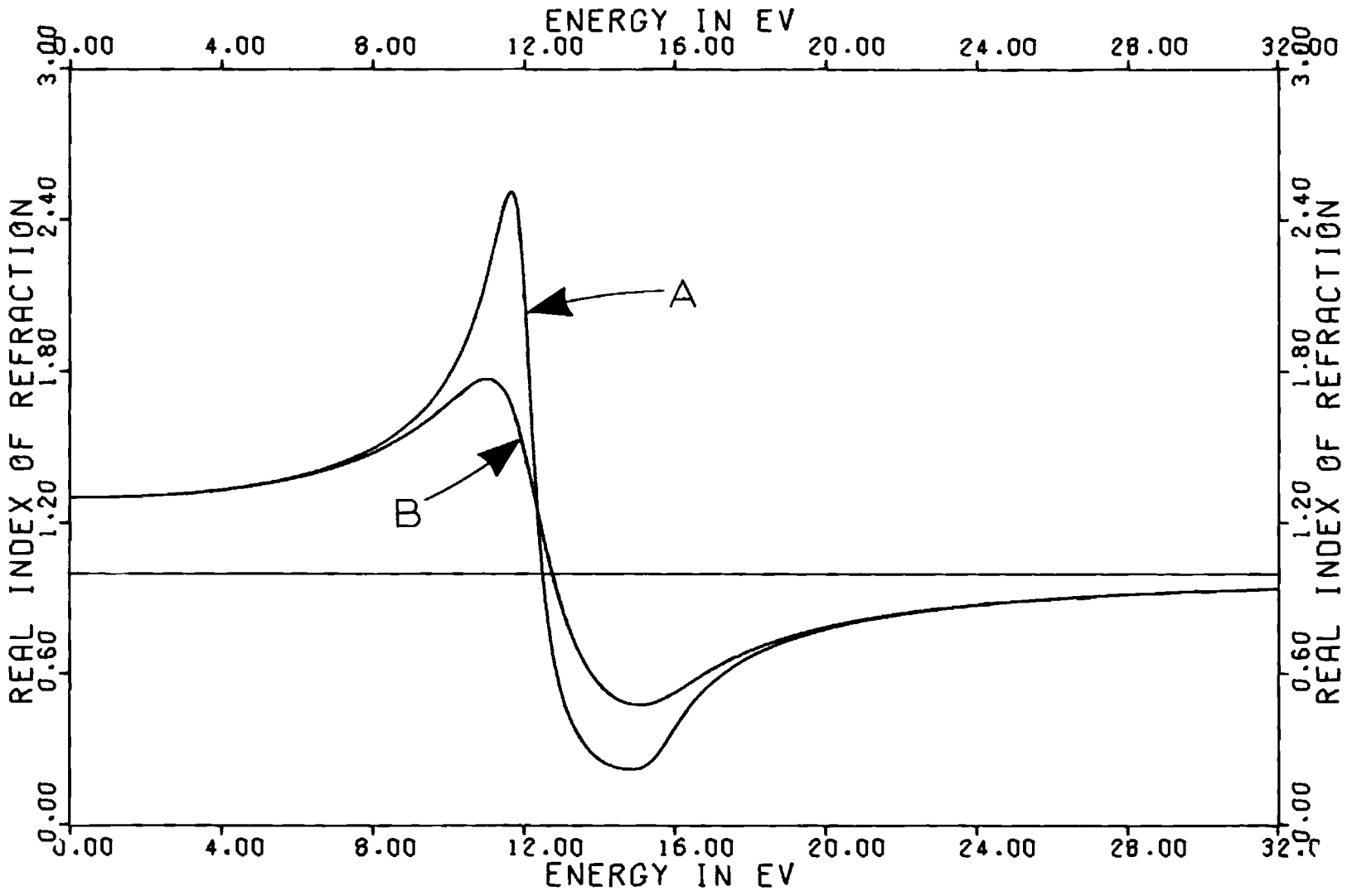

Figure 21. Theoretical n for Models for which $\hbar\omega_o$ = 12 eV, $\hbar\omega_p$ = 10 eV, and $\hbar\gamma$ Is (A) 1.0 eV and (B) 2.5 eV

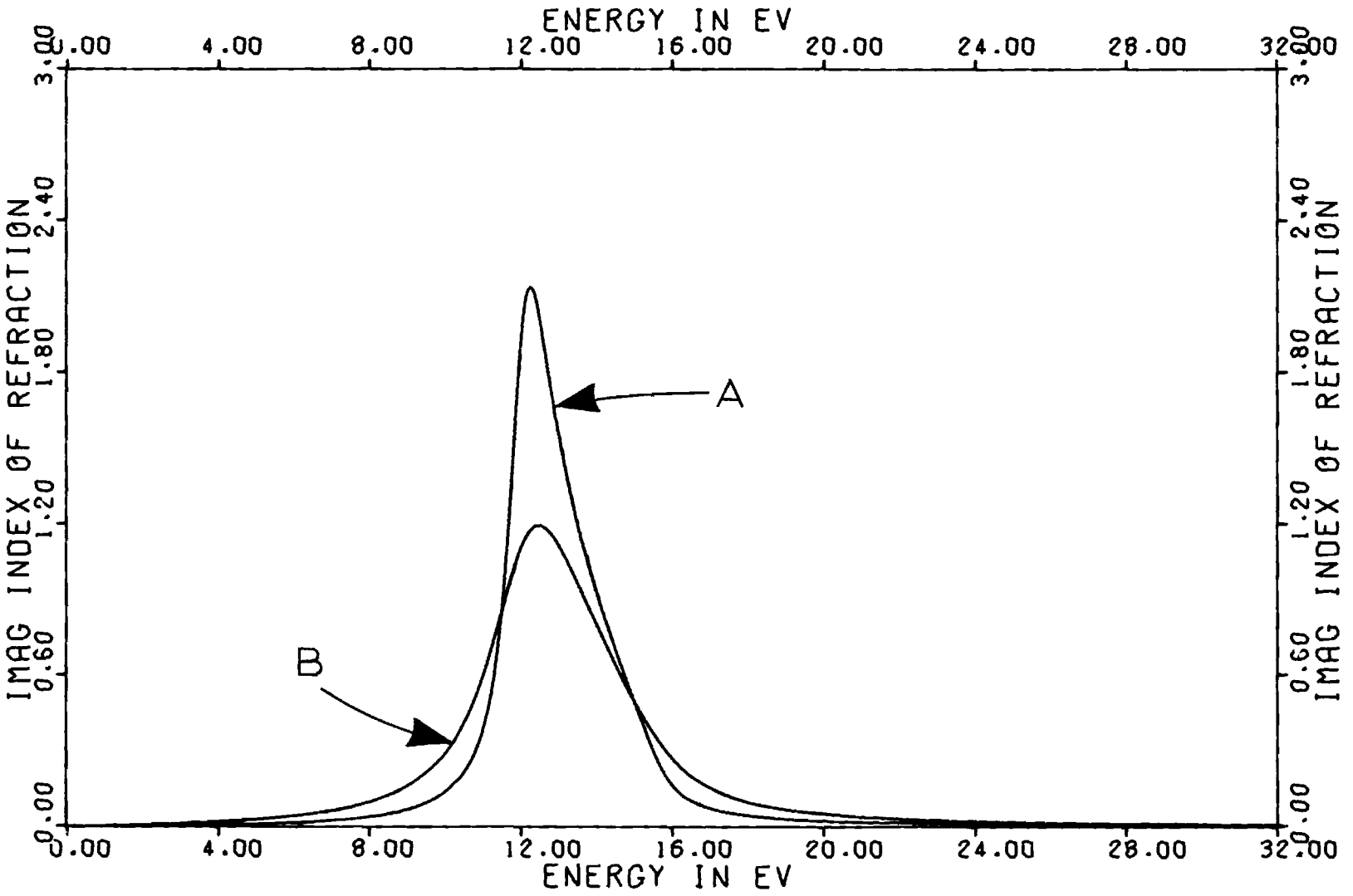

Figure 22. Theoretical k for Models for which $\hbar\omega_o$ = 12 eV, $\hbar\omega_p$ = 10 eV, and $\hbar\gamma$ Is (A) 1.0 eV and (B) 2.5 eV

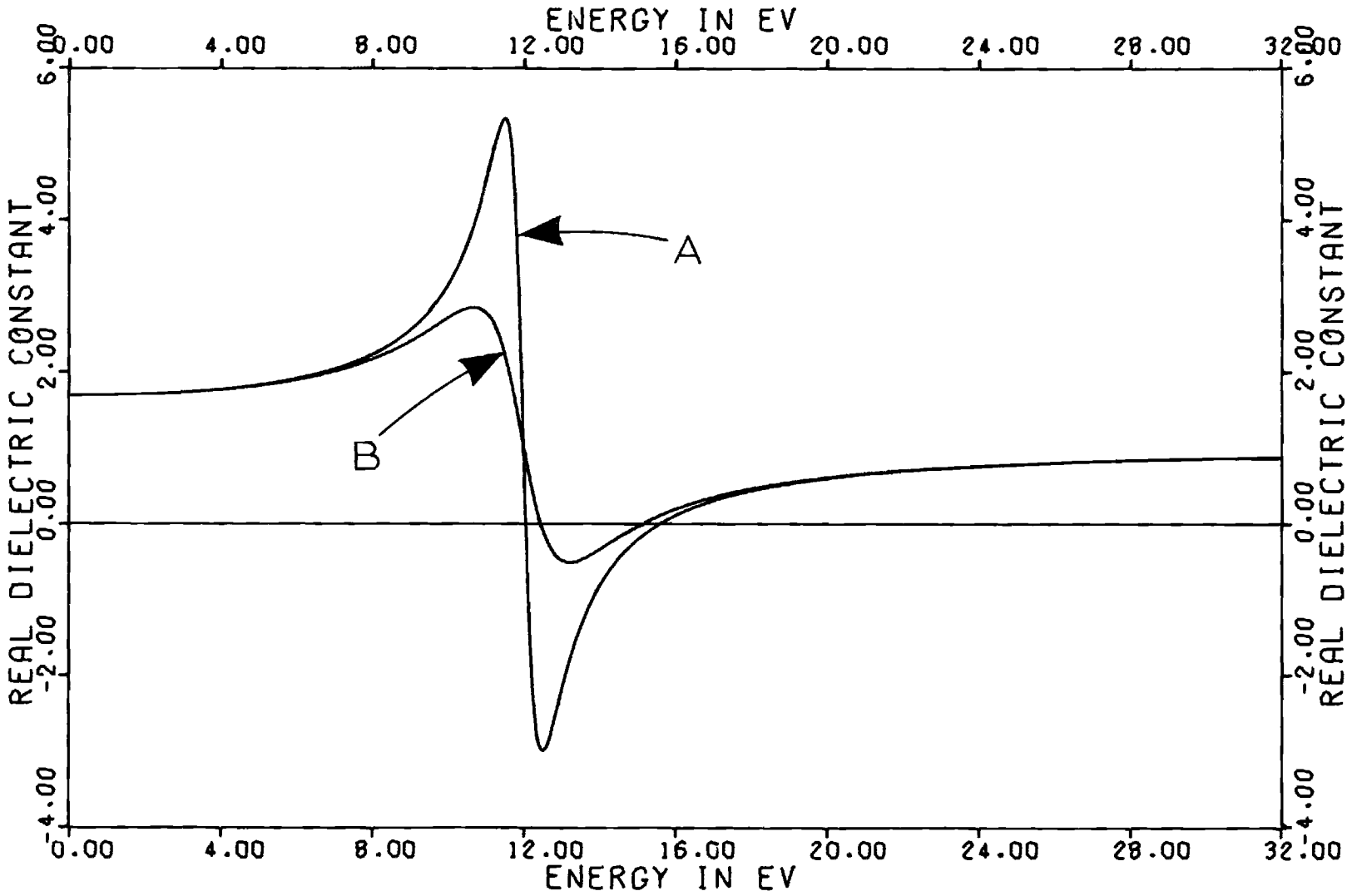

Figure 23. Theoretical ϵ_1 for Models for which $\hbar\omega_o$ = 12 eV, $\hbar\omega_p$ = 10 eV, and $\hbar\gamma$ Is (A) 1.0 eV and (B) 2.5 eV

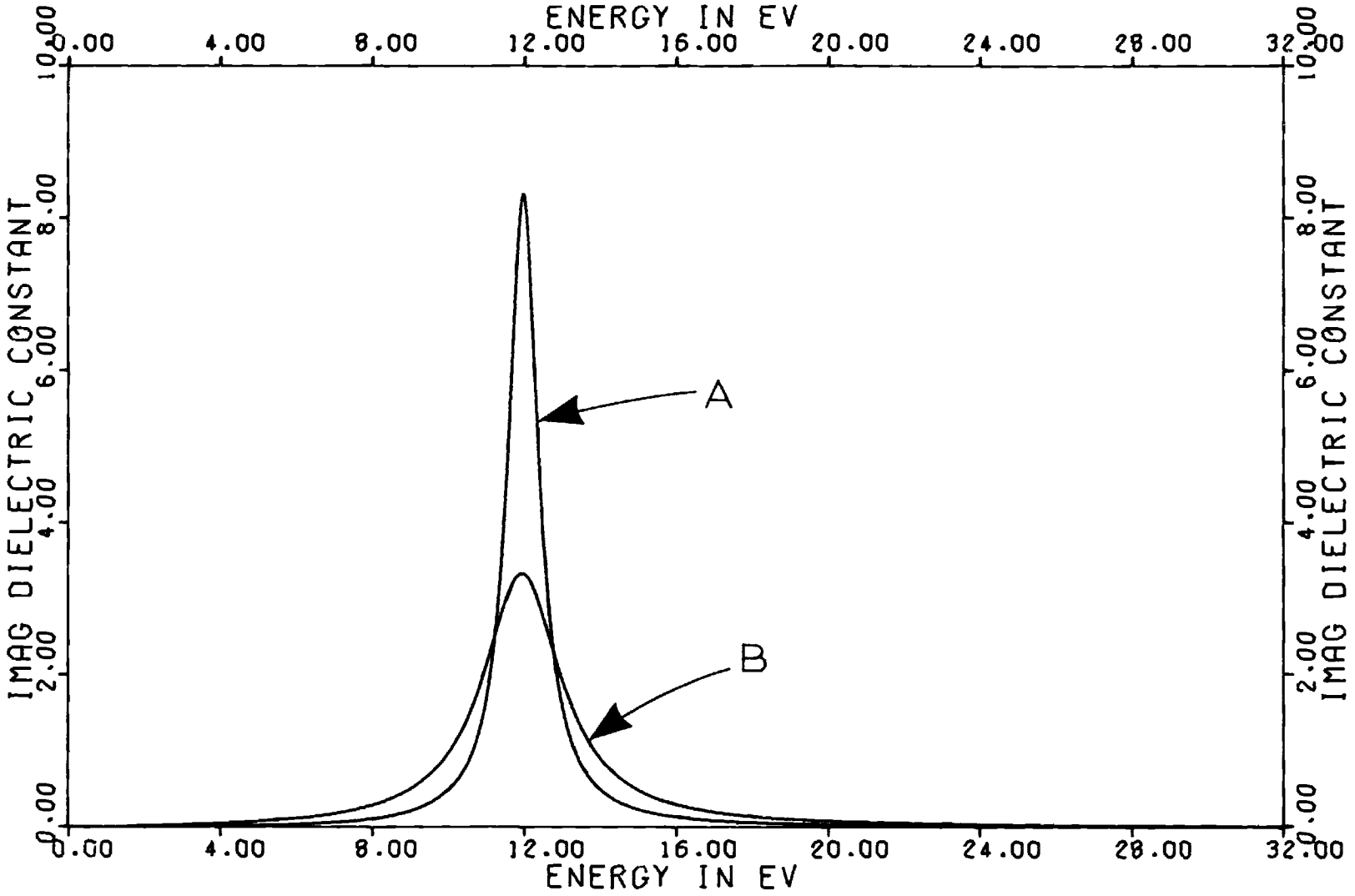

Figure 24. Theoretical ϵ_2 for Models for which $\hbar\omega_o$ = 12 eV, $\hbar\omega_p$ = 10 eV, and $\hbar\gamma$ Is (A) 1.0 eV and (B) 2.5 eV

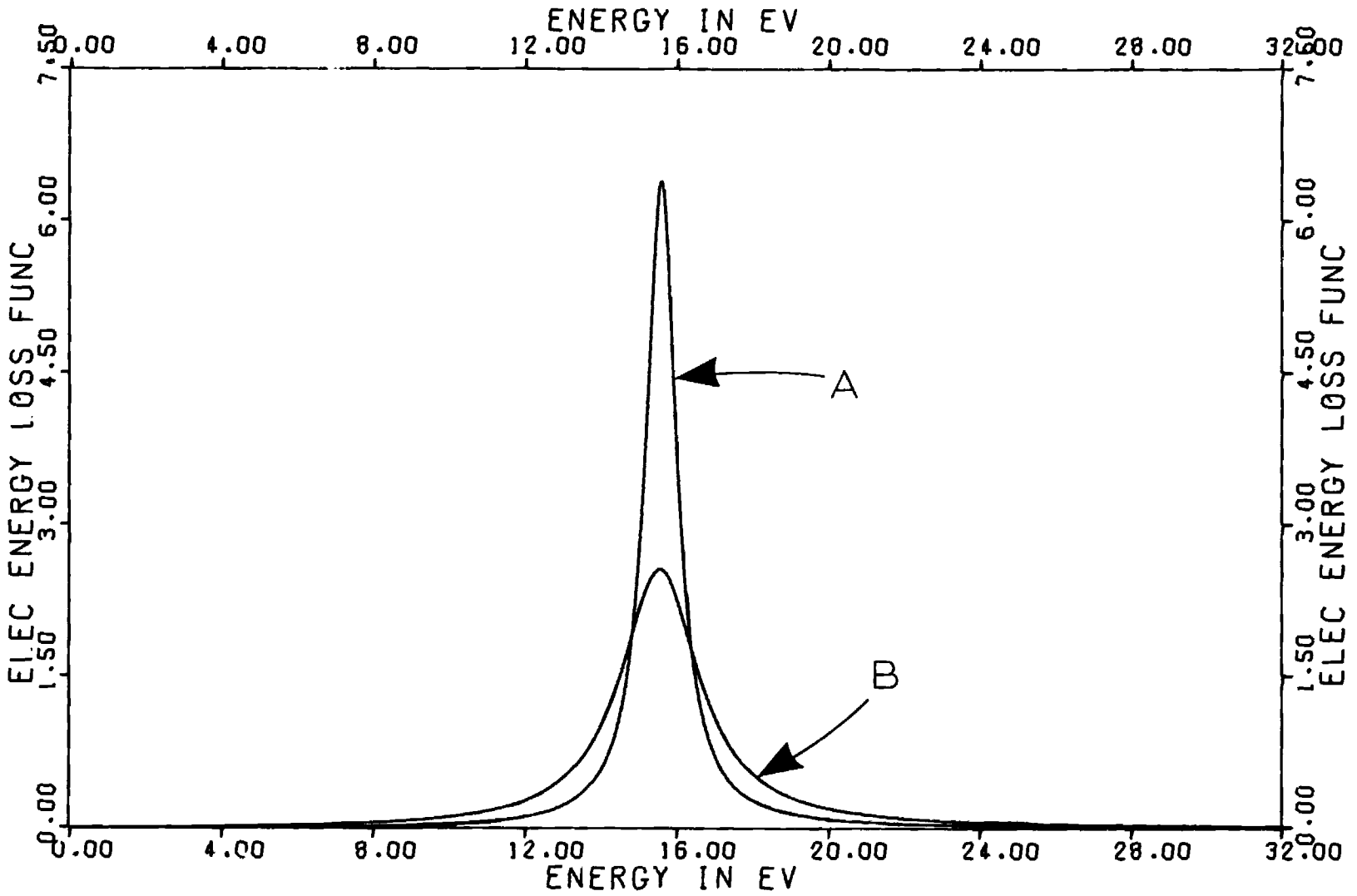

Figure 25. Theoretical $\mathrm{Im}(1/\tilde{\epsilon})$ for Models for which $\hbar\omega_o$ = 12 eV, $\hbar\omega_p$ = 10 eV, and $\hbar\gamma$ Is (A) 1.0 eV and (B) 2.5 eV

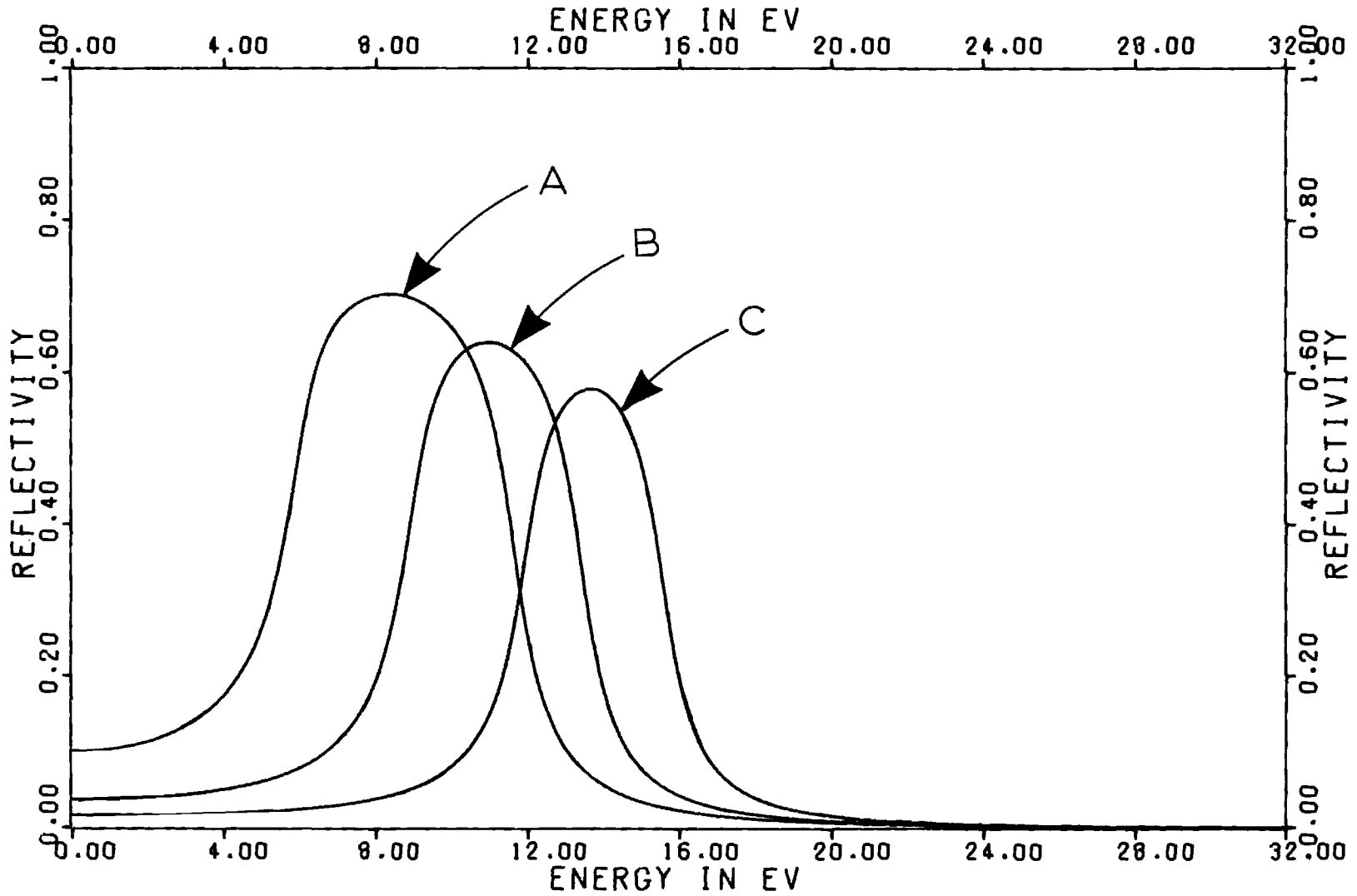

Figure 26. Theoretical Reflectance for Models for which $\hbar\omega_p$ = 10 eV, $\hbar\gamma$ = 1.0 eV, and $\hbar\omega_o$ Is (A) 6 eV, (B) 9 eV, and (C) 12 eV

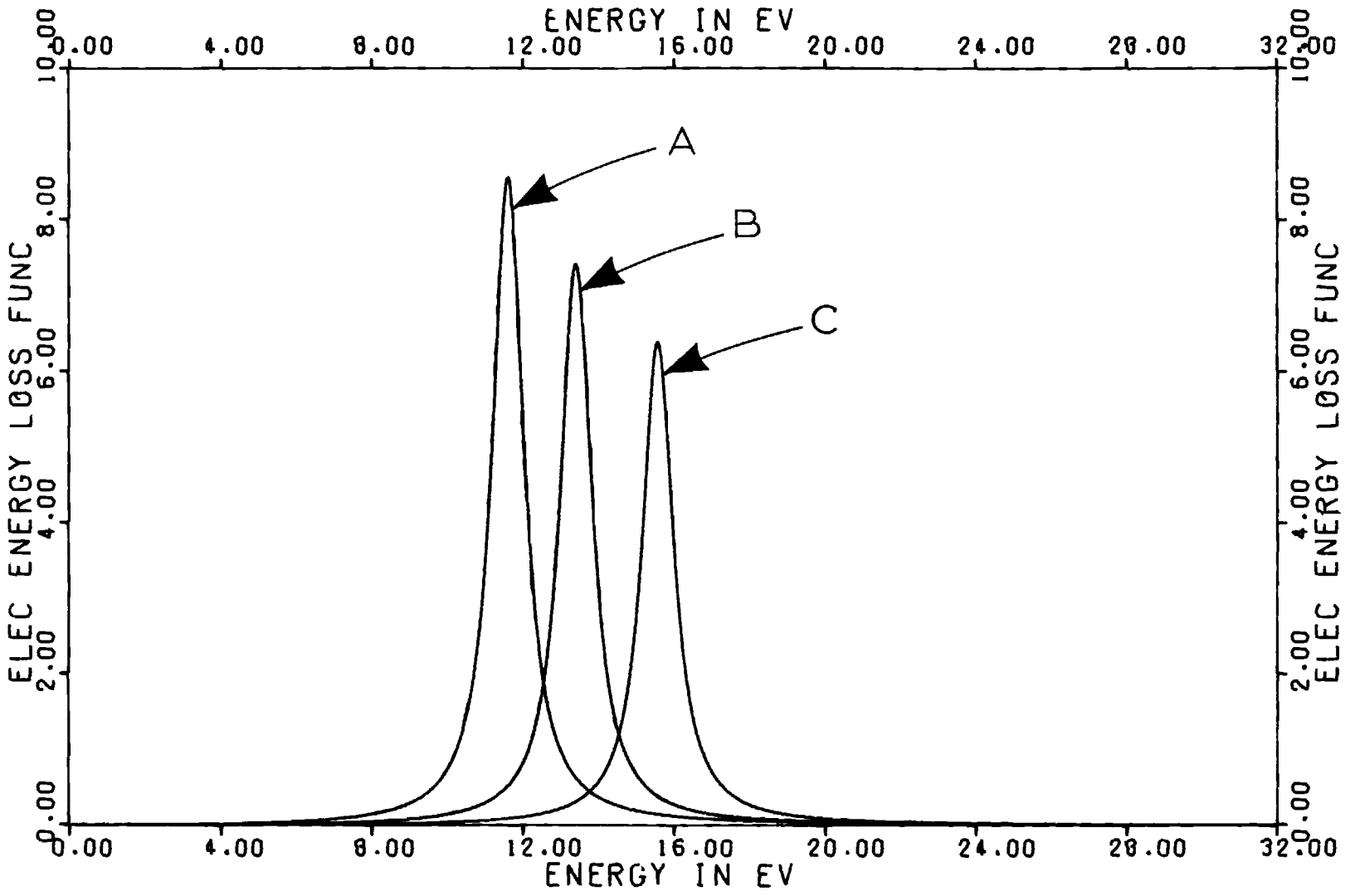

Figure 27. Theoretical $\mathrm{Im}(1/\tilde{\epsilon})$ for Models for which $\hbar\omega_p$ = 10 eV, $\hbar\gamma$ = 1.0 eV, and $\hbar\omega_o$ Is (A) 6 eV, (B) 9 eV, and (C) 12 eV

typical semiconductor values so that the magnitude of the absorption is enhanced, and we use a value $\hbar\gamma = 2.5$ eV.

We have evaluated the sum rules in Equations 3-4 for the optical constants appropriate to our model for values of the upper limit of integration Ω. The integration was done by a trapezoidal rule iterative program using values of n and k obtained from tabulations calculated for the model. Values of SR1 and SR2 are plotted as a function of Ω/ω_o in Figures 28 and 29, respectively. The convergence of SR1 is quite gradual; the value for SR1 decreases by a factor of one half as Ω changes from 9 to 18 times the resonant frequency. Conversely, the value of SR2 converges rapidly toward zero and is less than 0.02 when Ω is five times the resonant frequency. The second sum rule in Equations 3-4 thus becomes our choice for use in terminating the reflectance data.

In order to correlate the convergence of SR2 with the accuracy of a Kramers-Kronig analysis, we have calculated the normal-incidence reflectance $R(\omega)$ from the optical constants n and k of the model and performed a KK integration to regenerate the dielectric constants ϵ_1' and ϵ_2' (the prime will consistently denote the regenerated functions). This integration was done for various upper limits of integration Ω and the resulting $\tilde{\epsilon}'$ was compared with $\tilde{\epsilon}$ as a function of Ω/ω_o. In addition, the sum rule SR2 was calculated from the regenerated optical constants n' and k'. Since in comparing $\tilde{\epsilon}(\omega)$ and $\tilde{\epsilon}'(\omega)$ we have two functions whose agreement will depend upon the value of the argument ω and since, however, we are most interested in the optical properties near the resonance, we will resist the temptation to display large numbers of plots. Instead we arbitrarily choose to compare the location and the height of the maximum oc-

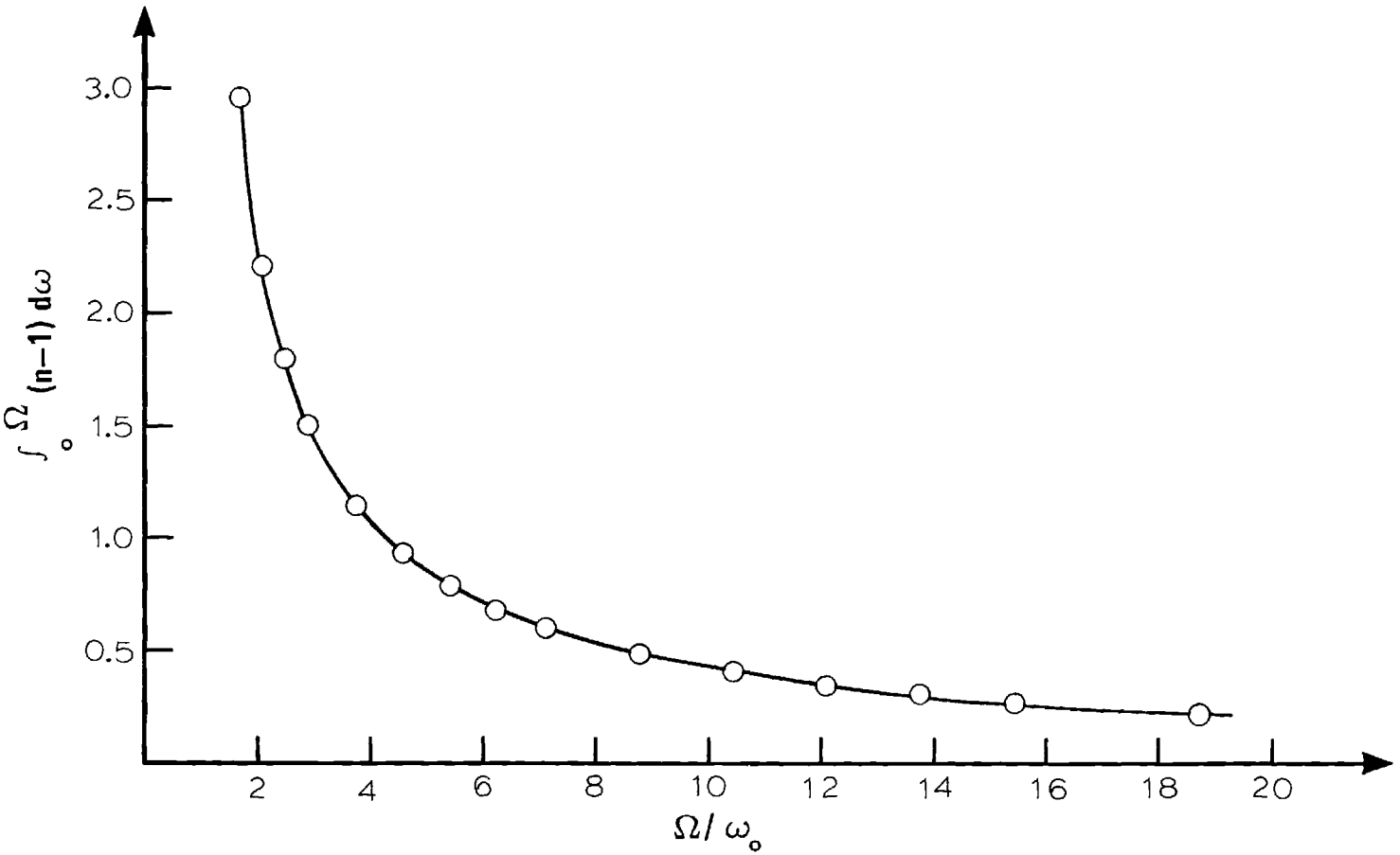

Figure 28. Value of SR1 as a Function of the Upper Limit of Integration Ω for Analytical Model

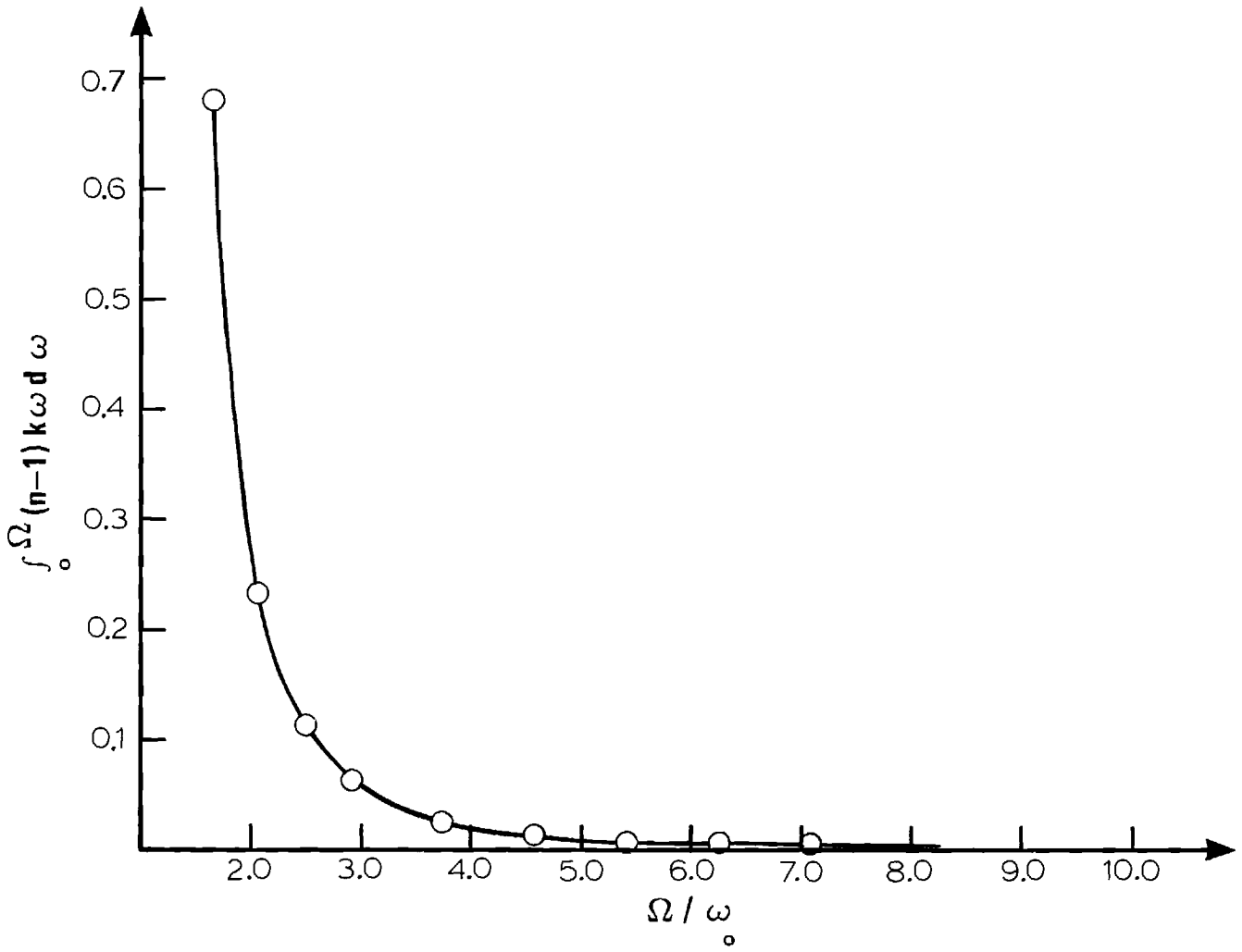

Figure 29. Value of SR2 as a Function of the Upper Limit of Integration Ω for Analytical Model

curring near the resonant frequency in the imaginary part of the dielectric constant. In Figure 30 we plot the location of the maximum point in ϵ_2' as calculated from a KK integration to an upper limit Ω, together with the sum rule evaluated for n' and k' to an upper limit Ω. The abcissa is the ratio of Ω to the resonant frequency ω_o. Figure 31 shows a similar plot of the value of ϵ_2' at the maximum. The convergence of the sum rule to zero is seen to agree roughly with the convergence of the peak location and value of ϵ_2' with that of ϵ_2. We note that a choice of $2\omega_o$ for the upper limit of integration results in an error of about 15% for the peak height and of about 0.25 eV (or 2%) in the peak location, while the sum rule has a corresponding value of 0.81. For an upper limit of above $5\omega_o$, however, the errors are less than 2% for the height and 0.014 eV (or $< 0.1\%$) for the location, respectively, while the sum rule evaluates to less than 0.02.

To establish the dependency of the convergence discussed above on the damping constant γ, we have performed brief calculations for models in which $\hbar\gamma$ was taken to be 1.0 eV and 5.0 eV in addition to the model above in which $\hbar\gamma$ was 2.5 eV. The models were otherwise identical. The results are summarized in Table 1 in which is given the percentage errors of the peak location and height in ϵ_2' together with the value of SR2 as a function of Ω/ω_o. The interpretation of the data is that a weaker damping results in more rapid convergence of the peak location but a less rapid convergence of the peak height value (which is larger in magnitude than that of a more strongly damped oscillator) and that the converse is true for strong damping. Regardless of the damping, however, the relative error in the peak location is smaller than that in the peak height and in

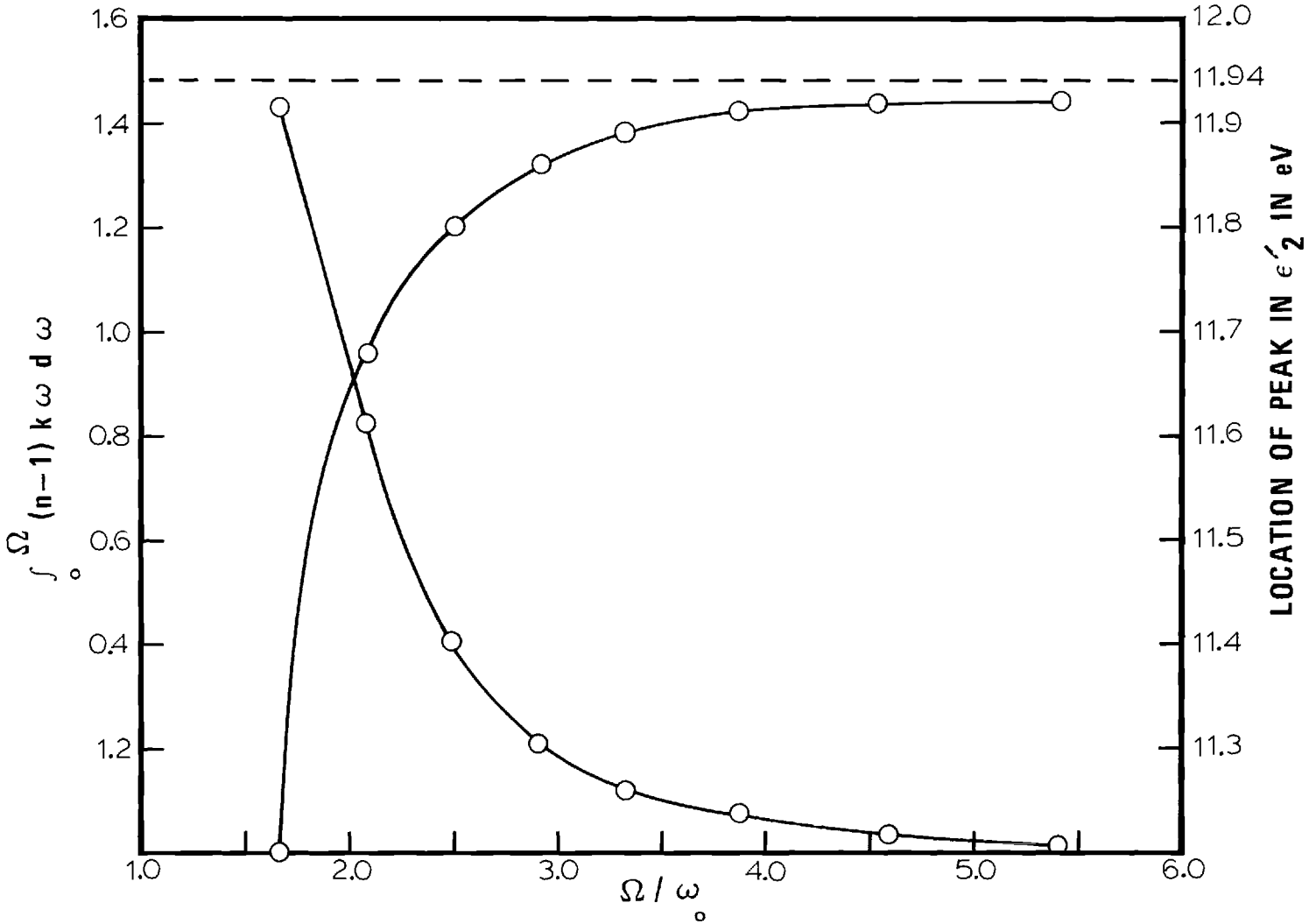

Figure 30. The Ascending Curve Shows the Location of the Peak in ϵ_2'. The Descending Curve Shows the Value of $\int_o^{\Omega} (n-1)k\omega d\omega$

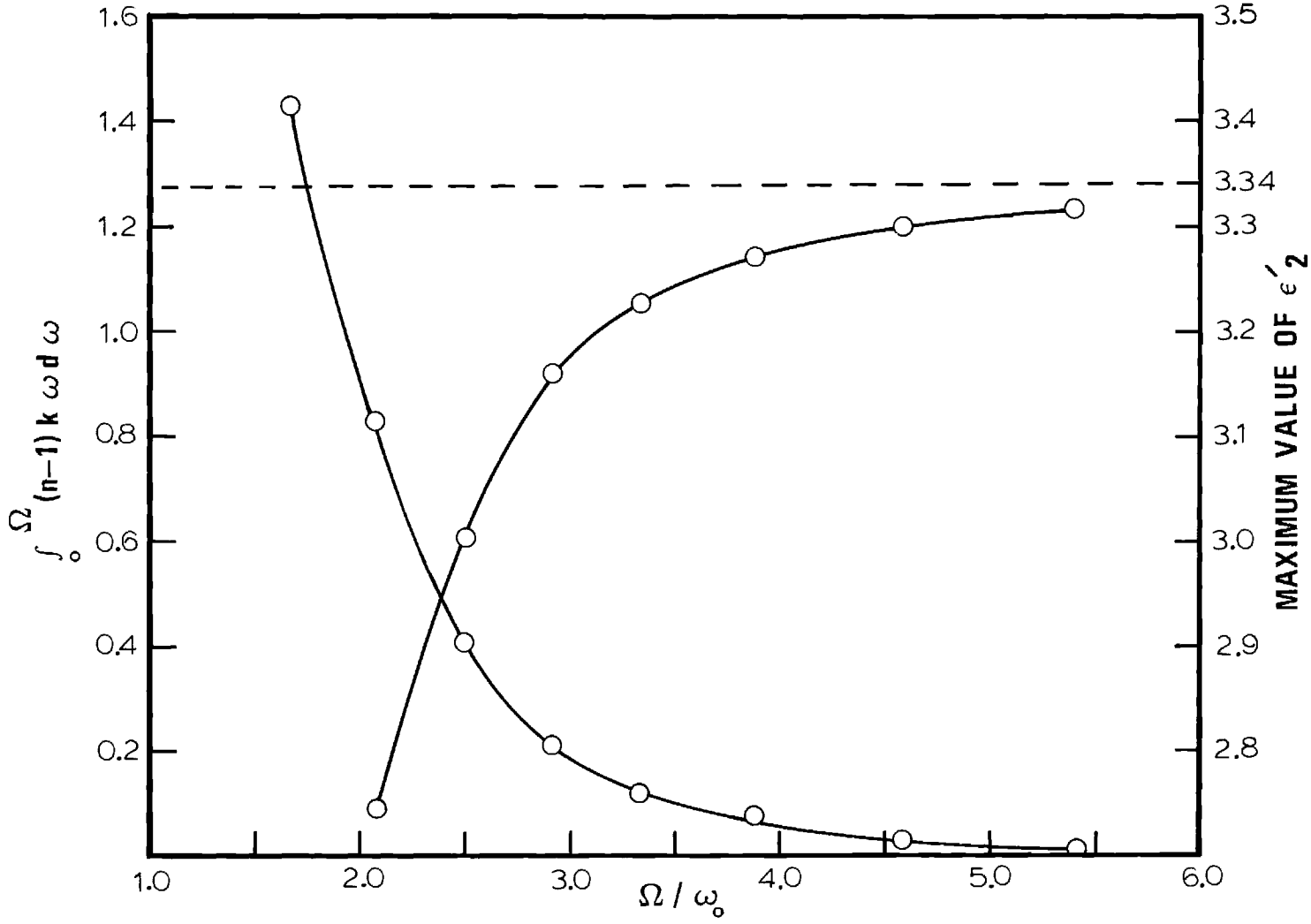

Figure 31. The Convergence of the Maximum Value of ϵ'_2 to Its Final Value Is Shown in the Ascending Curve as a Function of Ω/ω_o. The Descending Curve Is the Value of $\int_0^{\Omega} (n-1)k\omega d\omega$

Table 1. The Convergence of the Location and Height of $\epsilon_2'(\max)$ as a Function of Ω/ω_o for Various Damping Constants

$\hbar\gamma$(eV)		Ω/ω_o			
		2.1	2.5	3.3	4.6
5.0	Error in	3.2	1.5	0.7	0.2
2.5	Peak	2.0	1.2	0.4	0.1
1.0	Location (%)	1.0	0.7	0.1	< 0.1
5.0	Error in	8.9	4.4	1.7	0.6
2.5	Peak	18	9.4	3.4	1.2
1.0	Height Value (%)	41	19	6.4	1.6
5.0	Value	.614	.266	.021	.013
2.5	of	.825	.403	.115	.029
1.0	$\left\lvert\int_o^\Omega (n-1)k\omega d\omega\right\rvert$	.901	.497	.142	.031

each case the convergence of the sum rule roughly corresponds to that of the peak height. We note that, for a fixed value of Ω/ω_o, the error in the sum rule and in the maximum value of ϵ_2' is less for the more strongly damped oscillator. It is obvious from our calculations that accuracy in the absolute magnitude of the structure in the dielectric constant generated from a KK analysis of reflection data is much more sensitive to the termination at high energies than is the location of the structure. Finally, we see that values of SR2 of about 0.02 or less seem to indicate an error in the peak height on the order of 1%, with a smaller relative error in the peak location.

Application to Extrapolation of Real Data

The study of the sum rule convergence and the accuracy of a Kramers-Kronig analysis is particularly suited to the form of extrapolation in which the adjustable parameter is taken to be the upper limit of integration. One commonly used functional form for the extrapolated reflectance beyond the last data point is (5,38)

$$R = R_1 \exp[-\beta(\omega-\omega_1)] \qquad (3\text{-}5)$$

where R_1 is the reflectance at the highest frequency at which data are taken, ω_1, and β is to be chosen. The choice of β is not arbitrary, however, since we do not wish an abrupt change of slope at the frequency ω_1. Since this functional form is non-integrable to infinite frequencies, an upper limit must be taken, which then becomes the adjustable parameter.

We have extrapolated our experimental data for Cd_3As_2 using an exponential form for the reflectance beyond the highest energy data point.

A value of -0.04 for the exponential decay constant was found by matching the slope of the extrapolated reflectance to the data at 30 eV. Using the results of the study of the theoretical model, the integration was carried out to 124.5 eV, which resulted in a value of

$$\left| \int_{o}^{124.5} (n'-1)k'EdE \right| < 0.02$$

We have plotted in Figures 32-36 the results of the KK analysis of the extrapolated data together with those of the unextrapolated data. The effect of the extrapolation is apparent even at low energies, e.g. the real part of the index of refraction is driven further below unity in the region of 6 eV and remains less than one. The positions of peaks in the imaginary part of the index show slight shifts, and the value of the energy loss function in the plasma region is enhanced.

Errors in the Reflectance

Distinct in origin from the error originating in the Kramers-Kronig integral used to extract the optical constants from an experimental reflectance curve are errors in the reflectance. Sources of experimental errors in our research are enumerated below and an attempt is made to estimate the magnitude of the error.

Statistical Error

One obvious source of error was the statistical error in the accumulated count total. Since we could not allow the gain of the channeltron to change (see Chapter II), we were limited to count rates below 15K counts per second. The intensity of the reflected signal was then often on the

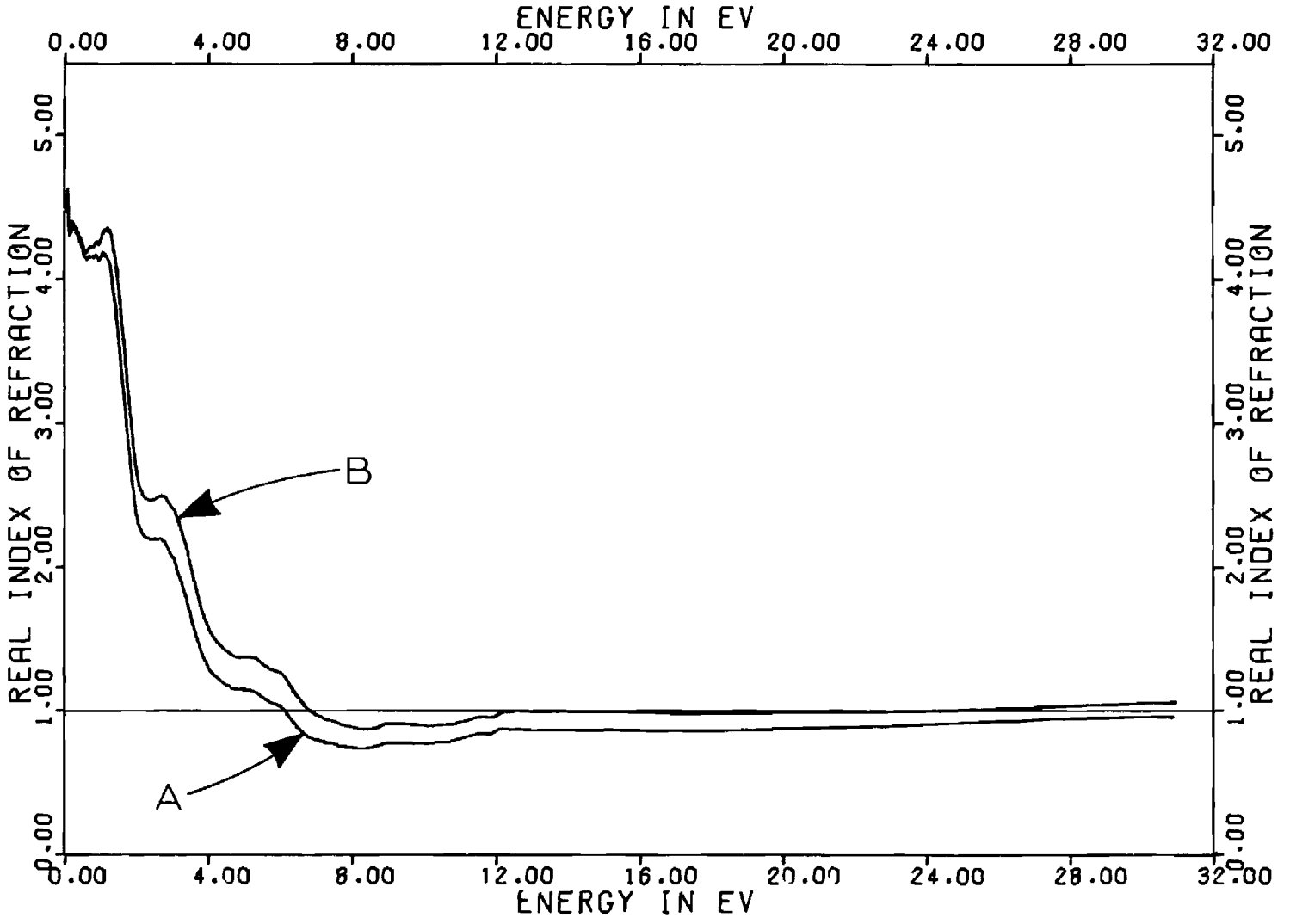

Figure 32. n Calculated by KK Analysis of Reflection Data in Figure 14; (A) With Extrapolation and (B) Without Extrapolation

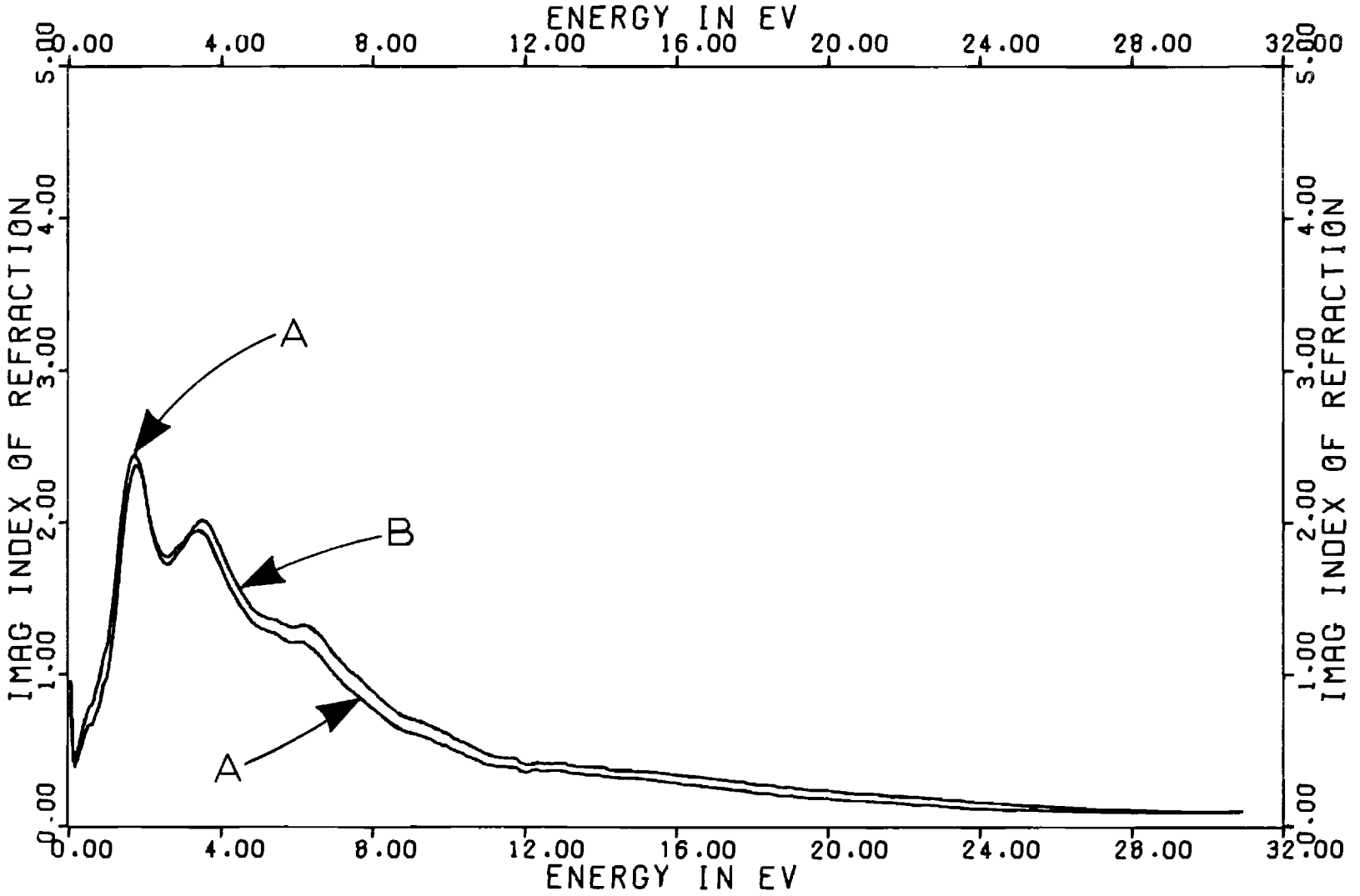

Figure 33. k Calculated by KK Analysis of Reflection Data in Figure 14; (A) With Extrapolation and (B) Without Extrapolation

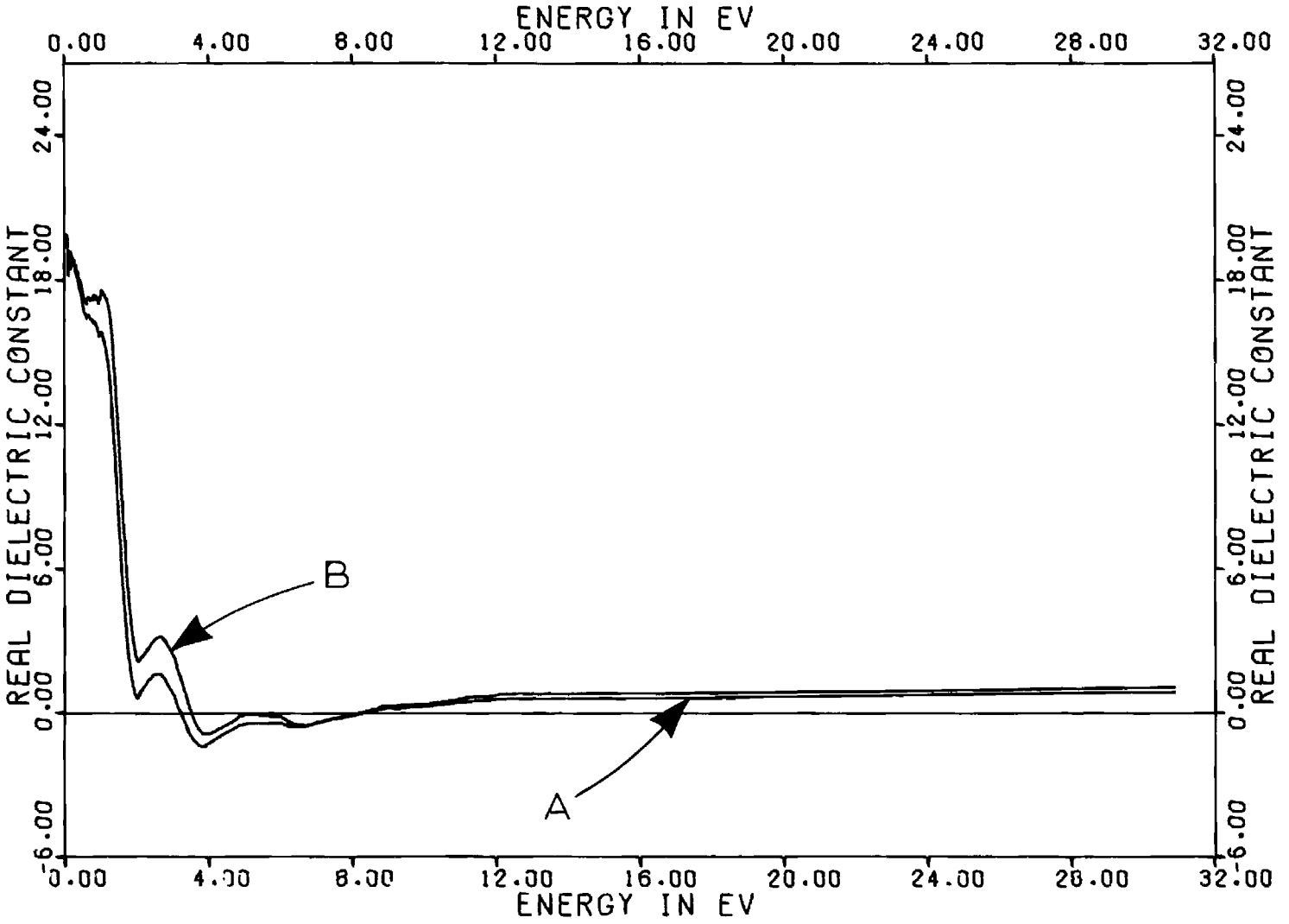

Figure 34. ϵ_1 Calculated by KK Analysis of Reflection Data in Figure 14; (A) With Extrapolation and (B) Without Extrapolation

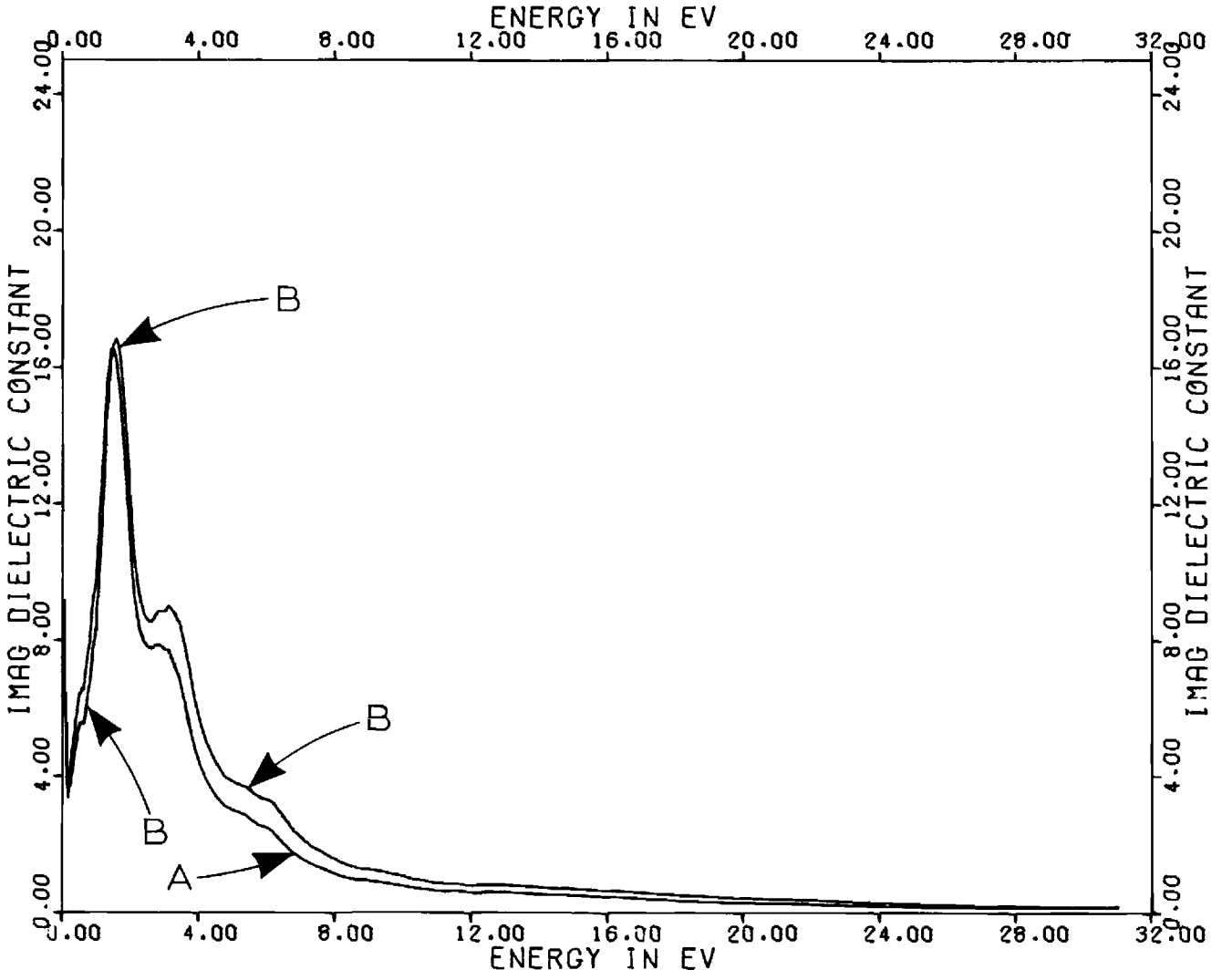

Figure 35. ϵ_2 Calculated by KK Analysis of Reflection Data in Figure 14; (A) With Extrapolation and (B) Without Extrapolation

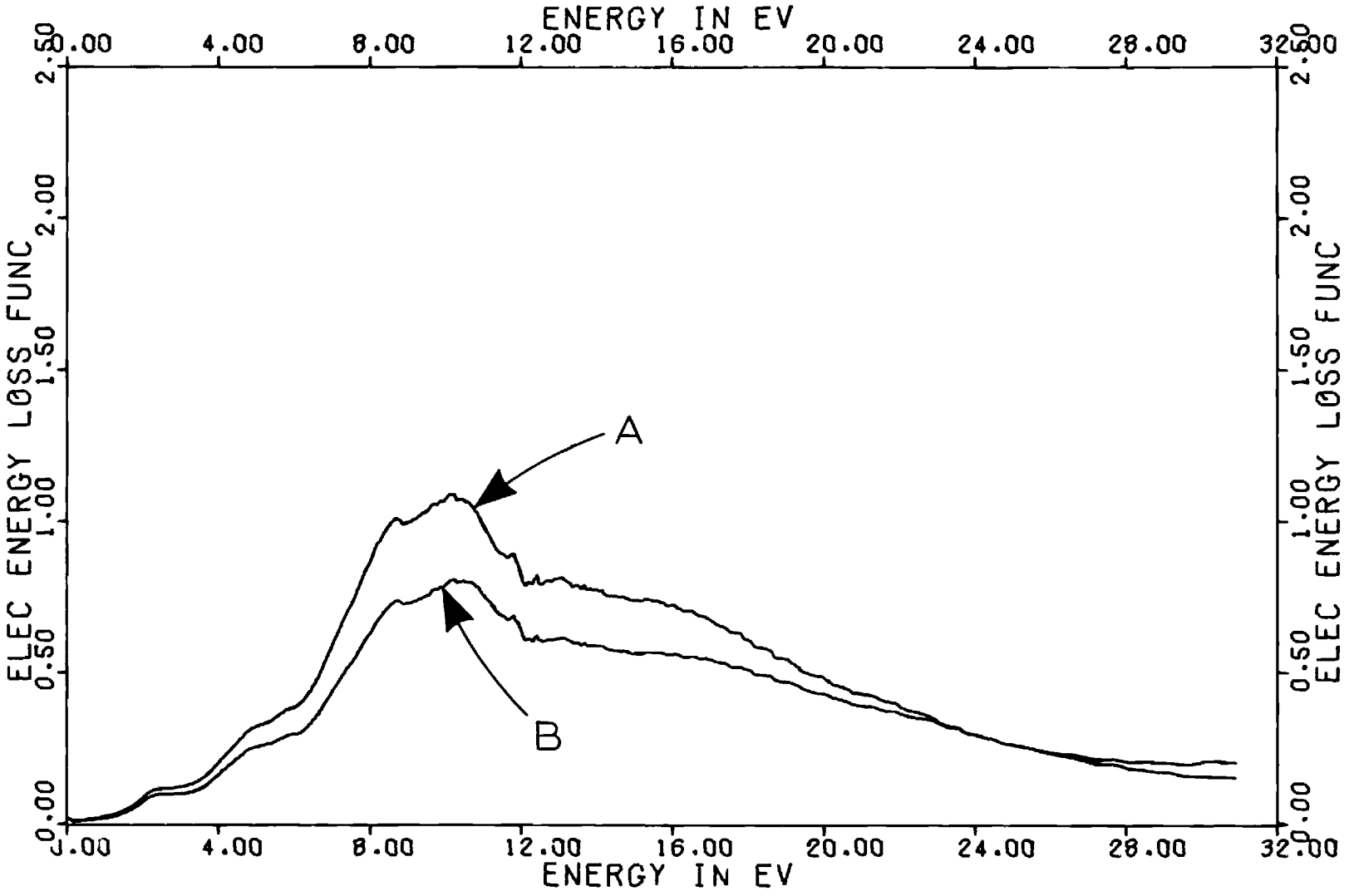

Figure 36. $\mathrm{Im}(1/\tilde{\varepsilon})$ Calculated by KK Analysis of Reflection Data in Figure 14; (A) With Extrapolation and (B) Without Extrapolation

order of 200-300 counts per second, especially in the high-energy region where the reflectance is small. An attempt was made to minimize this error by counting for extended periods of time, i.e. ten seconds. This resulted in typical count totals for I_oR at high photon energies of 2500, for which the theoretical standard deviation is 2%. The relative error was smaller in the regions of higher reflectance, i.e. above 1000 Å in wavelength. The region from 900-1040 Å was exceptional, and the statistical error here is extremely large, often 5% or more variation from point to point. Such random fluctuations tend to compensate in an integral over a large number of data points. The Kramers-Kronig integral was performed in such a way (41) that rapid point to point changes which resulted in little or no net change in the reflectance contributed insignificantly to the integral.

Noise

A second source of error arose from spurious counts in the scalar due to electronic noise primarily originating in the amplifier. This noise was measured by shutting a valve between the monochromator and the storage ring and simulating operation of the reflectometer. Count rates of 1-3 counts per second were observed; negligible compared to other error sources but, nevertheless, systematic in that it increased each recorded count total. The noise was therefore measured after every run and the average of ten 10-second accumulations was subtracted from each data point of the run before calculating the reflectance.

Scattered Light

The existence of non-monochromatic light in the incident beam is a particularly troublesome source of error since it contributes (in general)

an error in the reflectance which is energy dependent. The design of the Pruett-Lien monochromator (26) helps to eliminate scattered light by baffling the light beam before and after it strikes the diffraction grating. In addition the nature of the channeltron is such that photons whose wavelength is greater than about 1500 Å are not detected. To check on the amount of scattered light in the incident beam the LiF filter (which transmits only wavelengths greater than 1040 Å) was placed in the beam at a monochromator setting of $\lambda < 1000$ Å with the result that the count rate was not detectably different from that due to usual electronic noise (2-3 counts/sec). The indium filter was also used for a monochromator setting of $\lambda < 700$ Å (where it does not transmit) with a similar result.

Surface Condition of the Sample

A more significant uncertainty and one more difficult to determine was suspected to exist as a result of non-specular reflectance from the sample surface. An indication of this problem is that in matching the reflectance data in the VUV and XUV regions it was necessary to adjust one of the curves by a multiplicative constant in order to achieve a smooth transition. In the case of Cd_3As_2 the high-energy data were higher in the overlapping region by 15%. Our feeling on the basis of experience in attempting to prepare the surfaces (see Appendix C) is that this difference results from the different strengths and immersion times used in etching the samples (the samples were etched more strongly for the low-energy data). Support for this theory is provided by a comparison of the reflectance of $Cd_{1.5}Zn_{1.5}As_2$ before and after etching (Figures 12 and 13). Such errors resulting from surface roughness will in general contribute to the reflectance by an amount dependent on the wavelength of the incident

light.

In addition to the microscopic roughness caused by etching, a fraction of the surface of our samples was occupied by large ($\simeq$ 0.1 mm diameter) cracks which were presumed to be grain boundaries. These cracks lowered the amount of the reflecting surface by a constant fraction which was independent of wavelength, since the width of the cracks was larger than that of all wavelengths used.

In order to investigate qualitatively the effect of an overall higher reflectance on the calculated optical constants, we have analyzed a reflectance spectrum differing from our measured one by a multiplicative factor of 1.15. The modified data were extrapolated using the same procedure used to extrapolate the experimental data and the results for n, k, ϵ_1, ϵ_2, and the energy loss function are shown in Figures 37-41. The effect is to raise the value of the optical and dielectric constants, particularly at low photon energies. The location of the structure does not appear to be noticeably affected. The electron energy loss function is not significantly affected.

Conclusions and Recommendations

The major conclusions reached on the basis of this research are: (a) that reflectance data at high energies exert a definite influence on the behavior of calculated optical properties even at low energies, (b) that an extrapolation of the reflectance is necessary for an accurate Kramers-Kronig analysis unless the measurements extend to at least five times the energy of the structure of interest, and (c) that sum rules may provide a useful means of optimizing an extrapolation, given an assumed

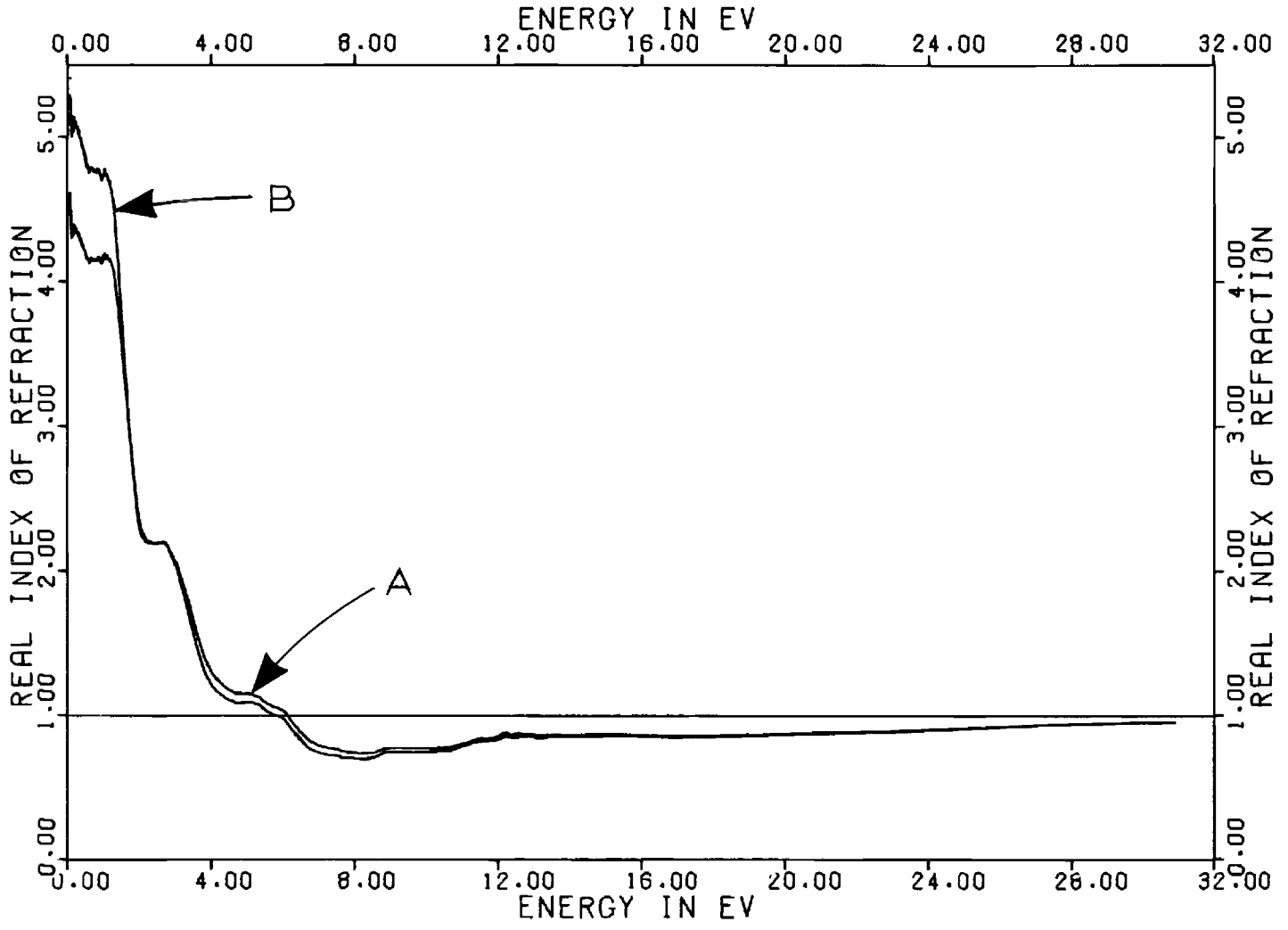

Figure 37. n Calculated Using (A) Reflection Data in Figure 14 and (B) the Same Data Increased by 15%

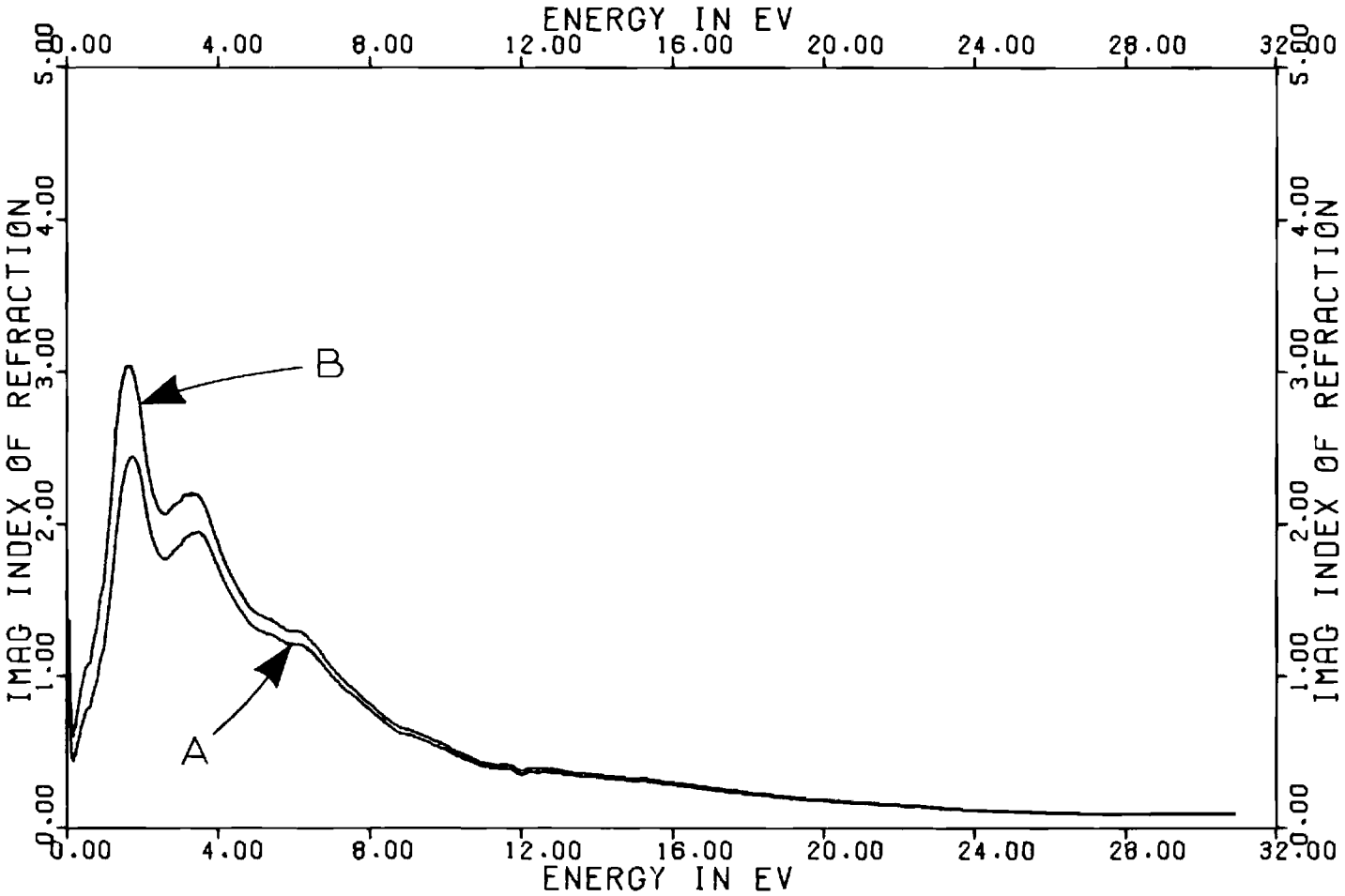

Figure 38. k Calculated Using (A) Reflection Data in Figure 14 and (B) the Same Data Increased by 15%

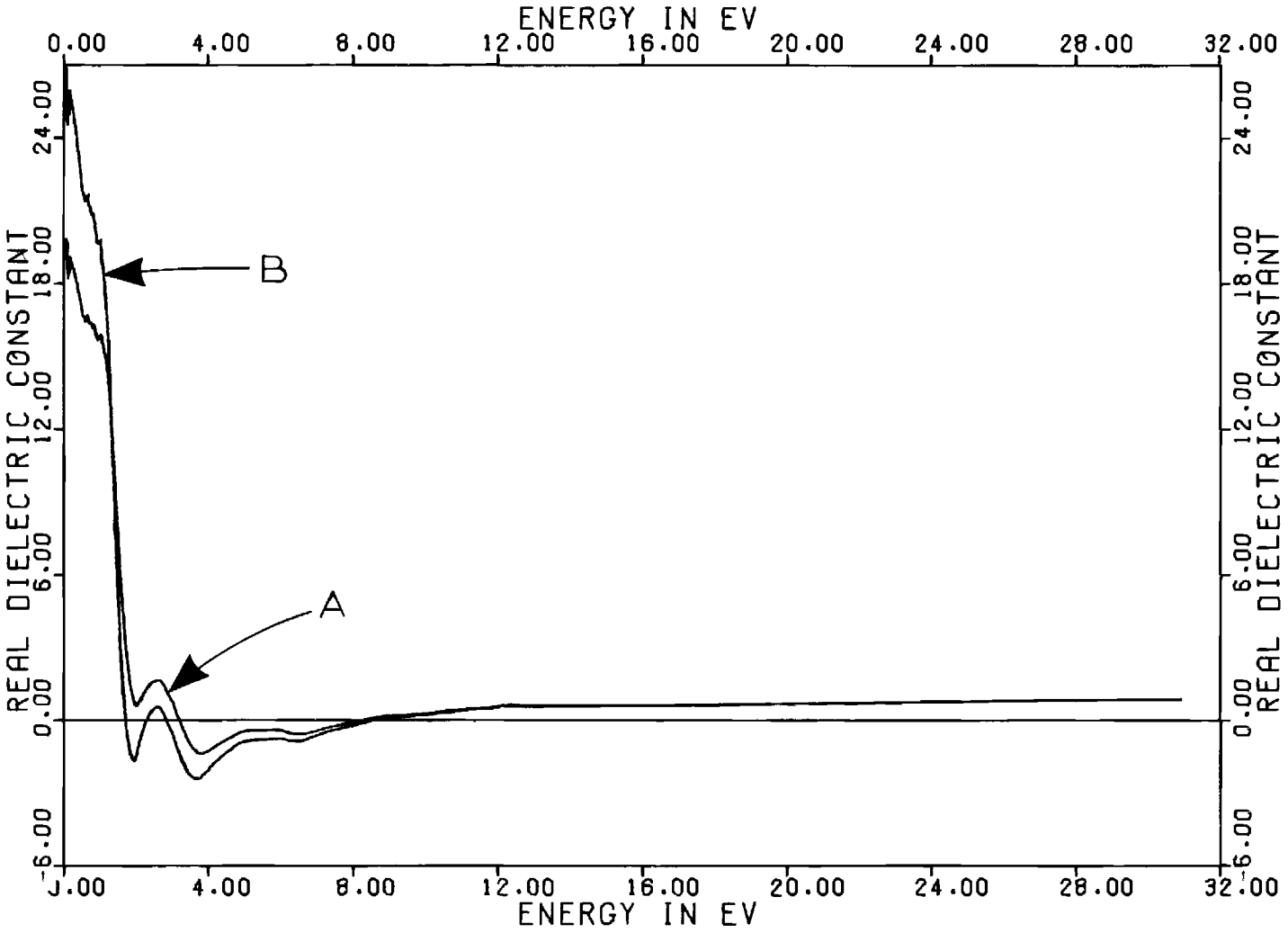

Figure 39. ϵ_1 Calculated Using (A) Reflection Data in Figure 14 and (B) the Same Data Increased by 15%

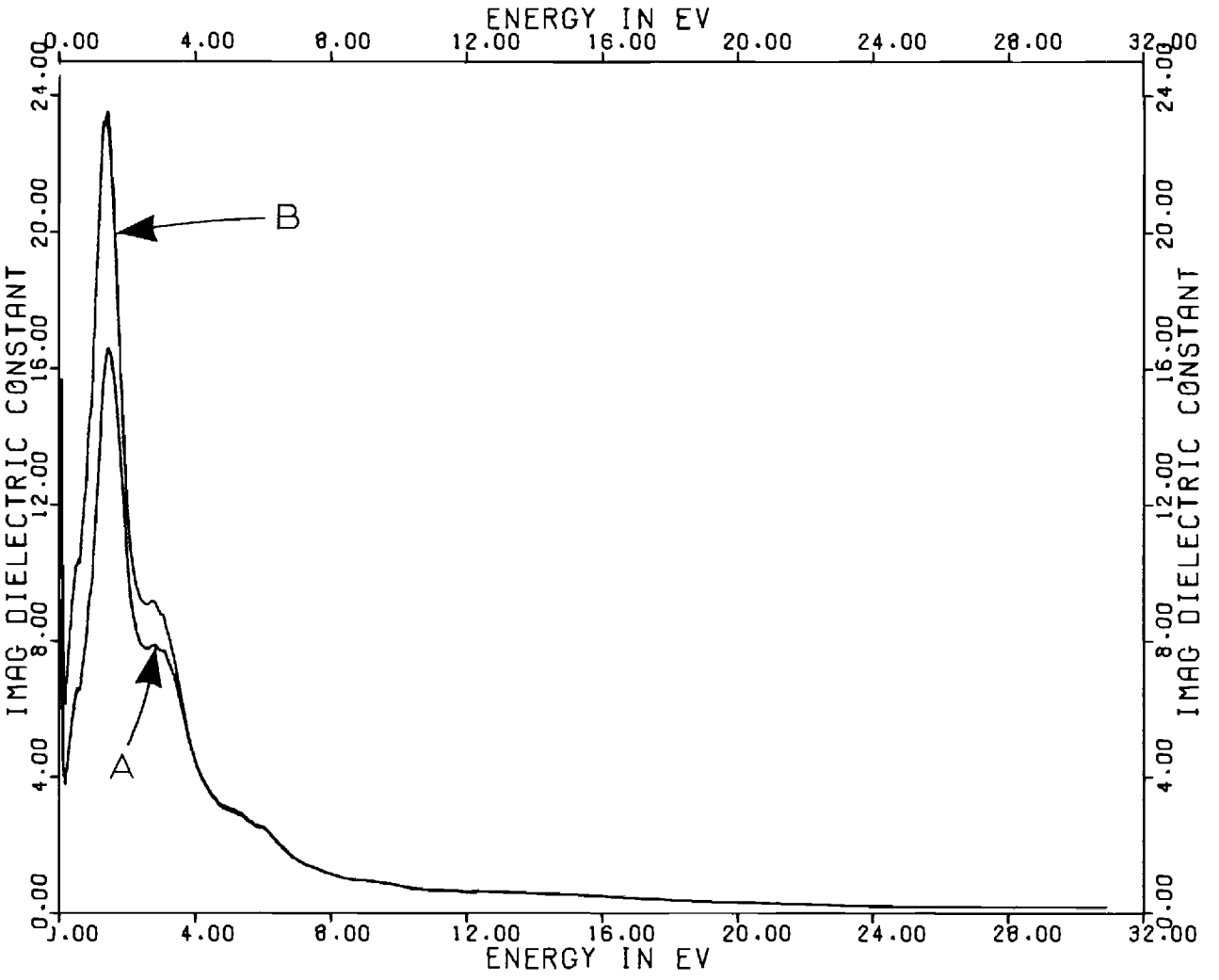

Figure 40. ϵ_2 Calculated Using (A) Reflection Data in Figure 14 and (B) the Same Data Increased by 15%

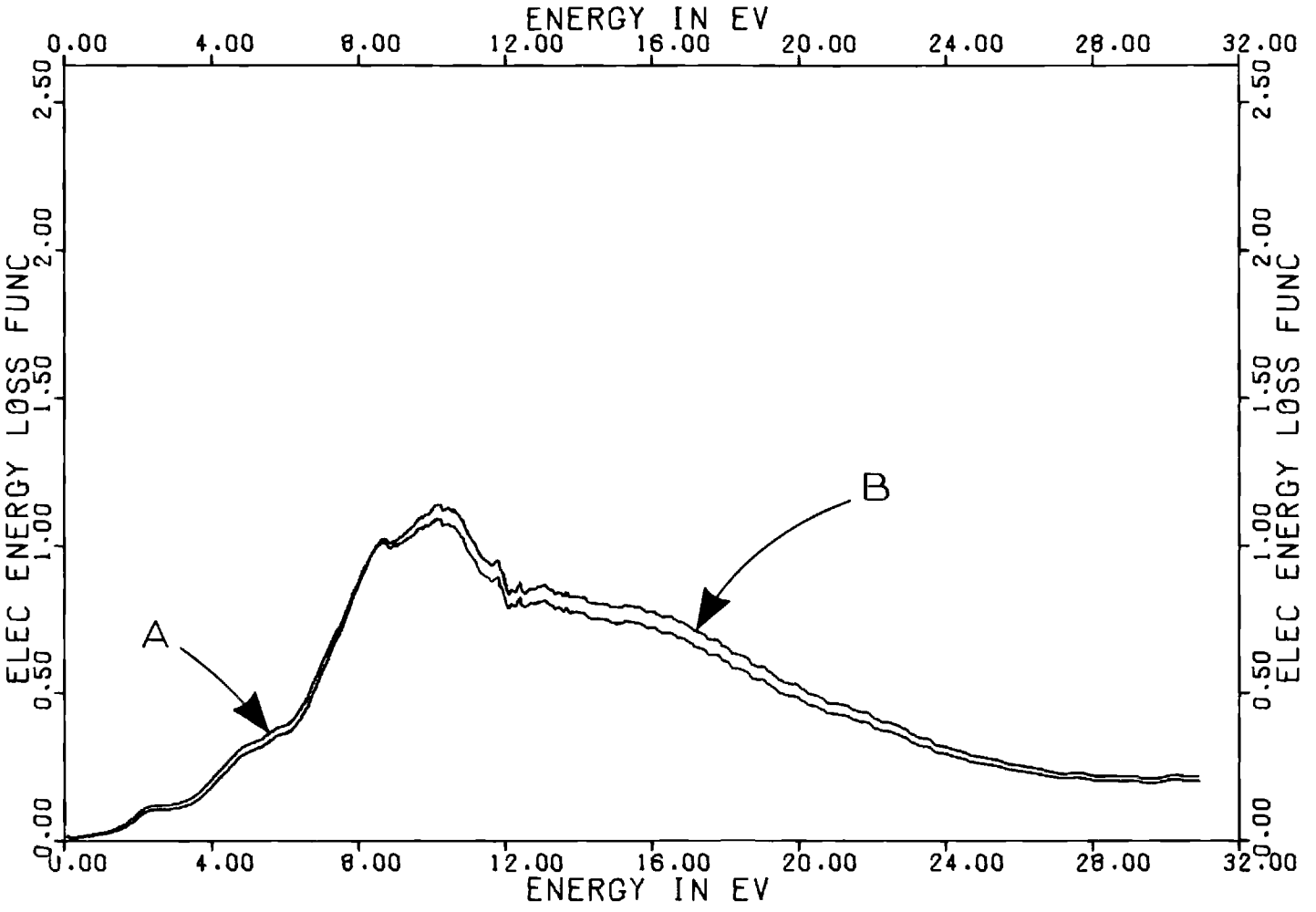

Figure 41. $\mathrm{Im}(1/\tilde{\epsilon})$ Calculated Using (A) Reflection Data in Figure 14 and (B) the Same Data Increased by 15%

functional form, and that SR2 (see Equations 3-4) seems the more sensitive and more appropriate for use with reflectance data. Furthermore, we have concluded from the reflectance data on $Cd_xZn_{3-x}As_2$ samples and a knowledge of the electronic structure of the neutral Cd, Zn, and As atoms (d) that d-bands lie at least 12-13 eV below the lower conduction bands, and (e) that there is an absence of bands in the energy range 15-30 eV below these lower conduction bands.

In addition this research has led us to the opinion that the problem of the surface condition of the sample is the major difficulty in obtaining accurate reflectance data at high energies. Preparing and maintaining a smooth, clean surface for materials which cannot be cleaved or evaporated in situ is a problem upon which much work is needed. We believe that further research on the high-energy reflectance of semiconductors should pursue the problem of preparing samples with good surfaces and of known crystalline orientations. With regard to the $Cd_xZn_{3-x}As_2$ alloy system, we believe that vacuum flash evaporation of thin films, although a new and difficult technique, should be considered. A significant contribution to future research in our group was the development of a system to obtain Auger data which can be correlated with changes in the reflectance due to aging, contamination, etc. It is our opinion that inaccuracies due to surface imperfections were too large to allow us to obtain high quality Auger data on the samples available for this research.

We note that the apparatus which has been developed is capable with little or no modification of transmission as well as reflection measurements. Materials which have bands lying within 30 eV of the conduction

bands may be investigated beyond the plasma energy if thin films can be evaporated. By making use of a grazing incidence monochromator, transmission and/or reflection measurements may be extended beyond 100 eV with this apparatus and using the UWPSL storage ring as a source of radiation. Gahwiller et al. (42) have performed similar measurements using a different instrument. The synchrotron as a radiation source in the extreme ultraviolet has opened an entirely new spectral region for exploration. On the basis of our research we believe that the lack of reflection data in this region prohibits an accurate Kramers-Kronig determination of the dielectric constant even in the near ultraviolet. This statement applies particularly to materials which possess energy bands which contribute to structure in the reflectance at energies in the XUV.

APPENDIX A

SYNCHROTRON RADIATION AS A SPECTROSCOPIC SOURCE

The synchrotron is presently the most suitable source of electromagnetic radiation for spectroscopy in the extreme ultraviolet spectral region ($\lambda < 1000$ Å), and was the source used for obtaining the experimental reflectance data in this research. The general theory of synchrotron radiation is well described in the literature (42-47). A knowledge of the properties of synchrotron radiation was of importance in the design of the reflectometer and optical system and, depending on the sample and wavelength range, may be crucial for correctly interpreting the data. Finally, a careful consideration of the unique nature of radiation from synchrotrons has shown us the possibilities of extending its use into new spectral regions (6). A brief discussion is given of the characteristics of synchrotron radiation, and in particular of the radiation from the UWPSL storage ring which was the source of such radiation in this research.

An expression for the power radiated by a single electron per unit frequency and integrated over all angular dependence has been derived by Schwinger (47) and is

$$P(\omega) = \frac{3^{3/2} e^2 c}{4\pi R^2} \left(\frac{E}{m_0 c^2}\right)^4 \frac{\omega}{\omega_c} \int_{\omega/\omega_c}^{\infty} K_{5/3}(x)\, dx$$

where e is the electronic charge, m_0 is the rest mass of the electron, R is the radius of the orbit, and E is the energy of the electron. The characteristic frequency ω_c is

$$\omega_c = \frac{3c}{2R}\left(\frac{E}{m_0c^2}\right)^3$$

The integrand is a MacDonald function which is defined in terms of Bessel functions of imaginary arguments by

$$K_\nu(x) = \frac{\pi}{2}\frac{I_{-\nu}(x) - I_\nu(x)}{\sin(\pi\nu)}$$

Since the wavelength is a more common experimental parameter than angular frequency we write for the power radiated per unit wavelength the expression

$$P(\lambda) = \frac{3^{5/2}e^2c}{16\pi^2R^2}\left(\frac{E}{m_0c^2}\right)^7\left(\frac{\lambda_c}{\lambda}\right)^3\int_{\lambda_c/\lambda}^{\infty} K_{5/3}(x)\,dx \qquad \text{(A-1)}$$

where the characteristic wavelength is

$$\lambda_c = \frac{2\pi c}{\omega_c} = \frac{4\pi R}{3}\left(\frac{m_0c^2}{E}\right)^3$$

which for the UWPSL storage ring is 260 Angstroms.

The wavelength dependence of the power per unit wavelength is governed by the function

$$G(y) = y^3 \int_y^\infty K_{5/3}(x)\, dx$$

For large and small arguments y, the MacDonald functions may be approximated by well-known functions:

$$x \gg 1 \qquad K_\nu(x) \simeq \frac{\pi}{2} \sqrt{x}\, e^{-x}$$

$$x \ll 1 \qquad K_\nu(x) \simeq 2^{\nu-1} \Gamma(\nu) x^{-\nu}$$

Thus for long wavelengths we have

$$G\left(\frac{\lambda_c}{\lambda}\right) \simeq 2^{2/3} \Gamma(2/3) \left(\frac{\lambda_c}{\lambda}\right)^{7/3}$$

and for small wavelengths we obtain

$$G\left(\frac{\lambda_c}{\lambda}\right) \simeq \frac{\pi}{2} \left(\frac{\lambda_c}{\lambda}\right)^{5/2} e^{-\lambda_c/\lambda}$$

Figure 42 shows a plot of G(y) versus y and of the approximations for large and small arguments. An upper limit on the integral of 40.0 was used in the calculation of G(y). Figure 43 shows a plot of the function $K_{5/3}(x)$ versus x for $0 < x \leq 10.0$, together with the approximations for large and small x.

In addition to the intensity distribution over wavelength, the geometrical nature of the radiation field and the polarization of the radiation are important experimental factors. The radiation from a single

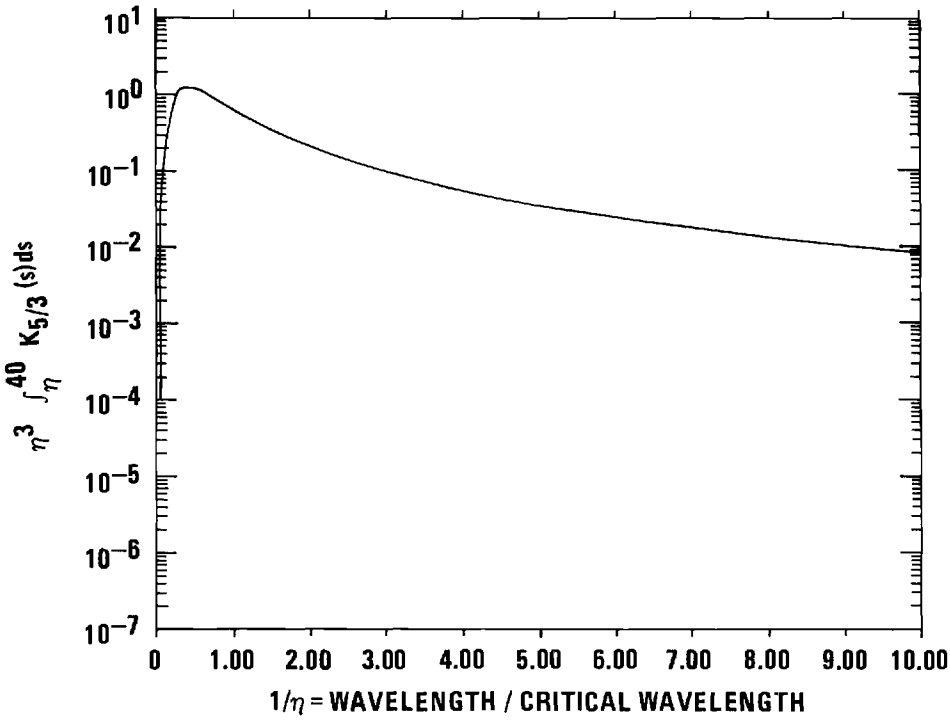

Figure 42. The Function G(η) Plotted versus 1/η

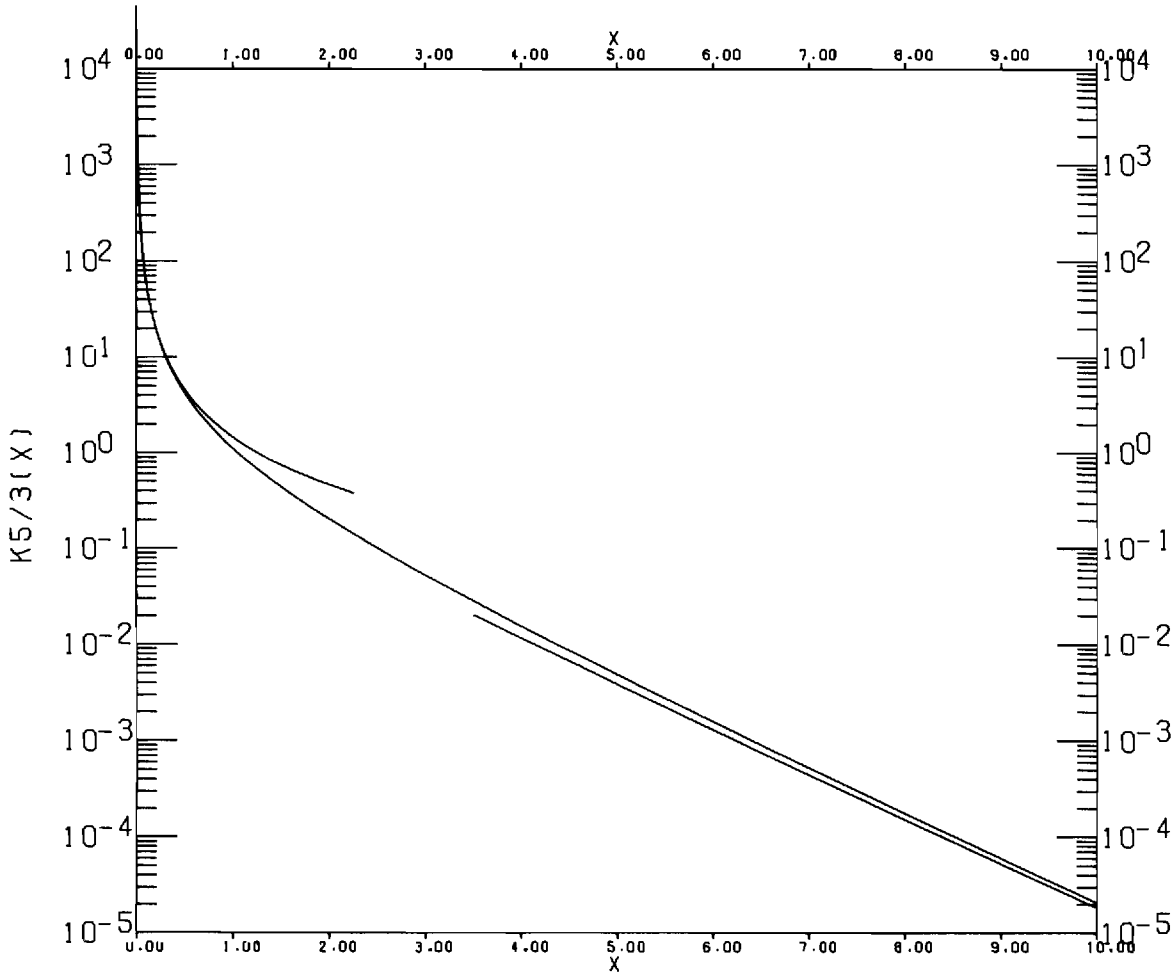

Figure 43. Plot of $K_{5/3}(x)$ versus x (The approximations for small and large arguments are plotted for arguments less than 2.5 and greater than 3.5, respectively.)

electron moving in a horizontal plane is emitted in a cone whose axis is tangent to the electron's orbit. The emission is predominantly in the forward direction of motion of the electron (23). The intensity distribution in the orbital plane away from the tangent to the instantaneous velocity is not experimentally critical since the motion of the electron will sweep a distribution of tangents into any entrance slit of finite width. The distribution of intensity in an angle θ measured away from the orbital plane depends on the frequency, and an expression for the power radiated per unit frequency and solid angle is (10,23)

$$\frac{dP(\omega)}{d\Omega} = \frac{e^2}{3\pi^2 c}\left(\frac{\omega R}{c}\right)^2\left(\frac{1}{\gamma} + \theta^2\right)^2\left\{K_{2/3}^2(\xi) + \frac{\theta^2}{\frac{1}{\gamma^2} + \theta^2}K_{1/3}^2(\xi)\right\}$$

where

$$\xi = \frac{\omega R}{3c}\left(\frac{1}{\gamma^2} + \theta^2\right)^{3/2}$$

and

$$\gamma = \frac{E}{m_0 c^2}$$

The term involving $K_{2/3}(\xi)$ represents the radiation polarized parallel to the orbital plane and is a maximum at $\theta = 0$, i.e. in the orbital plane. The term involving $K_{1/3}(\xi)$ represents the radiation polarized perpendicular to the plane of the orbit. The angle at which this polarization component reaches a maximum depends on frequency. For wavelengths below or near the critical wavelength the polarization component parallel to the orbital plane is much the greater, and almost all the radiation is emitted within two or three milliradians of the orbital plane. For wavelengths much greater than the critical wavelength the angular spread of

intensity becomes significant, and the polarization becomes strongly dependent on the angle θ; thus different parts of the radiated beam possess different polarizations. The exact dependence is a function of the machine parameters R and E as well as the ratio λ/λ_c. Figures 44 and 45 show the power per unit frequency as a function of the angle θ for each polarization and for their sum.

Figure 46 shows the distribution in the angle θ of the total intensity (both polarization components) for machine parameters characteristic of the UWPSL storage ring at several wavelengths. For the longer wavelengths a larger vertical angle must be accepted by the apparatus in order to collect the total emitted intensity. A useful parameter for experimental design is the rms angle of the radiation given by (24)

$$< \theta^2 >^{1/2} = \frac{m_0 c^2}{E} \left(\frac{\lambda}{\lambda_c}\right)^{1/3} = \frac{m_0 c^2}{(5.59)^{1/3}} \left(\frac{\lambda}{R}\right)^{1/3}$$

The value of $< \theta^2 >^{1/2}$ for the UWPSL machine at 10 μm is 15.5 milliradians (see Figure 46) and includes about 80% of the radiated power.

Another useful expression for experimental purposes is the number of photons emitted per second and Angstrom bandwidth into one milliradian of horizontal angle, which is

$$N(\lambda)\Delta\lambda = NP(\lambda) \frac{\lambda}{hc} \frac{10^{-3}}{2\pi}$$

where N is the number of circulating electrons and $P(\lambda)$ is given in Equation A-1. In terms of easily measured quantities the expression is given by Gahwiller et al. (42) as

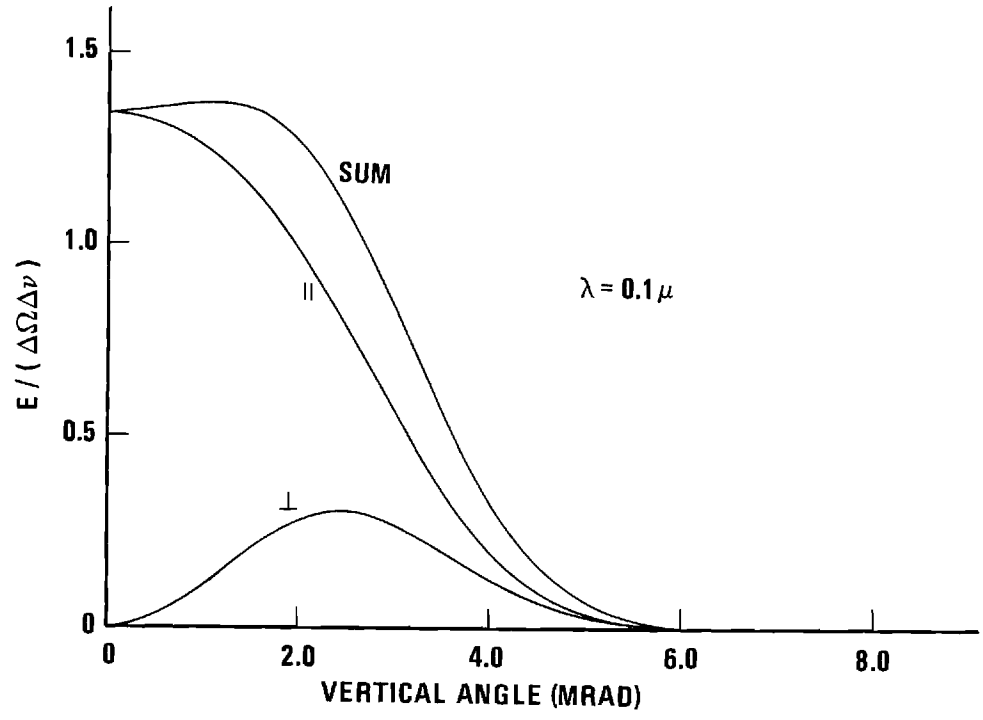

Figure 44. Distribution of Intensity (in Arbitrary Units) of the Two Linear Polarization Components of Radiation from the UWPSL Storage Ring (λ_c = 260 Å) at λ = 1000 Å (The vertical angle is measured from the electron's orbital plane. The component polarized parallel to the orbital plane is the middle curve.)

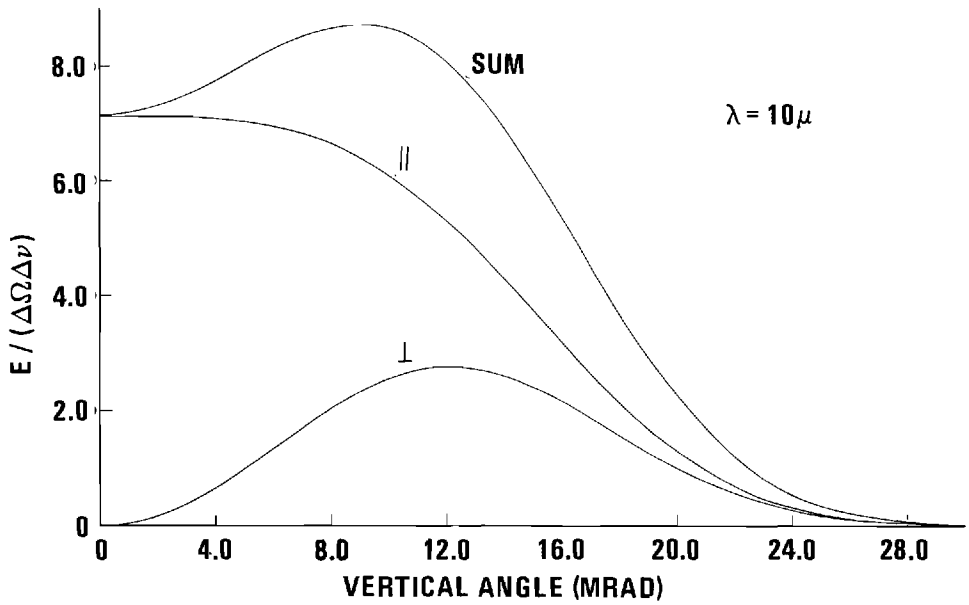

Figure 45. Distribution of Intensity (in Arbitrary Units) of the Two Linear Polarization Components of Radiation from the UWPSL Storage Ring (λ_c = 260 Å) at λ = 10 μ (The vertical angle is measured from the electron's orbital plane. The Component polarized parallel to the orbital plane is the middle curve.)

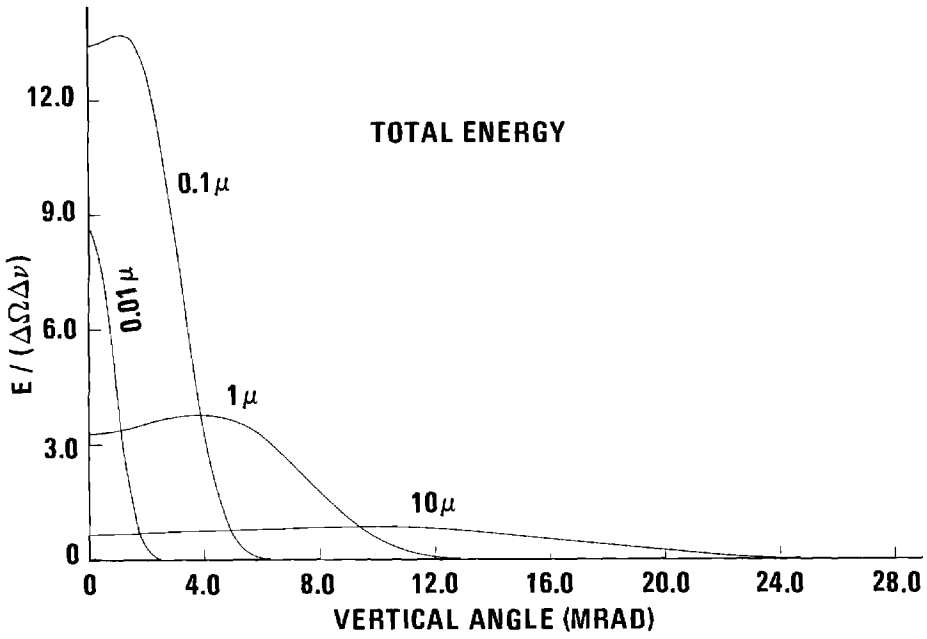

Figure 46. Distribution of Total Power per Unit Frequency (in Arbitrary Units) for λ_c = 260 Å as Radiated into the Angle Measured from the Electron's Orbital Plane for Several Wavelengths

$$N(\lambda)\Delta\lambda = 0.78 \times 10^{12}\, G\left(\frac{\lambda_c}{\lambda}\right) [\lambda(\text{Å})]\, J(\text{mA})\, \frac{[E(\text{GeV})]^7}{[R(\text{m})]^2}\, \Delta\lambda$$

where J is the electron current expressed in milliamperes and $G\left(\frac{\lambda_c}{\lambda}\right)$ is given in Equation 6. For parameters appropriate to the UWPSL storage ring (E = .24 GeV, R = 0.65 meters) we have

$$N(\lambda)\Delta\lambda = 0.86 \times 10^{8}\, G\left(\frac{\lambda_c}{\lambda}\right) [\lambda(\text{Å})]\, J(\text{mA})\, \Delta\lambda$$

If a constant resolution $\Delta\lambda/\lambda$ is maintained, the radiated power at long wavelengths is proportional to $\lambda^{-4/3}$. This rather slow decrease (compared for instance to a black body) implies that the synchrotron may provide useful intensity even in the infrared spectral region (6).

APPENDIX B

AUGER SPECTROSCOPY

The theory of Auger spectroscopy as a tool for surface analysis is described in the literature (48-50). A brief summary of the method used in this research is provided for those unfamiliar with the technique.

Emission of an Auger electron from an atom involves the ionization of an inner atomic shell, thereby creating a vacancy which may be filled by an electron from a higher energy level in the atom. In the case of Auger emission, two electrons in the higher energy shell are involved; one electron fills the inner shell vacancy thereby losing an amount of energy ΔE which is transferred to the second electron in a direct coupling process. The second electron (the Auger electron) is in general emitted from the atom with kinetic energy ΔE less the ionization potential of the shell from which it originated. Since in a multi-electron atom a vacancy on the (for instance) inner most shell may be filled by electrons from any one of several higher energy shells, Auger electrons may be emitted with any one of several energies in a series which is characteristic of the particular element. With the aid of a standard published chart of Auger energies one may identify elements by the energies of their Auger electrons. Auger spectroscopy consists of the production of inner shell ionization and the energy analysis of the emitted Auger electrons to identify the elements present. Since an Auger electron produced at a depth of more than a few Angstroms has small probability of escaping the

sample without undergoing an inelastic collision, Auger spectroscopy is sensitive only to the first few atomic layers of a surface. Auger spectroscopy thus provides a method of detecting extremely small amounts of contaminants on a surface. (It must be stated that there is disagreement about the depth below the surface from which an Auger electron may escape without undergoing an inelastic collision.)

In this research Auger electrons were produced at the sample through bombardment by a primary beam of electrons of about 2500 eV energy. The electron current I(E) was received at the phosphor-coated screen and measured as a function of E, the retarding potential placed on the intermediate grids. If N(E)dE represents the number of electrons received with energies between E and E + dE, then the signal is

$$I(E_o) = \int_{E_o}^{\infty} N(E)\, dE$$

and $N(E) = -\frac{dI(E)}{dE}$ is the electron energy distribution function. Maxima exist in N(E) at energies corresponding to the Auger energies characteristic of the surface atoms. These maxima are usually small, however, and exist in a relatively high background (27) of inelastically scattered primary electrons and secondary electrons excited from the sample. These true secondary electrons (as distinct from the Auger electrons which are emitted in the process of filling the vacancies left by the true secondaries) exhibit a broad peak upon which the relatively much weaker Auger peaks are superimposed, often appearing as inflection points on the slope of a stronger maximum. In general the location of the Auger structure is not easily observed from the energy distribution function N(E) due to its

weak signal strength relative to other sources of electron current. Considerable amplification may be necessary to resolve Auger structure and phase-sensitive detection is usually employed.

If we write for the voltage E at the retarding grids a constant E_o plus a small sinusoidal component A sin(ωt), then we may expand I(E) in a Taylor's series about E_o:

$$I(E) = I(E_o) + \left.\frac{dI(E)}{dE}\right|_{E_o} (E-E_o) + \frac{1}{2!}\left.\frac{d^2I(E)}{dE^2}\right|_{E_o} (E-E_o)^2 \qquad \text{(B-1)}$$

$$+ \frac{1}{3!}\left.\frac{d^3I(E)}{dE^3}\right|_{E_o} (E-E_o)^3 + \ldots$$

We now identify

$$\left.\frac{dI(E)}{dE}\right|_{E_o} = -N(E_o) \qquad \text{and} \qquad (E-E_o) = A \sin(\omega t)$$

so that Equation B-1 becomes

$$I(E) = I(E_o) - A\,N(E_o)\sin(\omega t) - \frac{1}{2}\left.\frac{dN(E)}{dE}\right|_{E_o} \sin^2(\omega t)$$

$$+ \frac{1}{6}\left.\frac{d^2N(E)}{dE^2}\right|_{E_o} \sin^3(\omega t) + \ldots$$

If we now assume that $A \ll E_o$ so that we may approximate I(E) by a third order expansion about E_o and make use of the trigonometric identities

$$\sin^2(\omega t) = \frac{1}{2}(1 - \cos 2\omega t)$$

$$\sin^3(\omega t) = \frac{1}{4}\left[3\sin(\omega t) - \sin(3\omega t)\right]$$

we obtain

$$I(E) = I(E_o) - \frac{1}{4}A^2\left.\frac{dN}{dE}\right|_{E_o} - \left\{A\,N(E_o) + \frac{1}{8}A^3\left.\frac{d^2N}{dE^2}\right|_{E_o}\right\}\sin(\omega t)$$

$$+ \frac{1}{4}A^2\left.\frac{dN}{dE}\right|_{E_o}\cos(2\omega t) + \frac{1}{24}A^2\left.\frac{d^2N}{dE^2}\right|_{E_o}\sin(3\omega t)$$

to third order.

Thus to the extent that the sinusoidal component is sufficiently small that the third order expansion accurately represents I(E), the signal received at the screen at the second harmonic of the perturbing frequency is proportional to the derivative of the energy distribution function. In this function, the Auger portion of the signal is enhanced against the relatively constant background signal of the inelastically scattered primaries, which does not contribute significantly to the derivative. The broad secondary peak has a slowly varying derivative which is essentially constant over the narrow region taken by an Auger peak. An Auger maximum which is merely an inflection point in N(E) becomes a true peak in the derivative. As an Auger peak is scanned in energy, the derivative of N(E) passes through a pronounced maximum followed immediately by a minimum, so that the shape characteristic of an Auger process is readily identifiable. Thus, although the signal strength at frequency 2ω is much smaller than that at the perturbing frequency ω, the resolution of Auger structure is made easier by the elimination of the major

noise problems.

A block diagram of the electronics used to detect the Auger spectrum is given in Figure 47. The correct biasing of the retarding grids and screen to yield the maximum sensitivity and resolution has been discussed in the literature (50). We followed the present scheme of Tharp et al. for the three-grid analyzer design. The first grid (nearest the sample) was held at ground to provide a field-free region for the electrons during the flight from the sample to the retarding field. The second and third grids were shorted together electrically, and the retarding voltage applied. The perturbing sinusoidal component was supplied by a Hewlett-Packard model 202c oscillator and was about six to twelve volts peak-to-peak. The signal was taken from the screen. The frequency was chosen to minimize rf interference from other equipment in the room. The "constant" retarding voltage E was supplied by a Kepco model 123A programmable power supply which was programmed to ramp at about 1 volt/second from 100 V to 1500 V. A voltage which was proportional to this ramping voltage provided the horizontal axis input to the Mosely model 2D-2M X-Y recorder.

In our three-grid detection optics there was no grounded grid between the retarding grids and the screen, therefore capacitive coupling existed which introduced a signal of frequency ω at the screen. This signal was electronic in origin. A capacitance nulling circuit (51) was used to supply the screen with a voltage whose amplitude and phase were adjusted to interfere destructively with the capacitance coupling signal. In addition the screen was biased at a constant +100 volts relative to ground to enhance its electron collecting capabilities.

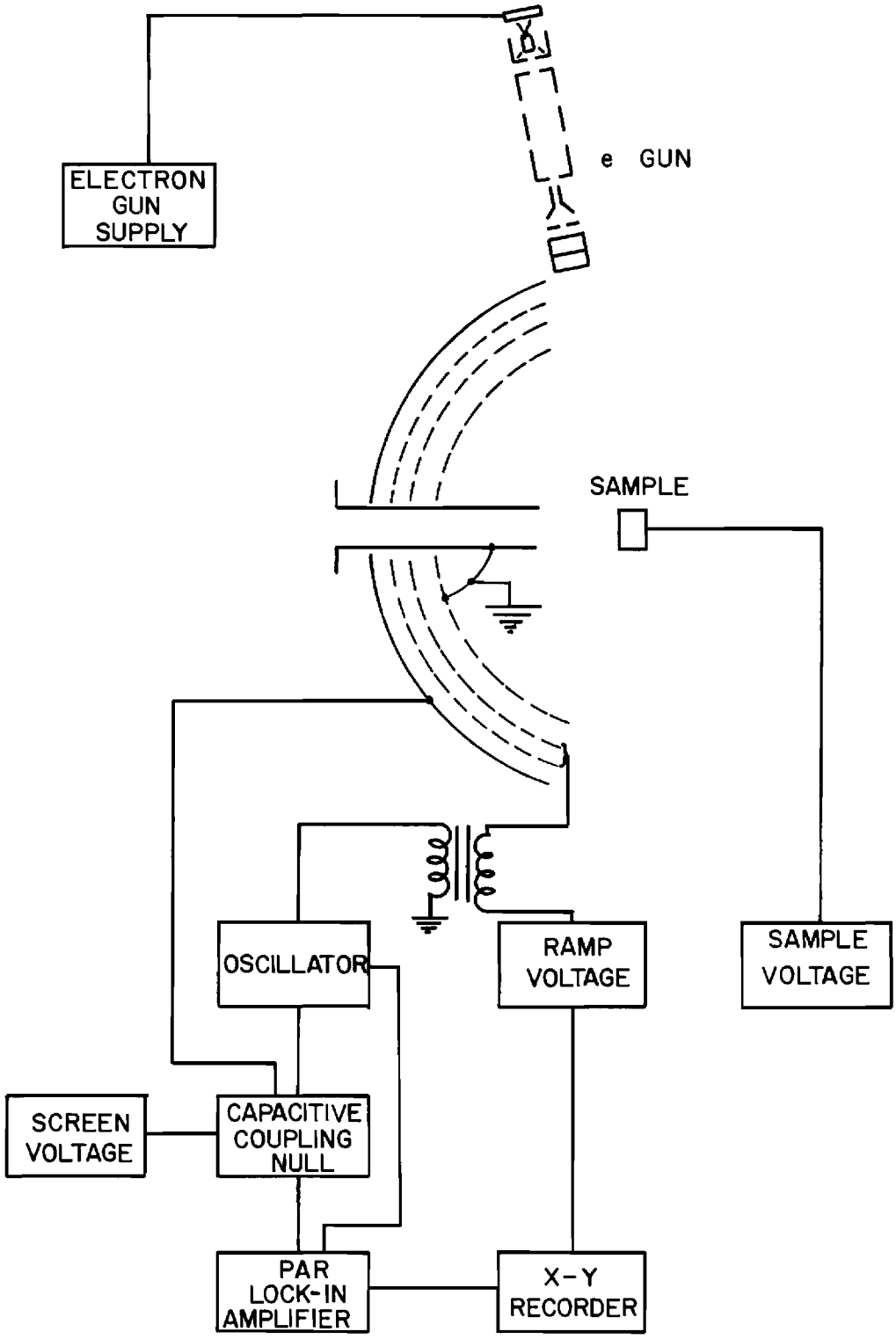

Figure 47. Electronics Used for Auger Spectroscopy

The phase-sensitive detection was effected by a PAR model HR-8 lock-in amplifier which possessed the capability of synchronizing with an externally produced reference signal. The reference signal was supplied by a frequency-doubling circuit (52) which the HP 202C oscillator was modified to incorporate and which supplied a small (one to two volts rms) signal at frequency 2ω, where ω was the frequency of the perturbing voltage applied to the retarding grids. The electron current collected by the screen was converted to a voltage signal which was input to the lock-in amplifier. A phase shift was introduced to phase-match the 2ω component of this signal with the reference channel. The resulting output of the amplifier was proportional to the second harmonic of the electron current for a particular retarding voltage E_o and thus was a relative value of $\left(\frac{dN(E)}{dE}\right)_{E_o}$. The output of the HR-8 served as the vertical axis drive for the x-y recorder. As the retarding potential was ramped, an X-Y plot was generated of relative values of $\left(\frac{dN(E)}{dE}\right)_{E_o}$ versus E_o, from which the energy values of the Auger peaks were extracted.

An example of an Auger spectrum on stainless steel taken during the early testing of the apparatus is shown in Figure 48. Atmospheric contaminants are detected as well as the underlying substrate, which is presumably the source of the iron. The oxygen peak arises from the KLL Auger transition which denotes the ionization of the K electron shell which is filled by an electronic transition involving two L-shell electrons, one of which becomes the Auger electron. The location of the peak is taken to be the minimum of the recorder deflection, which is near the 512 eV tabulated value for the oxygen KLL transition. The KLL carbon peak at 273 eV was used to calibrate the apparatus during each run.

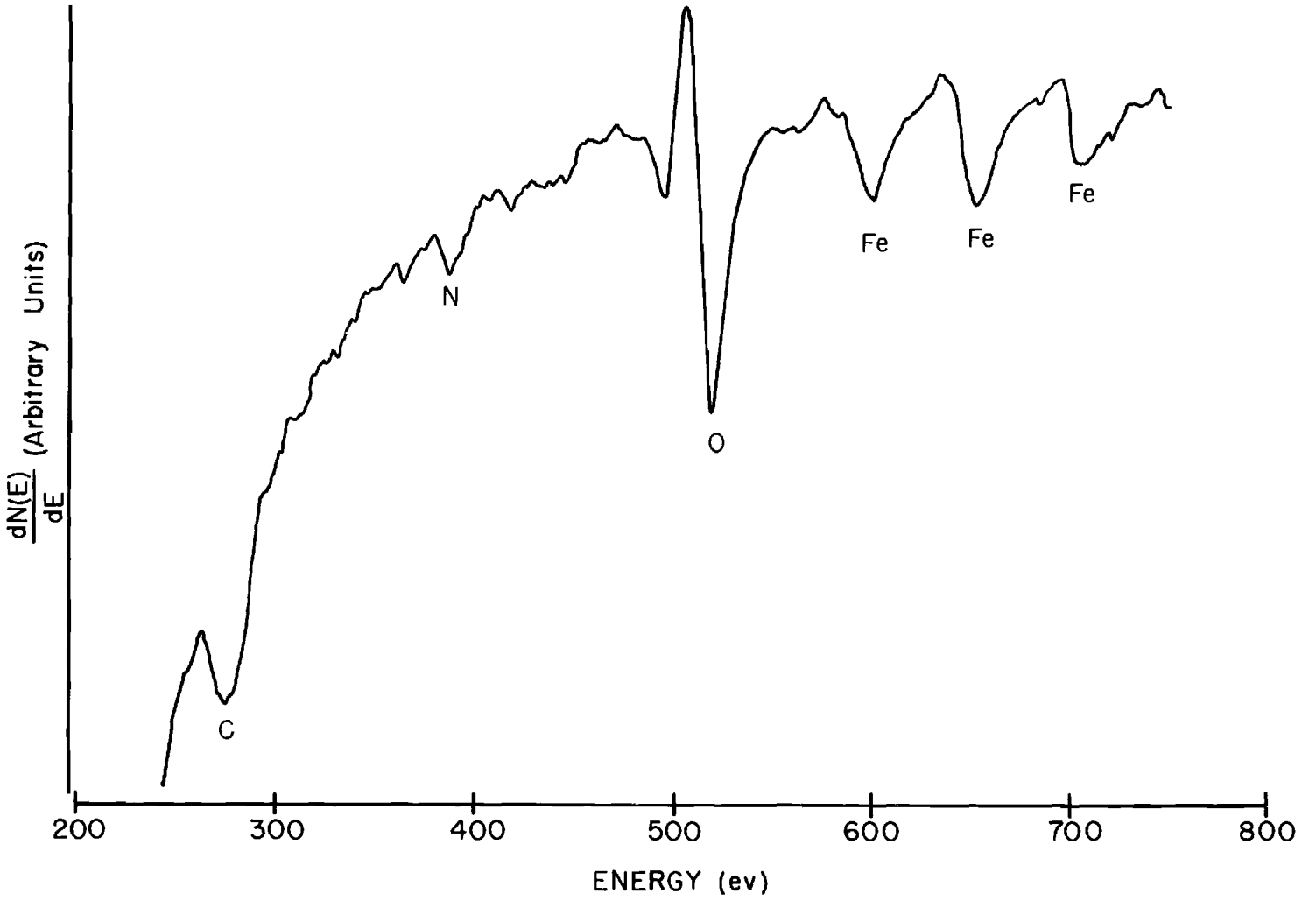

Figure 48. Auger Spectrum for Stainless Steel (The structure is labeled as being characteristic of a particular element.)

APPENDIX C

SAMPLE SURFACE PREPARATION

The surface preparation of samples of the $Cd_xZn_{3-x}As_2$ alloy system was the subject of some investigation in the course of this research. The samples as received had been serially cut from the grown ingots by a string-saw which left a rough, visibly uneven surface on the two flat sides, which were often not parallel. The softness of the sample material however made grinding unnecessary, since a coarse polish removed stock rapidly from the surface. All polishing was done on a motor-driven wheel tightly covered by a Buehler AB microcloth. The motor was operated from a variac supply which allowed a choice of polishing speeds. During polishing the samples were affixed by a resin with a low-temperature melting point (about 150°F) to a cylindrical steel plug 1 inch in diameter and about 1 inch long. This plug was held concentrically in a 3 inch O.D., 1 inch I.D. "doughnut" by a set screw. This device, designed originally by Livesay (53) allowed the sample surface to be brought flush with the much larger surface of the outer doughnut and supplied a uniform pressure to the sample surface during polishing. In addition, a uniform orientation was maintained between the sample surface and the wheel, eliminating "rounding," i.e. the production of a convex surface.

The initial polish used was a slurry of water and 1.0 μm alumina particles. This abrasive removed stock from the surface at such a rate that one to two hours of polishing resulted in a flat, visibly shiny

surface, flush with the surface of the outer doughnut. No further adjustment of the sample relative to the holder was made during the polishing procedure.

The next step was the subject of some experimentation. Both 0.3 μm alumina in distilled water and 0.25 μm diamond in oil were used as polishing abrasives. It was observed that, while both materials were capable of producing a surface which appeared smooth to the eye (except for the cracks to be discussed shortly), the alumina polish produced a surface which appeared to be much rougher when viewed under a phase-contrast microscope (see Figure 49(A)). The diamond polish, on the other hand, initially produced an "orange peel" surface, dense in small circular craters or pits which were visible to the eye. It was found that a slower polishing speed (about four revolutions per second of our 8 inch diameter wheel) and the frequent addition of cooling oil to the cloth greatly reduced the size and number of the pits. The resulting surface, shown in Figure 49(B) exhibited relatively few scratches. The final polish was a dilute suspension of 0.05 μm alumina particles in distilled water. The sample was usually polished for 90 minutes for reasons to be discussed below, although little improvement could be seen after about 30 minutes (see Figure 50).

After mechanical polishing, the samples were removed from the holder and etched using a 5% solution by volume of bromine in methanol, an etchant recommended by the growers of the alloy crystals as one which removed Cd, Zn, and As at roughly equal rates. The samples were etched for periods of time ranging from 5 to 30 seconds. In cases where the mechanical polishing with 0.05 micron alumina was performed for less than

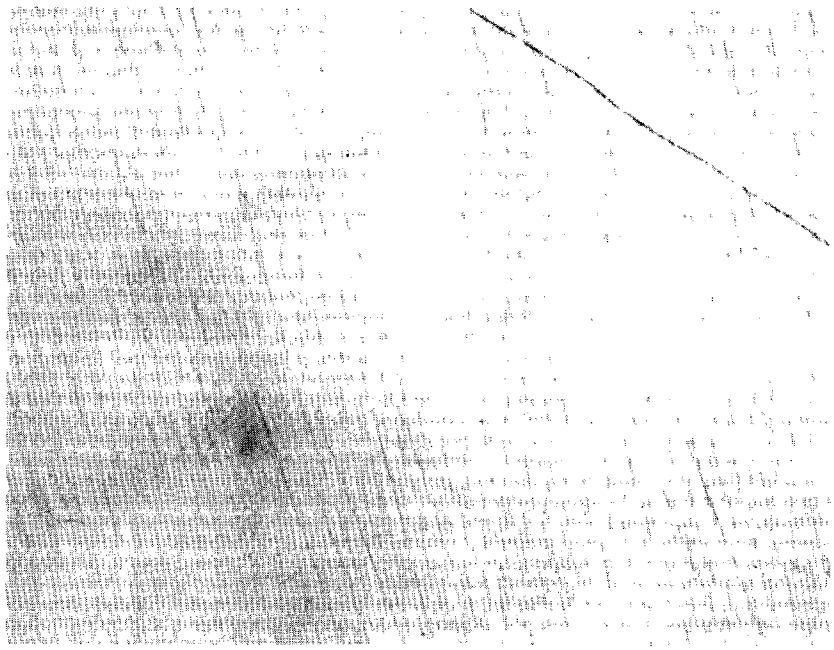

(A)

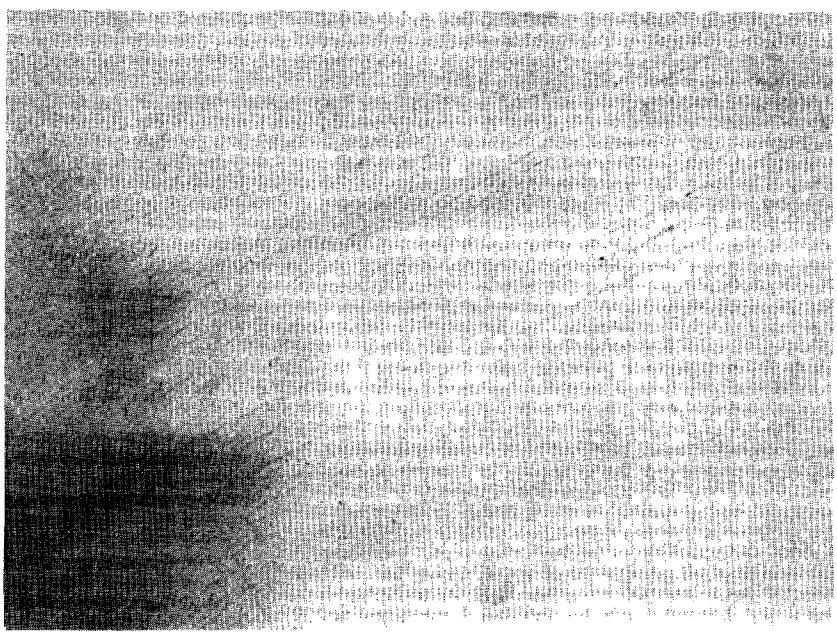

(B)

Figure 49. Surface of Cd_3As_2 Seen Through Phase-Contrast Microscope (Magnification Factor 500) after Polishing with (A) 0.3 μm Alumina and (B) 0.25 μm Diamond

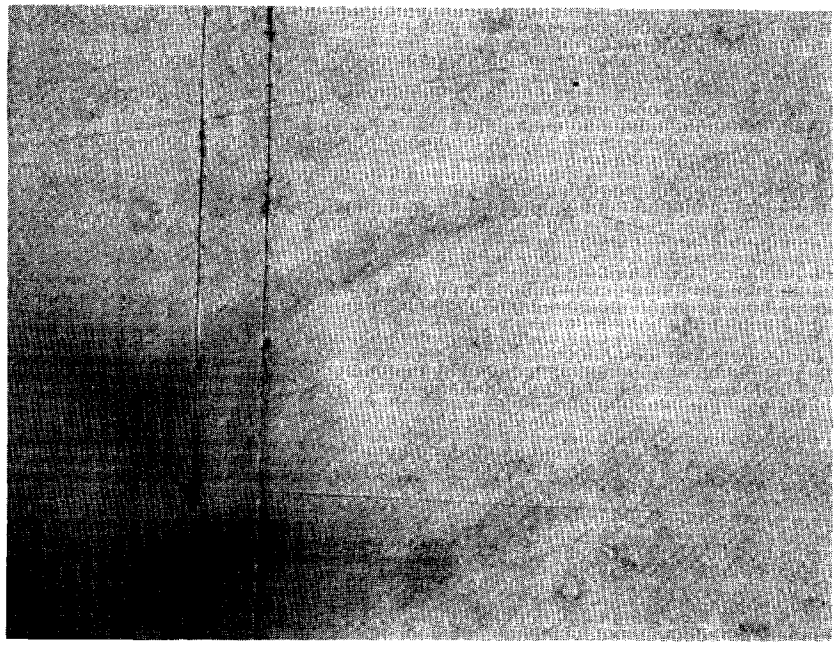

(A)

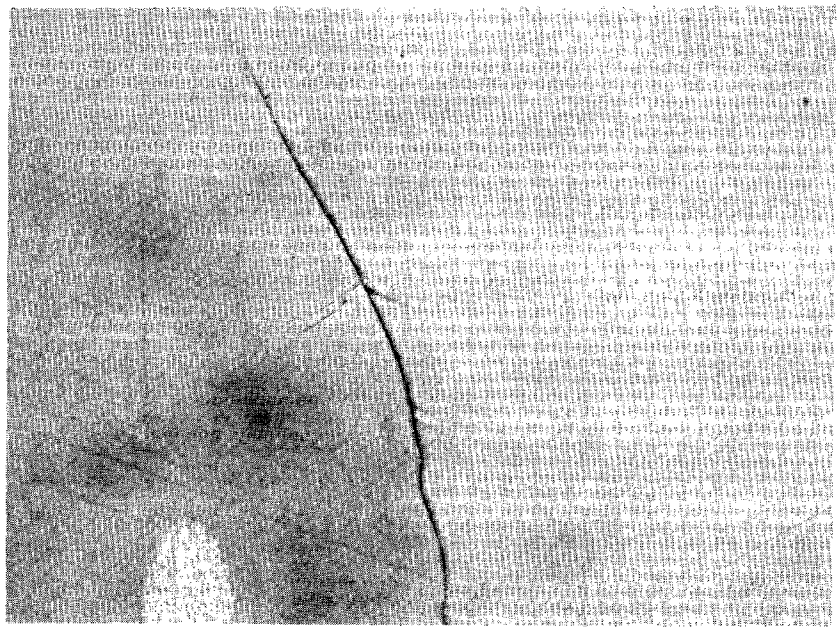

(B)

Figure 50. Surface of Cd_3As_2 Seen Through Phase-Contrast Microscope (Magnification Factor 500) after Polishing with 500 Å Alumina for (A) 30 Minutes and (B) 60 Minutes

about an hour, etching for 30 seconds or more left the surface badly discolored. In every case, regardless of polishing time, the etch left a dulled surface. The microscope revealed a roughened surface and the presence of scratches, presumably the reappearance of scratches produced by the earlier mechanical polishes.

These results are subject to either of two interpretations. It is possible that the fine (0.05 μm alumina) polish actually removed the scratches made by the prior polishes, but was insufficient to remove the strain damage below the surface made by the abrasive particles. The damaged material would probably be preferentially removed by the etch, creating grooves in the surface. Alternatively, the fine polish may have acted simply to fill up the scratch marks of the prior polish and to coat the entire surface with amorphous material (or perhaps a microcrystallite powder) abraded from the surface (a Beilby layer) (54,55). An argument for the first hypothesis is made by the fact that the longer polishing time with the fine polish reduced the discoloration produced by the etch. Attempts to obtain a Laue x-ray diffraction photograph of the unetched samples yielded photographs which showed a diffuse halo (a pattern characteristic of an amorphous substance) in which the Bragg maxima were barely distinguishable. It is conceivable that the longer polishing times with the fine polish produced a thick enough amorphous layer that 30 seconds of etching was insufficient to expose the scratches.

Electron photo-micrographs were taken of two samples identical in alloy composition, one which had been polished only with 0.25 μm diamond and one which had been additionally polished with 0.05 μm alumina for 90 minutes. Each sample was photographed, etched for 30 seconds and re-

photographed. In each case the etch produced a surface whose texture appears rougher, although the appearance of additional scratches is not evident in the photographs (see Figures 51 and 52). In order to establish the effect of etching on the reflectance data, reflection runs were made on $Cd_{1.5}Zn_{1.5}As_2$ before and after etching. The unetched surface exhibited a slightly higher optical reflectance over the entire wavelength range from 400-1400 Å. Interestingly, the reflectance seems to differ only by a multiplicative factor, with the shape of the curve unaffected. This is nevertheless sufficient to cast doubt on the accuracy of the Kramers-Kronig calculation of the optical constants, which depends on the absolute value of the reflectance.

A further difficulty with the samples was the appearance of cracks in the surface during polishing. The samples were reputedly single crystals and x-ray exposures of several samples showed a Laue pattern, although obscured in a diffuse background. These very visible cracks appeared, however, to penetrate the entire thickness of the sample, as they showed no tendency to "polish out" and in fact grew more distinct with increased polishing. Upon repeated heating (necessary in mounting the samples for polishing) several samples actually broke into two or more fragments, always along the crack lines. The density of cracks was highest for those samples whose alloy composition was primarily Cd_3As_2, but no sample was completely free of them. The cracks appear in several of the photographs. The effect of such cracks would be to lower the absolute value of the reflectance for all wavelengths by a multiplicative factor since a portion of the surface was not able to contribute to the specular reflectance.

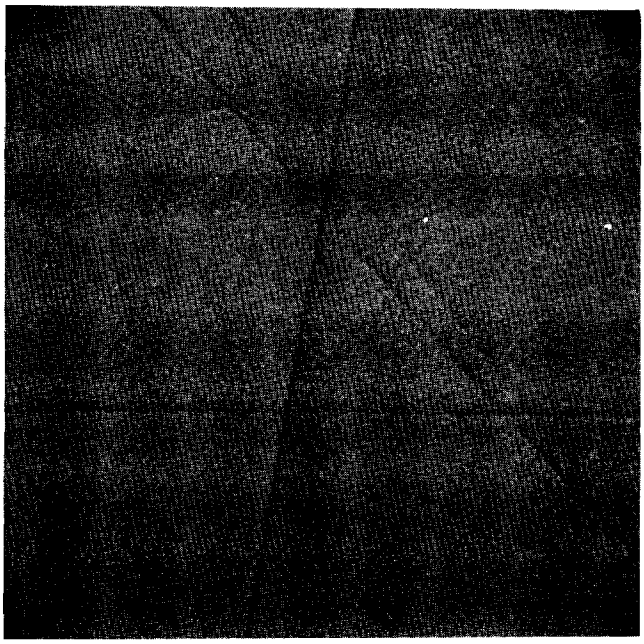

(A)

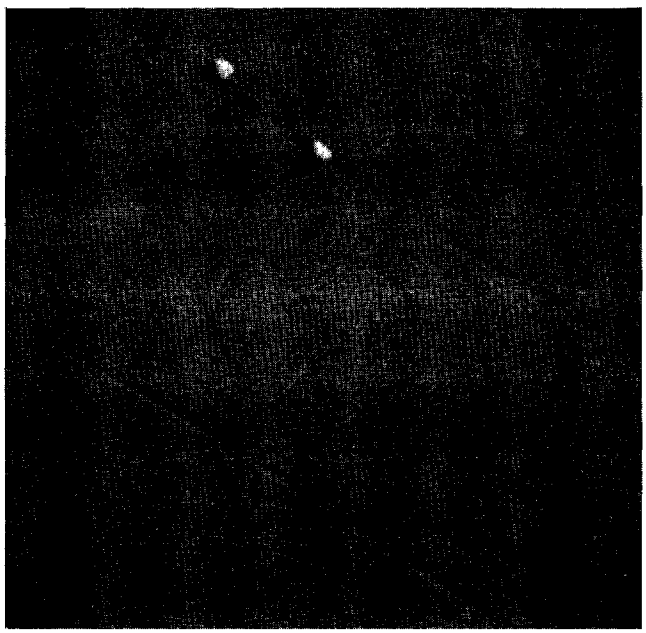

(B)

Figure 51. Sample of $Cd_{1.5}Zn_{1.5}As_2$ Polished with 0.25 μm Diamond (A) Before Etching and (B) After Etching

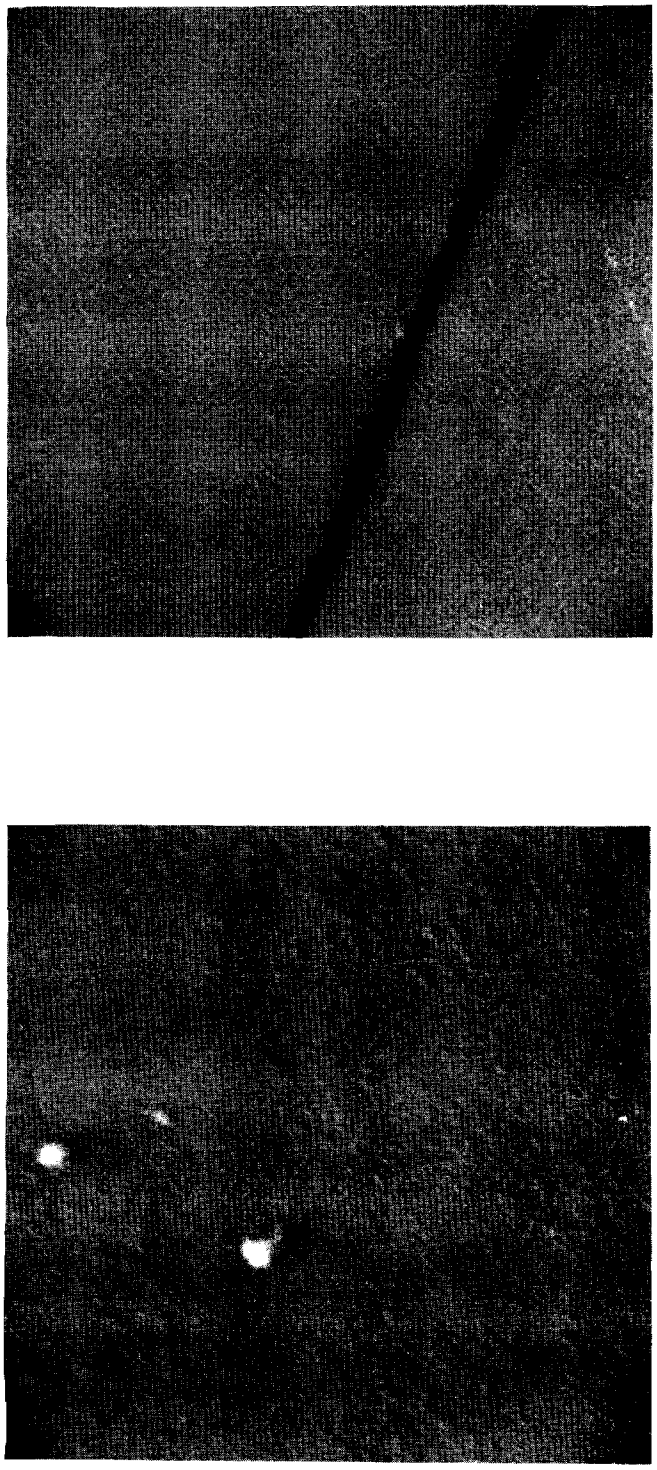

(A)

(B)

Figure 52. Surface of $Cd_{1.5}Zn_{1.5}As_2$ after Polishing 1 1/2 Hours with 0.5 μm Alumina (A) Before Etching and (B) After Etching

BIBLIOGRAPHY

1. L. Zdanowicz and W. Zdanowicz, phys. stat. sol. 6, 227 (1964).

2. W. J. Turner, A. S. Fischler, and W. E. Reece, Phys. Rev. 121, 759 (1961).

3. P. J. Lin-Chung, Phys. Rev. 188, 1272 (1969).

4. R. J. Wagner, E. D. Palik, and E. M. Swiggard, J. Phys. Chem. Solids Supp. 1, 471 (1971).

5. M. Zivitz, Doctoral Thesis, Georgia Institute of Technology (1973).

6. J. R. Stevenson, H. Ellis, and R. Bartlett, Appl. Opt. 12, 2884 (1973).

7. S. A. Korff and G. Breit, Rev. Mod. Phys. 4, 471 (1932).

8. F. C. Brown, The Physics of Solids (W. A. Benjamin Inc., 1967).

9. H. A. Lorentz, The Theory of Electrons (Dover, New York, 1952) 2nd ed.

10. J. D. Jackson, Classical Electrodynamics (J. Wiley and Sons Inc., 1962).

11. E. Merzbacher, Quantum Mechanics (J. Wiley and Sons Inc., 1961).

12. H. Eyring, J. Walter, and G. E. Kimball, Quantum Chemistry (J. Wiley and Sons Inc., 1944).

13. F. Seitz, The Modern Theory of Solids (McGraw-Hill, New York, 1940).

14. D. L. Greenaway and G. Harbeke, Optical Properties and Band Structure of Semiconductors (Pergamon Press, New York, 1968).

15. J. S. Toll, Phys. Rev. 104, 1760 (1956).

16. F. Stern, Solid State Physics 15, 299-408 (1963).

17. R. V. Churchill, Complex Variables and Applications (McGraw-Hill, New York, 1960).

18. D. M. Roessler, Brit. J. Appl. Phys. 16, 1119 (1965).

BIBLIOGRAPHY (Continued)

19. D. M. Roessler, Brit. J. Appl. Phys. 17, 1313 (1966).

20. H. R. Philipp and H. Ehrenreich, Phys. Rev. 129, 1550 (1963).

21. M. Alterelli, D. L. Dexter, H. M. Nussenzveig, and D. Y. Smith, Phys. Rev. B 6, 4502 (1972).

22. J. A. R. Samson, Techniques of Vacuum Ultraviolet Spectroscopy (J. Wiley and Sons, New York, 1967).

23. A. A. Sokolov and I. M. Temov, Synchrotron Radiation (Pergamon Press, New York, 1968).

24. F. C. Brown, P. L. Hartman, P. G. Kruger, B. Lax, R. A. Smith, and G. H. Vineyard, "Synchrotron Radiation as a Source for the Spectroscopy of Solids," N.R.C. Solid State Panel Subcommittee Report, March 1965.

25. E. M. Rowe, R. A. Otte, C. H. Pruett, and J. D. Stebben, IEEE Trans. Nucl. Sci. NS-16, 159 (1969).

26. C. H. Pruett, N. C. Lien, and J. D. Stebben, Third Int. Conf. on Vacuum Ultraviolet Radiation Physics, Tokyo, Japan, 30 Aug. - 2 Sept., 1971.

27. E. J. Scheibner and L. N. Tharp, Surface Science 8, 247 (1967).

28. Programming Languages, Digital Equipment Corp., Maynard, Mass. (1970).

29. FOCAL is a registered trademark of Digital Equipment Corp.

30. D. E. Wrege, DECUS Proc. Spring 1970, p. 77, Digital Equipment Corp., Maynard, Mass. (1970).

31. D. E. Wrege and D. S. Harmer, DECUS Proc. Spring 1972, p. 213, Digital Equipment Corp., Maynard, Mass. (1972).

32. P. Nozieres and D. Pines, Phys. Rev. 113, 1254 (1959).

33. S. L. Adler, Phys. Rev. 126, 413 (1962).

34. J. Hubbard, Proc. Phys. Soc. (London) A68, 441 (1955).

35. P. Nozieres and D. Pines, Phys. Rev. 109, 762 (1958).

36. H. Harrison, J. Chem. Phys. 901 (1970).

BIBLIOGRAPHY (Concluded)

37. J. C. Slater, Phys. Rev. 98, 1039 (1955).

38. H. R. Philipp and E. A. Taft, Phys. Rev. 113, 1002 (1959).

39. M. P. Rimmer and D. L. Dexter, J. Appl. Phys. 31, 775 (1960).

40. P. O. Nilsson and L. Munkby, Phys. kondens Materie 10, 290 (1969).

41. J. L. Shay, private communication.

42. C. Gahwiller, F. C. Brown, and H. Fujita, Rev. Sci. Instrum. 41, 1275 (1970).

43. R. P. Madden, E. L. Ederer, and K. Codling, Appl. Opt. 6, 31 (1967).

44. R. Haensel and C. Kunz, Z. Agnew Physik 23, 276 (1967).

45. R. P. Godwin, Springer Tracts Mod. Phys. 51, 1 (1969).

46. D. H. Tomboulian and P. L. Hartman, Phys. Rev. 102, 1423 (1956).

47. J. Schwinger, Phys. Rev. 75, 1912 (1949).

48. P. W. Palmberg, Appl. Phys. Letters 13, 183 (1968).

49. R. E. Weber and W. T. Peria, J. Appl. Phys. 38, 4355 (1967).

50. N. J. Taylor, Rev. Sci. Instrum. 40, 792 (1969).

51. R. P. Woodward, Doctoral Thesis, Georgia Institute of Technology (1973).

52. R. P. Woodward, private communication.

53. B. R. Livesay, Doctoral Thesis, Georgia Institute of Technology (1972).

54. L. E. Samuels, Metallographic Polishing by Mechanical Methods (Sir Isaac Pitman and Sons Ltd., London, 1971).

55. E. Rabinowicz, Scientific American 218, No. 6, 91 (1968).

VITA

Harry Waters Ellis was born July 6, 1944 in Dalton, Georgia. He is the son of Harold Devine and Mae Waters Ellis. He began his formal education at Pleasant Grove School and completed his secondary training at North Whitfield High School. He received the degree Bachelor of Science in Physics with honors from the Georgia Institute of Technology in 1966. A Master of Science degree in physics was awarded in 1968.

He was the recipient of a National Science Foundation traineeship in 1966 and held a graduate research assistantship from 1968 to 1974. He was a member of the Graduate Student Senate from 1970 to 1972. He is a member of Phi Kappa Phi and Sigma Pi Sigma honorary societies.